MOLECULAR AND PROCESS DETERMINANTS OF SELF-ASSEMBLIES FROM AMPHIPHILIC MACROMOLECULAR BRUSHES

by
Hanying Luo

A dissertation submitted to Johns Hopkins University in conformity with the requirements for the degree of Doctor of Philosophy

Baltimore, Maryland
August, 2016

ABSTRACT

The self-assembly of amphiphilic block copolymers is widely studied as an approach to engineer nano-objects. In aqueous medium, the hydrophobic blocks collapse to form the micelle core while the hydrophilic parts serve as the stabilizing corona. Polymeric micelles are emerging as promising carriers for the delivery of hydrophobic drugs, wherein the poorly water-soluble agents could be solubilized in the micelle core, allowing for their transport at concentrations considerably higher than their intrinsic solubility in water. A variety of different morphologies, including spherical micelles, cylindrical or worm-like micelles, toroids and vesicles result from the self-assembly of linear amphiphilic block copolymers by manipulating the ratio of dissimilar blocks, solvent quality, coronal interactions, and processing parameters.

Macromolecular brushes are graft polymers with densely grafted side chains. Crowded grafting results in a uniquely extended backbone conformation and influences their physicochemical properties. In this dissertation, the self-assembly behavior of amphiphilic macromolecular brushes with poly(glycidyl methacrylate) (PGMA) as backbone bearing poly(ethylene glycol) and poly(D,L-lactide) side chains, was studied. We systematically investigated how variation in the molecular characteristics of amphiphilic brushes, and processing parameters, influenced their aggregate structure.

Amphiphilic macromolecular brushes were further used as hydrophobic solute stabilizers, successfully generating solute nanoparticles by a rapid change in solvent

quality. Nanoparticle morphology was found to strongly depend on the physicochemical characteristics of the solute, on occasions resulting in unusual shapes. Anisotropic morphologies observed are attributed to the mobility of hydrophobic core, and it may potentially assist the shape control of nonspherical aggregate morphologies.

Through a judicious choice of side-chain and backbone length, unimolecular nanoparticles can be readily achieved from amphiphilic macromolecular brushes. These are promising for drug delivery purposes, particularly upon dilution in the blood stream. Harnessing their potential as drug carriers warrants a detailed study regarding their ability to stabilize hydrophobic solutes. We found that a particular type of copolymer adopts a unimolecular structure in the presence of hydrophobic solutes, driven by hydrophobic interactions between the solute and the brush amphiphile. The stability of loaded particles was examined by interactions with human serum albumin. Finally, the release profile of loaded nanoparticles was investigated.

First Reader (Thesis Advisor): Professor Margarita Herrera-Alonso

Second Reader: Professor Kalina Hristova

ACKNOWLEDGEMENT

Five years of doctoral study is one of the most invaluable experience in my life. I appreciate for all challenges that I had faced, which pushes my intellectual limits while sparkles my creativity. I am fortunate to always have great people around during this journey. Without them, I would never have been able to finish this thesis. I would like to take this opportunity to thank those who have been helping me and supporting me.

First and foremost, I would like to express my deepest and sincere gratitude to my advisor, Professor Margarita Herrera-Alonso, for her constant encouragement, patience and support throughout my doctoral study. Dr. Herrera brought me into the amazing world of polymer science and mentored me acquiring knowledges and solving problems. The enthusiasm and hardworking of hers will radiate through my entire career. I would also like to thank my committee members: Professor Hristova, Professor Katz, Professor Cui, Professor Bevan, for their careful review of this thesis.

I also own a debt of gratitude to all my present and past colleagues in Herrera group. Especially I would like to thank Dr. Jose Luis Santos, and Dr. Yanet Elised Aguirre-Chagala, who offered a great help in training me organic synthesis techniques when I first joined Herrera Lab. I am truly grateful to Elena Garcia, Lazaro Pacheco, Dr. Teresa Palacios and Yuxuan Huang, who always inspired me in both research and life during my doctoral study. Without them, it would have been a lonely lab.

I would also like to thank Rodbell award and Paul V. Reoff fellowship from the generous donations of Mrs. Adelle Rodbell and Mr. Paul V. Renoff, respectively, which supported my doctoral study.

My gratitude is also expressed to all the staff members in the Materials Science and Engineering Department. Specifically, I thank Jeanine Majewski, Marge Weaver, and Ada Simari, who have provided a lot of assistance during my study at Johns Hopkins.

Finally, I would express my special thanks to my family and friends for their support throughout my entire life. In particular, I would like to thank my husband Dr. Le Xin, whom I have met since I was thirteen; you are always there supporting me and cheering me up. And I would like to thank my wonderful parents, who support me with their endless and unconditional love. To them, I dedicate this thesis.

TABLE OF CONTENTS

LIST OF FIGURES

LIST OF TABLES

Chapter I: Introduction

1.1 Overview of Drug Delivery Strategies

According to the US pharmacopeia,[1] over 40% of currently marketed drugs are poorly water soluble, and approximately 70% of new drug candidates suffer from limited water-solubility.[2] In the context of parenteral delivery,[3] direct administration of poorly water-soluble drugs could lead to aggregation and precipitation, or cause unwanted adsorption during oral administration,[4] thereby limiting drug concentration at the targeted site and hindering its therapeutic effect.[5] To resolve this issue, a number of drug formulation strategies have been developed to improve bioavailability of poorly water soluble compounds, such as microemulsions, hydrogels, micelles, liposomes, nanocrystals or lipid nanoparticles.[3] There are both advantages and limitations in each of the strategies mentioned above. However, some general guidelines for the design of drug delivery systems is that they undergo controlled degradation, are endowed with external stimuli responsivity, and exhibit long in vivo circulation time.[6] Polymeric micelles are emerging as one of the most promising strategies for the delivery of hydrophobic drugs or diagnostic imaging agents.[6] Harnessing the versatility of polymer chemistry and processing methods, polymeric nanoparticles have demonstrated their potential in generating nanostructures with adaptable morphology and size,[7,8] allowing functional moiety decoration for environmental-responsivity or site targeting.[9,10]

Polymeric nanoparticles are most commonly generated from block copolymer

solution assembly, providing an excellent reservoir to solubilize hydrophobic compounds inside the micelle core, thus allowing their transport at concentrations that exceed their intrinsic water solubility.[6,11-13] Hydrophilic components, such as polyethylene glycol (PEG) are tethered onto the particle surface, creating a passive stabilization barrier that prevents protein adsorption and cellular adhesion.[11,14-16] As a result, micelles could potentially improve the pharmacokinetics profile and/or reduce the toxicity of drugs.[13,17,18] The nano scaled size (~20-100 nm) of objects realized through block copolymer assembly are ideal for in vivo applications,[13,18] since particles within this size range are capable of avoiding renal and lymphatic clearance and opsonization. Hence, particle surface properties and size are key to prolonging their circulation time in the blood, further enabling tumor targeting through the enhanced permeation and retention (EPR) effect during in vivo circulation.[19] Despite the above-mentioned advantages found for polymeric micellar systems, it remains challenging to optimize current copolymer properties and nanoparticle fabrication processes to meet drug delivery application needs. For instance, the complexity of the interaction between particles and the plasma proteins present in biological medium may alter their size or surface charge.[20] Furthermore, there exist inherent difficulties in controlling particles size distribution, as well as precisely reproducing materials from different batches.[13]

1.2 Molecular and Process Determinants of Solution-based Polymeric Self-assemblies

In a selective solvent, amphiphilic copolymers undergo self-assembly in order to minimize the interfacial free energy of the system.[12,18] Similar to their low molecular

weight analogs, block copolymers can self-assemble into different structures, governed by their molecular characteristics, solvent composition, or temperature.[21]

The geometry of these self-assembled structures is controlled by the enforced curvature in the assembly, determined by the relative size and thermodynamic interactions of soluble and insoluble blocks.[22,23] A variety of morphologies, including spheres, cylinders and membrane-enclosed vesicles can be obtained through block copolymer self-assembly, by controlling their molecular characteristics,[7,8,23] as evidenced by the morphology diagram provided in Figure 1.1.

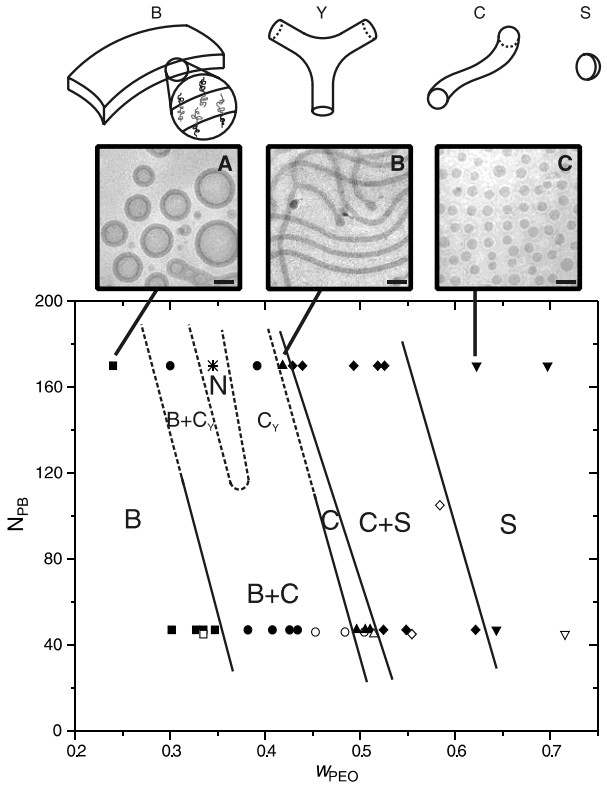

Figure 1.1. Morphology diagram for PB-PEO in water (1 wt%) as a function of molecular size and composition, prepared by Jain *et al.*.[8] N_{PB} and w_{PEO} are the degree of polymerization and weight fraction of the PB and PEO blocks, respectively. Reprinted with permission from ref 8. Copyright 2003 The American Association for the Advancement of Science.

Unlike their low molecular weight analogs, the high molecular weight of block copolymers results in a high energy penalty for polymer chains to transfer between solution and aggregates,[24,25] leading to the slow chain exchange dynamics in the assembly process[8,24,26,27]. Unlike ergodic systems wherein equilibrium is maintained between molecules in the assembly and molecules in the solution, the non-ergodic character in the block copolymer self-assembly suggests the same type of polymer could potentially adopt numerous different structures that are kinetically locked.[23,25] This property not only allows for access to numerous kinetically trapped structures, but also provides more controls over assembly morphologies through processing conditions. For example, a rapid exchange in solvent quality, provided by a multi-inlet vortex mixer (Figure 1.2),[28] or a confined impinging jet mixer,[29] or a microfluidic platform,[30] could achieve mixing time scales smaller than the time scale for block copolymer aggregation, resulting in non-equilibrium assembled nanoparticles.[29] Also, previous work has demonstrated the assembly pathway of charged, amphiphilic block copolymer could be controlled through a combination of solvent mixing and the complexation with divalent organic counter ions, leading to kinetically trapped assemblies.[31] In one last example, the external shear force exerted by an on-chip assembly process could offer sufficient energy to overcome repulsive interparticle potentials, resulting in assembled structures that are distinct from the off-chip equilibrium structure.[32]

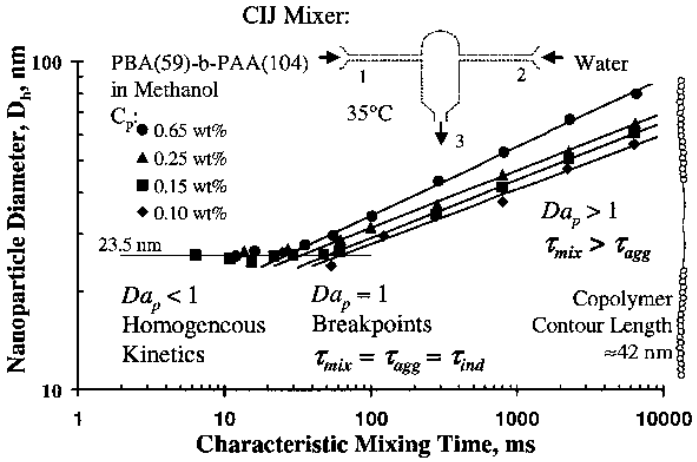

Figure 1.2. Rapid self-assembly of diblock copolymer nanoparticles in a confined impinging jet mixer induced by addition of a nonsolvent to a stream of soluble copolymer. The resulting particle hydrodynamic diameter, measured by dynamic light scattering (y-axis), is shown to be a strong function of the characteristic time of mixing (x-axis) until homogeneous kinetics are obtained, $Da_p < 1$. The mixing time and aggregation time are equivalent at the break point, $Da_p = 1$. Da_p is the Damkohler number, defined as the characteristic mixing time (τ_{mix}) divided by the characteristic aggregation time of diblock copolymer (τ_{agg}). Reprinted with permission from ref 29. Copyright 2003 American Physical Society.

Two major methods have been commonly adopted to prepare nanoparticles from amphiphilic copolymers, according to their water solubility: (1) the direct dissolution method, and (2) the dialysis method. The former one is suitable for copolymers that are marginally soluble in water, and micelles are prepared by simply dissolving the amphiphilic copolymers in the aqueous medium. It requires a polymer concentration well above its C_{CMC} value, and oftentimes a heated aqueous medium. The latter method is applied to copolymers that are not soluble in water. In this case, the polymers are dissolved in a water-miscible organic solvent (e.g., dimethylformamide, tetrahydrofuran, or acetonitrile) and placed inside a dialysis cartridge with a molecular weight cutoff that is below that of the copolymer. The cartridge is introduced in an aqueous environment where solvent exchange –and thus,

micellization– takes place.[6,33,34]

The hydrophobic core of micelles serves as a reservoir for hydrophobic solutes, such as drug molecules or imaging agents. Similarly with micelle preparation methods, drug loaded nanoparticles could be prepared by direct dissolution method, wherein drug molecules were dissolved together with marginally water-soluble copolymers in an aqueous solvent. Or, drug loading could be attained by dialysis method, with solutes and polymer dissolved together in an organic solvent common to both prior to undergoing solvent exchange.[34] The solvent-casting method is yet another widely used alternative. In this case, a copolymer-drug solution is prepared in a volatile organic solvent and the solvent is allowed to evaporate to form a polymeric film. Film rehydration with a heated aqueous solvent and/or by intensive shaking, yields the final drug loaded micelles.[34,35] In general, the drug solubilization process is highly dependent on the interactions between a solute and the core-forming hydrophobic block of the amphiphile. The compatibility between solute and hydrophobic blocks dictates the efficiency of drug incorporation. The compatibility between polymer and solutes can be evaluated based on their Flory-Huggins interaction parameter (χ_{sp}); a lower value indicates better compatibility. The interaction parameter is expressed as $\chi_{sp} = (\delta_s - \delta_p)^2 V_s/\mathrm{RT}$, wherein δ_s and δ_p are the Scatchard-Hidebrand solubility parametrs of the solute and core-forming polymer block respectively, and V_s is the molar volume of the solubilized drug.[6]

The aforementioned methods for nanoparticle fabrication are based on slow thermodynamically controlled processes, which may lead to drug/matrix phase

separation and low drug loading.[36] Alternatively, kinetically controlled rapid precipitation techniques have been developed to enhance drug loading efficiency. In the formation of nanoparticles, solute nucleation kinetics are controlled by both local supersaturation and temperature.[37] Supersaturation is defined as

$$S \equiv \frac{c}{c_\infty}$$

where c is the ratio of the total mass of solute fed divided by the final solution volume, and c_∞ is the bulk solubility in the final solvent mixture.[38] In a rapid precipitation process, the solvent contains the solute and the stabilizing amphiphile, and these undergo rapid mixing with a selective solvent for the polymer and the solute, and the resulting high supersaturation induces a rapid solute nucleation and growth. The final particle size is controlled by the adsorption rate of the stabilizing copolymers, which acts to quench particle growth.[28,39] This process is illustrated in Figure 1.3A. For this to occur in a homogeneous environment, it requires a rapid mixing time $\tau_{mix,}$ which should be shorter than the time necessary for nanoparticle formation τ_{flash}, wherein the τ_{flash} involves both the formation time of block copolymer nanoparticles τ_{agg}, and the induction time τ_{ng} of solutes nucleation and growth. The match between τ_{agg} and τ_{ng} further dictates nanoparticle size and morphology.[40] This so-called Flash Nanoprecipitation technique has been developed by Prud'homme and co-workers,[40] utilizing a multi-inlet vortex mixer (MIVX) or a confined impinging jet (CIJ) mixer, as illustrated in Figure 1.3B.

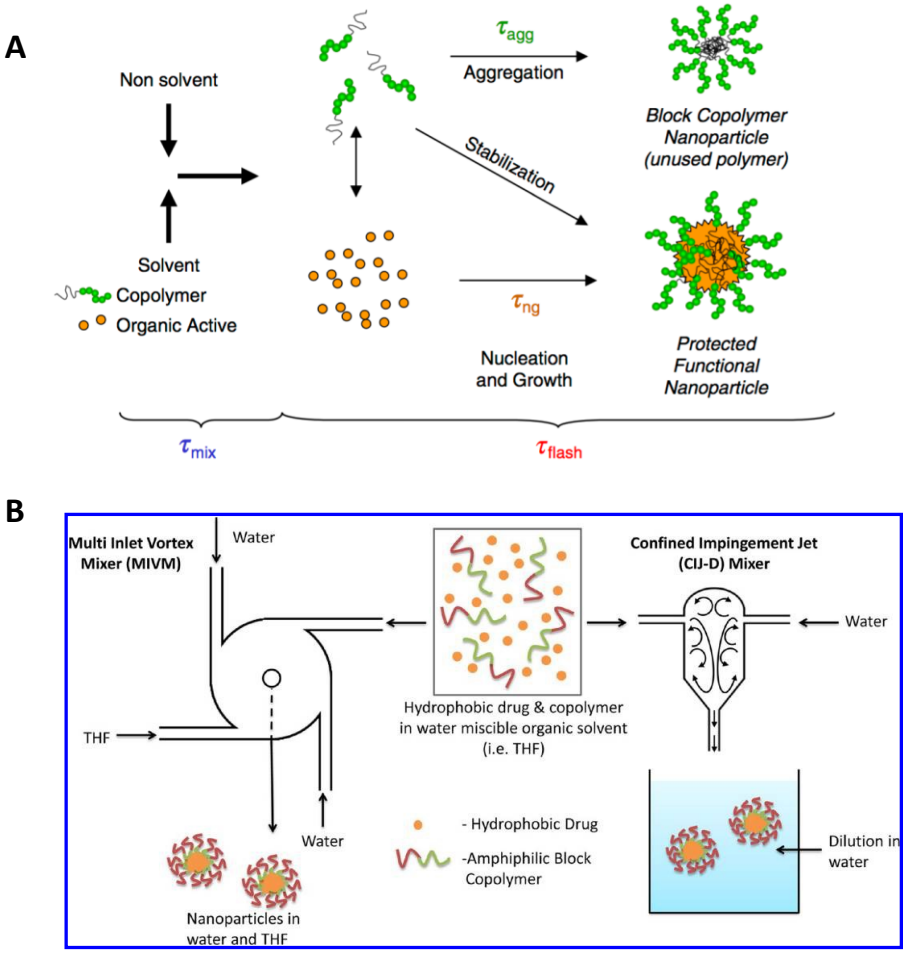

Figure 1.3. (A) Flash Nanoprecipitation process. (B) Schematic illustrations of the multi-inlet vortex mixer (MIVM) and the confined impingement jet (CIJ) mixer. In the MIVM, the drug and copolymer in organic solvent (i.e. THF) undergo rapid mixing with greater volume of water, resulting in kinetically frozen nanoparticles in a cosolvent mixture from mixer outlet. In the CIJ mixer, flows rate of water and organic phase have to be balanced, and final particles were immediately injected to large volume of water to achieve organic solvent dilution.[41] (A) Reproduced from Johnson and Prud'homme (2003),[40] with permission from CSIRO Publishing. (B) Reprinted with permission from ref 41. Copyright 2013 American Chemical Society.

Flash nanoprecipitation allows control over nanoparticle size via the initial supersaturation and polymer adsorption kinetics, producing nanoparticles with uniform size distribution.[42] This method has been demonstrated to be a highly efficient and reproducible approach to prepare spherical nanoparticles capable of carrying different types of hydrophobic cargos. However, capabilities of this

technique to prepare non-spherical aggregates still remain unexplored.[25] Also, there is a lack of work examining the influence of polymer architecture on nanoparticle formation.

1.3 Block Copolymer Architecture

In nature, biomolecules exhibit elaborate molecular structures. For example, proteoglycans are brush-like macromolecules found in human body, they support different types of bodily functions, including offering lubrication in cartilage, or assisting mucociliary clearance. The multi-functionality is related with their brush-like structure, which enables dense packing of functional groups along the backbone.[43] Another example is glycogen, wherein the highly branched architecture offers unique performance in energy storage in animals.[44] Inspired by biomolecules, there has been great interest to mimic their properties, and in this respect a variety of macromolecules have been developed, including dendrimers,[45] linear-dendritic copolymers,[46] multi-arm star copolymers,[10,47], toothbrush-like copolymers,[48] graft copolymers,[49] and molecular brush copolymers.[50-53]

Recent advances in polymerization techniques have facilitated the synthesis of well-defined macromolecules with complex architecture, and a number of controlled polymerization methods have been utilized to prepare copolymers with narrow molecular weight distributions. These include the controlled radical polymerization routes[17,54], ring-opening metathesis polymerization (ROMP),[55,56] and ring-opening polymerization.[10,48,57] Dendritic macromolecules, for example, are synthetic

analogues of the globular three-dimensional structure of certain biomolecules, and their syntheses most commonly involves the stepwise growth of each generation from a central core.[58,59] However, they are limited by onerous syntheses steps, and the low yield leads to high cost of production. Thereby, other globular hyperbranched structures –such as multi-arm star copolymers– with facile syntheses were developed.[58] Multi-arm star copolymers are globular molecules composed of at least three branches (arms) radiating out from the central core. They are normally prepared using a multifunctional central scaffold, followed by polymerization of arms through initiation sites via ROP or controlled radical polymerizations.[9,10,47,58] The development of star copolymers simplified the synthesis of branched structures, however, the total number of branches (arms) are limited.[58]

Alternatively, there is a growing interest in studying anisotropic branched structures, such as graft and molecular brush copolymers. Graft copolymers are composed of a polymeric backbone with side chains covalently attached at regular intervals.[60,61] Molecular brush copolymers are a special group of graft copolymers,[62-65] wherein the length of branches are longer than the space between neighboring grafting points.[60] The excluded volume interactions among crowded side chains in molecular brushes force the backbone to adopt an extended conformation,[43,62,63] differentiating them from traditional graft polymers. Generally, there are three main routes for constructing graft and molecular brushes copolymers: "grafting through", "grafting onto", and "grafting from"[43,62-64], as illustrated in Figure 1.4. Briefly, "grafting through" involves polymerization of macromonomers with a terminal functionality, and it ensures high grafting density. Ring-opening metathesis polymerization

(ROMP) has been employed in this approach due to its remarkable efficiency.[55,66,67] "Grafting to" involves the coupling of prepared side chains to the backbone, and azide-alkyne Huisgen cycloaddition ("click" reaction) is often adopted to achieve high grafting efficiency.[68,69] In the "grafting from" approach, side chains are polymerized from the backbone through initiation sites, and controlled polymerization chemistries are preferred in this approach.[70] There are limitations in each of the strategies listed above; therefore, a combination of different approaches is often adopted to enable and optimize the synthesis of molecular brushes.[43]

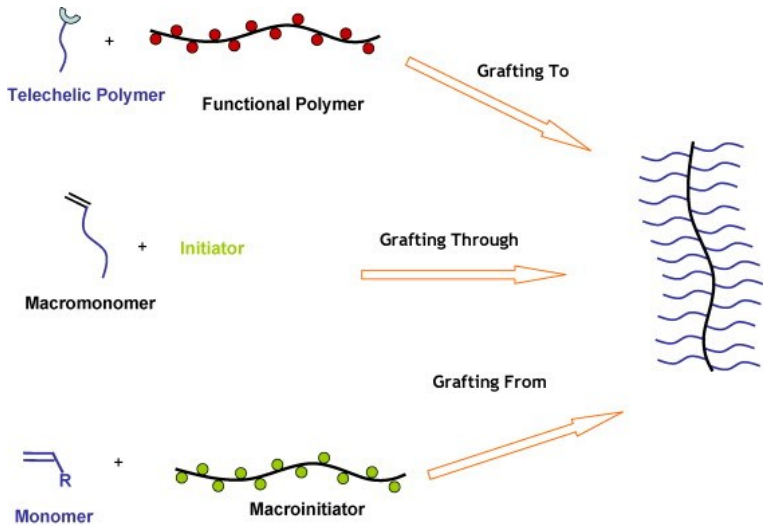

Figure 1.4. Three main approaches to prepare molecular brushes: grafting through, grafting to, and grafting from. Reprint with permission from ref 63. Copyright 2010 Elsevier.

It is well known that the topology of copolymers also plays an important role in determining their bulk and solution properties.[71] In particular, branched polymers normally exhibit different physical properties compared with their linear analogs, such as melt rheology and mechanical behavior.[48,72]. More importantly, polymer architecture also serves as a crucial factor that determines physicochemical properties

of micelles derived from them.[73] In branched structures, the abundant covalent bonds provide extra intrinsic stability to the assembled structures.[13,74] Moreover, the excluded interactions among dense branches result a lower level of intermolecular entanglement in assembled structures,[57,75] giving rise to smaller aggregation numbers in self-assembled structures.[76] In some cases, with enough steric hindrance from corona-forming blocks, unimolecular micelles are formed.[76] The unimolecular structure ensures that the micelle formation and dissociation is independent of polymer concentration; thereby further improving micellar stability against dilution.[13,47,62] By virtue of their enhanced stability, numerous studies have been carried out investigating the potential of branched polymer micelles as drug carriers. These studies reveal their advantageous physicochemical properties, such as prolonged circulation time,[9,10] higher drug loading capacity,[48,77] and better drug release kinetics.[48,51] In addition, the large numbers of end groups of branched structures are available for functional decoration, allowing them to achieve multifunctional tasks simultaneously.[13,51,55,78]

Nevertheless, a complete understanding of the self-assembly behavior of branched copolymers is still lacking. The complexity of the branched structure results in additional intramolecular aggregation in the self-assembly process.[60,79-81] For instance, upon decreasing solvent conditions, a number of different intramolecular aggregates including spheres, cylinders, and multi-domain pearl-necklace can form, as established by theoretical predictions, molecular dynamics simulations, and observed experimentally.[50,60,80] These intramolecular domains complicate the solution assembly behaviors of branched copolymers, which is not yet fully explored but is especially

important since the in vivo properties of drug carriers are largely depending on their physicochemical properties, such as size, surface charge and morphology.[58] A better fundamental understanding of branched copolymers self-assembly behaviors, will assist in the rational design of polymer structures, and in optimizing their properties as drug delivery carriers.

1.4 Objectives

Polymeric micelles formed by the solution-based self-assembly from amphiphilic copolymers provide an efficient platform for the delivery of hydrophobic drugs or diagnostic imaging agents, largely improving their biodistribution. Among these, micelles from copolymers with branched structures are poised to offer enhanced in vitro and in vivo properties. Hence, there exist challenges and opportunities in investigating the self-assembly behavior of complex copolymer structures. Moreover, no prior work is known regarding the kinetics of aggregation of branched polymer systems, which as previously mentioned, can become increasingly complex because of intra/intermolecular association phenomena.

In this work, we provide insights regarding the molecular and process determinants of self-assemblies from amphiphilic molecular brushes, and investigate their physicochemical properties as drug stabilizers. The work is divided into five chapters. In Chapter II, a systematic study of the variation in molecular properties of amphiphilic asymmetric molecular brushes and its effect on aggregate structure was conducted. The effect of processing parameters on solution assemblies of these macromolecules was also examined. In Chapter III, the influence of copolymer

topology on solution assemblies was investigated, and the assembly kinetics of branched copolymers possessing different architectures was compared. In Chapter IV, amphiphilic molecular brushes were used as hydrophobic solute stabilizers, successfully generating solute nanoparticles by a rapid change in solvent quality. Nanoparticle morphology was found to strongly depend on the physicochemical characteristics of the solute, on occasions resulting in unusual anisotropic shapes. In Chapter V, we discuss a particular type of molecular brush copolymer which leads to solute stabilization in the form of a unimolecular construct, and examine the properties of the particles generated from it with respect to the type of solute. In Chapter VI, we contrast the physicochemical properties of unimolecular micelles with multimolecular micelles from linear diblock copolymers in the context of drug delivery, with particular emphasis on their stability on interaction with human serum albumin and drug release kinetics.

Chapter II: Synthesis and Self-assembly of Amphiphilic Molecular Brushes

2.1 Introduction

The self-assembly of amphiphilic block copolymers has been widely studied as an approach to engineer nano-objects. A variety of different features, including spherical micelles,[7,8,23,82-86] cylindrical or worm-like micelles,[7,8,23,87] toroids,[86,88-90] and vesicles,[7,23,82,84,87] result from the self-assembly of linear amphiphilic block copolymers by manipulating the ratio of dissimilar blocks, solvent quality, and coronal interactions.[7,22,23,84,91] Aside from the possibilities enabled by chemical diversity, aggregate structure can also be manipulated through kinetic features of the assembly process.[25,31,32,86,92] Elucidating the molecular (bottom-up) and process (top-down) parameters influencing self-assembly should enable the fabrication of increasingly complex morphologies with unique functions, thus broadening their envisioned applicability.

Unlike linear amphiphiles, the morphological determinants of solution assemblies from more complex macromolecular building blocks, such as graft copolymers, are far less explored. In terms of morphological diversity and control over the characteristic sizes of self-assembled objects, there exists a lack of work showing the equivalence between graft copolymers and their linear analogs.[87]

In this chapter, we report on our findings regarding the self-assembled structures from

amphiphilic asymmetric macromolecular brushes, triggered by a large and rapid change in solvent quality. As previously defined, molecular brushes are graft polymers wherein the distance between grafting points is smaller than the characteristic dimensions of the side-chains. Crowded grafting results in a uniquely extended backbone conformation and influences their physicochemical properties.[93-95] Amphiphilic asymmetric macromolecular brushes consist of hydrophobic and hydrophilic side-chains grafted onto the same backbone repeat unit.[52,95,96] We demonstrate that a decrease in the hydrophilic ratio results in morphological transitions of self-assemblies from spherical micelles to cylindrical micelles, and finally bilayer structures (vesicles). Furthermore, we discuss the process parameters leading to the formation of toroidal aggregates.

2.2 Materials and Method

2.2.1 Materials and Characterization

All reagents were commercially available and used as received unless otherwise noted. Glycidyl methacrylate (GMA, Aldrich 97%) was passed through a short basic alumina column to remove the inhibitor. 2,2′-Azobis(isobutyronitrile) (AIBN) and D,L-lactide were recrystallized from methanol and anhydrous ethyl acetate, respectively. 1,8-Diazabicyclo[5.4.0]undec-7-ene (DBU) was kept over molecular sieves (3 Å) overnight. Deionized water was purified in a Barnstead Nanopure system to a final resistance of 18.2 mΩ; it will be referred to as Nanopure water.

Gel permeation chromatography (GPC) was performed on a Waters 1515 Isocratic

HPLC equipped with two Styragel® columns (HR4, HR3, 300 mm x 7.8 mm) connected in series, a differential refractive index detector (Waters 2414) and a UV-visible detector (Waters 2489). HPLC grade tetrahydrofuran was used as the eluent, at a flow rate of 1 mL/min. Molecular weights are reported referenced to polystyrene standards (Shodex SL-105). ^{1}H NMR spectra were recorded on a Bruker AV 400 MHz spectrometer in either $CDCl_3$ or DMSO-d_6. Spectra were referenced to $CHCl_3$ (7.26 ppm) or DMSO (2.50 ppm). Dynamic Light Scattering experiments were conducted on a Malvern Instruments Nano-ZS ZetaSizer equipped with a 4 mW He-Ne laser operating at 633 nm. All measurements were performed at 25 °C at a scattering angle of 173°. Bright-field transmission electron microscopy (TEM) was performed on a FEI Tecnai 12 TWIN transmission electron microscope operated at an acceleration voltage of 100 kV. TEM images were recorded by a SIS Megaview III wide-angle CCD camera. Carbon-coated copper grids (Electron Microscopy, Hatfield, PA) were ionized under plasma before sample preparation. Grids were placed on a drop of aggregate suspension (20 μL). After 5 min, the grid was washed under five drops of doubly distilled water and placed onto a drop (20 μL) of a 2 wt% aqueous uranyl acetate solution for 30 s. Grids were then blotted with filter paper and samples were allowed to dry at room temperature prior to imaging.

2.2.2 Synthesis of Amphiphilic Molecular Brushes

PGMA backbone.

Synthesis of the PGMA backbone is described in detail elsewhere.[97] Briefly, GMA (3 mL, 0.022 mol), 2-cyano-2-propyl benzodithioate (CPB) (4.3 μL, 0.022 mmol,) and

AIBN (0.7452 mg, 0.0045 mmol) were added to a clean and dry round bottom flask equipped with a magnetic stir bar and a septum. Reagents were dissolved in 3 mL of benzene, and the mixture was bubbled with nitrogen for 1 h. The reaction was conducted at 60 °C for 16 h. Polymerization was stopped by immersing the flask in an ice bath and opening it to atmosphere. Aliquots were taken to evaluate monomer conversion. Samples were diluted with dichloromethane and precipitated in methanol. The resulting precipitate was dried under vacuum. Yield: 46.7%. GPC: M_n=71.06 kDa, M_w/M_n=1.16 (Figure 2.1). ^{1}H NMR peaks assignments is shown in Figure 2.2. Conversion was evaluated based on the ratio of the signal from polymer (e) and from unreacted monomer (e', Figure 2.2 inset), according to $I_e/I_e+I_{e'}$. Conversion was calculated to be 50%, and the degree of polymerization (DP) is ~500. DP was estimated by multiplying conversion and the initial monomer/chain transfer agent molar ratio.

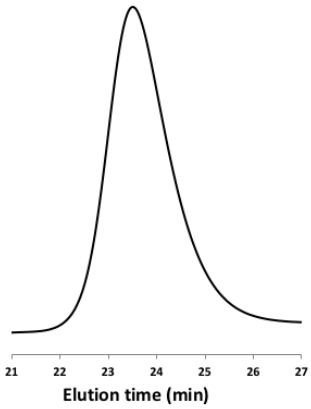

Figure 2.1. Chromatogram of PGMA500 backbone.

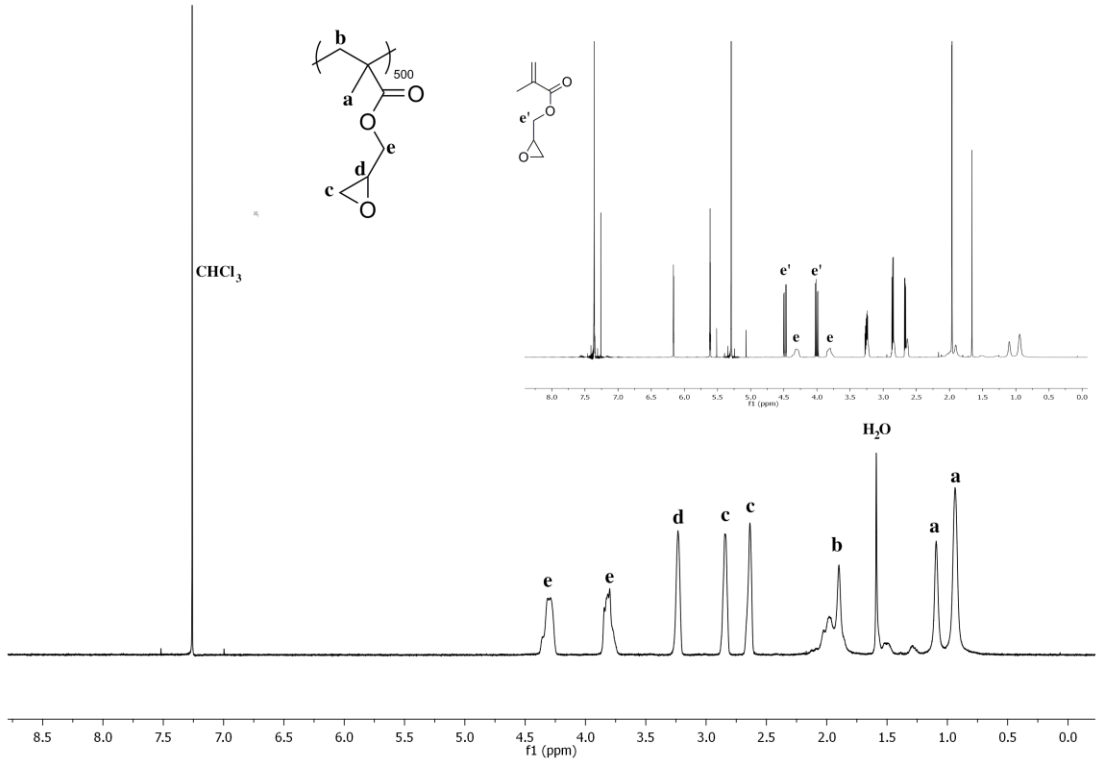

Figure 2.2. ^{1}H NMR spectra of purified PGMA500 and unpurified material containing monomer (inset).

PGMA$_{500}$-g-N$_3$.

PGMA (500 mg, 3.52 mmol epoxy groups) was added to a round bottom flask and dissolved in 20 mL of *N*,*N*-dimethylformamide (DMF). Sodium azide (700 mg, 10.77 mmol) and ammonium chloride (575 mg, 10.75 mmol) were added once the polymer was completely dissolved. Azidolysis was conducted at 50 °C under reflux for 24 h. The resulting solution was cooled to room temperature and diluted with THF. Salts were filtered off and the solution was concentrated before precipitation into Nanopure water. Solids were freeze-dried. Yield: 64.2%. ^{1}H NMR peaks assignments are shown in Figure 2.3, signals indicate complete conversion.

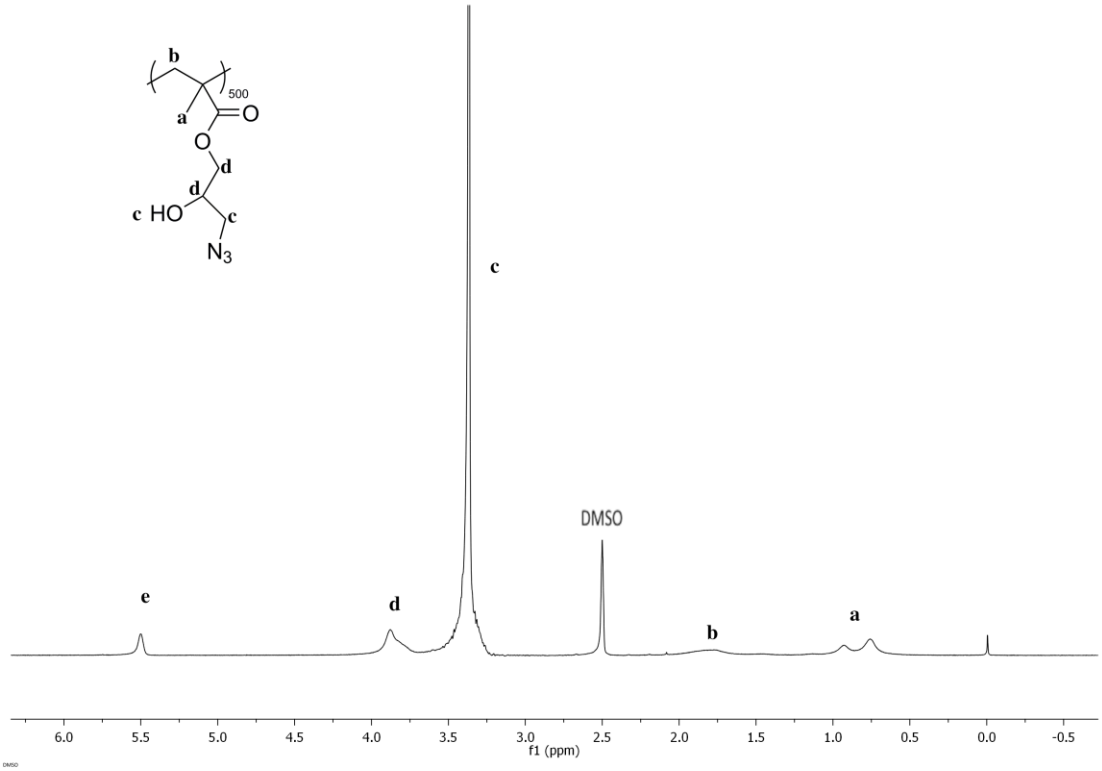

Figure 2.3. ^{1}H NMR spectrum of PGMA$_{500}$-N$_3$.

PGMA$_{500}$-g-PLA$_x$.

The protocol for this synthesis is adapted from Huang *et al*.[97] Known amounts of PGMA$_{500}$-*g*-N$_3$ and D,L-lactide were loaded into a round bottom flask, and placed under high vacuum for ~ 5 h. After backfilling with nitrogen, anhydrous DMF was added to dissolve the reagents. DBU was then injected and the reaction was allowed to proceed for 1.5 h under nitrogen at room temperature. Polymerization was quenched by addition of benzoic acid. DMF was removed under vacuum and the polymer was re-dissolved in THF, followed by precipitation into a mixture of water and methanol (1:1, vol). Solids were lyophilized. ^{1}H NMR of the resulting grafted polymer is shown in Figure 2.4. The DP of PLA side chains was calculated by the ratio of signal from the terminal unit of PLA (*g*) and signal *e* from the PLA chain

(I_g/I_e+1).[97]

Table 2.1. Summary of the syntheses of PGMA500-g-PLAx copolymers with different PLA lengths.

copolymer	$PGMA_{500}$-*g*-N_3 (mg, mmol of OH)	D,L-lactide (g, mmol)	DBU (µL, mmol)	DMF (mL)	Benzoic acid (mg, mmol)	Yield
$PGMA_{500}$-*g*-PLA_{11}	130, 0.7	0.562, 3.9	21.7, 0.145	20	45, 0.368	72.9%
$PGMA_{500}$-*g*-PLA_{26}	50, 0.27	0.571, 3.96	21.9, 0.146	10	45, 0.368	84.1%
$PGMA_{500}$-*g*-PLA_{56}	100, 0.54	2.8, 19.43	108, 0.722	35	220, 1.801	68.0%

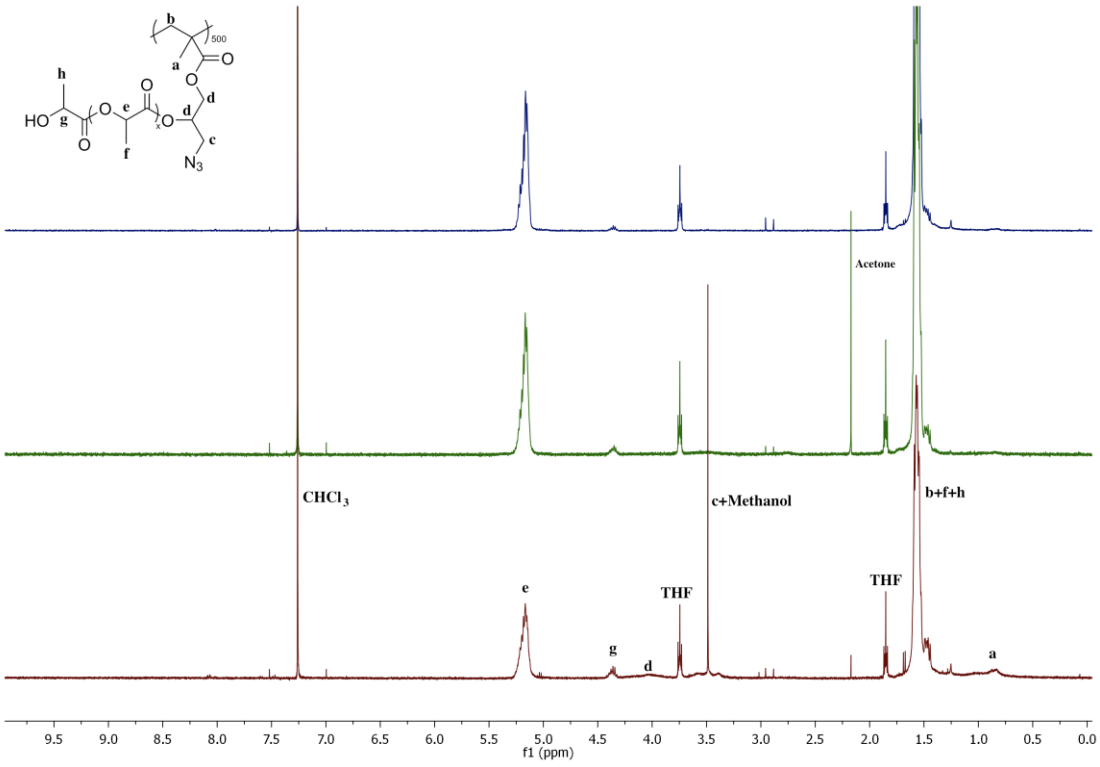

Figure 2.4. ^{1}H NMR spectra of $PGMA_{500}$-*g*-PLA_x. From bottom to top x=11, 26, and 56.

Alkynyl-terminated PEG.

Monomethoxypoly(ethylene glycol) (mPEG, 10.13 g, 13.5 mmol) was transferred to a round bottom flask and placed under high vacuum for ~5 h. After backfilling the flask with nitrogen, 5-hexynoic acid (1789 µL, 16.21 mmol) and 4-

(dimethylamino)pyridine (DMAP) (676.49 mg, 5.54 mmol) were added and purged with nitrogen for 30 min. Then, 30 mL of anhydrous dichloromethane (DCM) were added to dissolve the reagents. N,N'-dicyclohexylcarbodiimide (DCC) (5.57 g, 27 mmol) was dissolved in 5 mL of anhydrous DCM and added to the reaction mixture dropwise via syringe. The raw product was filtered and extracted with 1 M HCl solution 10 times, with DI water 3 times, and with a 1 M NaOH solution 5 times. The solution was then dried over anhydrous magnesium sulfate. After filtration, the solvent was removed under vacuum and the product was dried in the vacuum oven. Yield: 63.9%. ^{1}H NMR (Figure 2.5) indicated quantitative conversion.

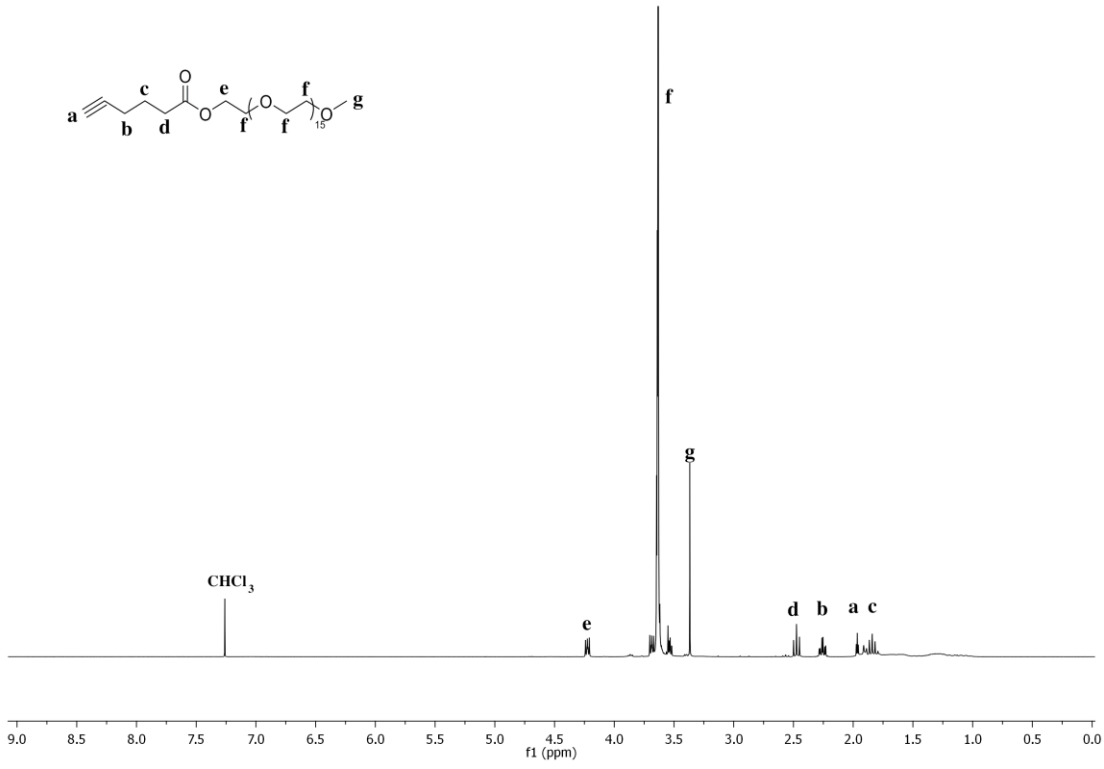

Figure 2.5. ^{1}H NMR spectrum of 5-hexynoic acid functionalized alkynyl-PEG.

$PGMA_{500}$-g-PEGm/PLA_x.

The protocol for this synthesis was adapted from Chen, et al.[98] The 'click' reaction

was catalyzed by $CuSO_4 \bullet 5H_2O$/ascorbic acid. In all cases, a molar ratio of N_3, alkynyl groups, $CuSO_4 \bullet 5H_2O$ and ascorbic acid was kept at 1:1:0.2:1 (details in Table 2.2). $PGMA_{500}$-*g*-PLA_x was mixed with an equimolar amount of alkynyl-PEG in a round bottomed flask. After complete dissolution in DMF, ascorbic acid was added and the solution was bubbled with nitrogen for 30 min. $CuSO_4 \bullet 5H_2O$ was then added under nitrogen and the reaction proceeded for 12 h. The solvent was evaporated, and the raw product was re-dissolved in THF. Polymers were purified by dialysis against Nanopure water for 4 days and lyophilized. ^{1}H NMR spectra are shown in Figure 2.6.

Table 2.2. Summary of the syntheses of $PGMA_{500}$-*g*-PEG_{16}/PLA_x amphiphilic block copolymers.

copolymer	$PGMA_{500}$-*g*-PLA_n (mg, mmol of N_3)	Alkynl-PEG (mg, mmol)	$CuSO_4 \bullet 5H_2O$ (mg, mmol)	Ascorbic acid (mg, mmol)	DMF (mL)	Yield
$PGMA_{500}$-*g*-PEG_{16}/PLA_{11}	200, 0.21	174.2, 0.21	9.78, 0.04	36.1, 0.21	15	86.1%
$PGMA_{500}$-*g*-PEG_{16}/PLA_{26}	202, 0.098	86, 0.10	5.23, 0.02	17.75, 0.10	10	89.2%
$PGMA_{500}$-*g*-PEG_{16}/PLA_{56}	500, 0.12	92.97, 0.11	5.22, 0.02	18.38	15	76.5%

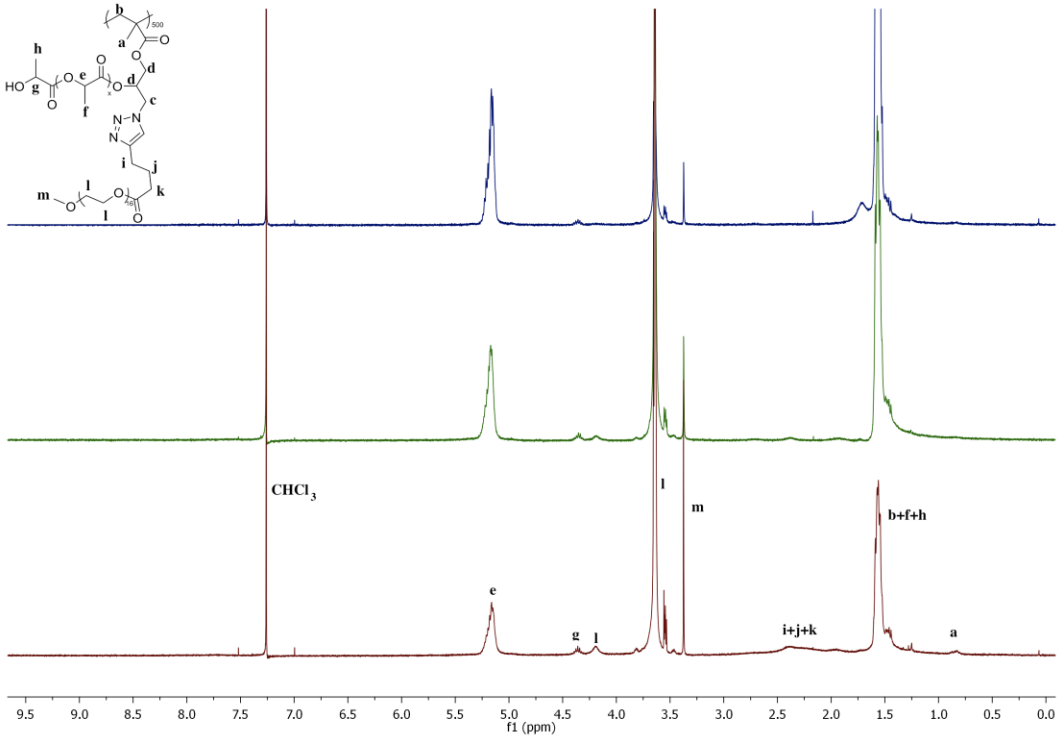

Figure 2.6. ^{1}H NMR spectra of PGMA$_{500}$-*g*-(PEG$_{16}$/PLA$_{x}$). From bottom to top x=11, 26, and 56.

2.2.3. Amphiphilic Molecular Brushes with Different Backbone Repeat Units

A similar approach was adopted to synthesize amphiphilic molecular brushes with different backbone lengths, as discussed above. Characteristics of the resulting PGMA backbones are summarized in Table 2.3, and GPC results are provided in Figure 2.7. Molecular characteristics of the final products are summarized in Table 2.4.

Table 2.3. Characteristics PGMA backbone with different DP.

	M_w[a] *(kg/Mol)*	$Đ_M$ [a]
$PGMA_{68}$	10.58	1.23
$PGMA_{114}$	16.08	1.13
$PGMA_{273}$	31.51	1.27
$PGMA_{721}$	92.60	1.18

[a]Measured by gel permeation chromatography.

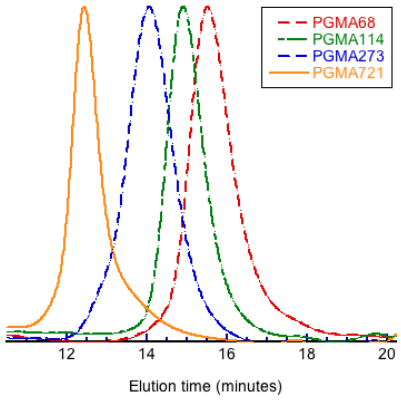

Figure 2.7. Chromatograms of PGMA backbones with different DP.

2.2.4. Differential Refraction Index Measurement

Measurements were performed on an Optilab-rEX refractive index detector (Wyatt Technology) at a wavelength of 658 nm. Flow cell temperature was set at 25 ºC. Sample and solvent solutions were pumped with a syringe pump (New Era Pump System, NE-1000) at 0.2 mL/min through a 0.45 um PVDF syringe filter (Thermo Scientific) prior to measurements. Five concentrations of each sample were prepared in anhydrous dimethylformamide: 0.2, 0.5, 1.0, 1.5, and 2.0 mg/mL. Aggregate solutions were prepared in Nanopure water at the following concentrations: 0.01, 0.02, 0.04, 0.06, 0.12 and 0.21 mg/mL. dn/dc values were analyzed using an Astra 6.1 software.

2.2.5 Static Light Scattering Measurement

Static light scattering (SLS) was performed on a Dawn Heleos II (Wyatt Technology) with a 120 mW GaAs linearly polarized laser operating at 658 nm. Sample and solvent solutions were pumped with a syringe pump (New Era Pump System, NE-1000) at 0.2 mL/min through a 0.45 um PVDF syringe filter (Thermo Scientific) prior to measurements. Polymer and aggregate concentrations were the same as above. Measurements of molecular brushes and micelles were normalized using polystyrene (20 kDa, Fluka; 5 mg/mL solution in dimethylformamide) and dextran (9 kDa-11 kDa, Aldrich; 5 mg/mL solution in Nanopure water), respectively. dn/dc values were applied to determine the absolute molecular weights and M_w was extracted from Zimm plots using Astra 6.1 software and the Debye model.

2.2.6 Self-assembly of Amphiphilic Molecular Brushes.

a) Under a rapid change in solvent quality

Amphiphilic molecular brushes were dissolved in tetrahydrofuran (THF, 2.5 mg/mL unless otherwise specified) and sonicated. A lower concentration (0.5 mg/mL) was also examined for $PGMA_{500}$-*g*-PEG_{16}/PLA_{26}. Rapid self-assembly was carried out in a four-stream vortex mixer. A detailed description and characterization of the mixer are provided elsewhere.[28] Nanopure water was charged into three 50 mL syringes (Hamilton, NJ) and the organic solution into a 10 mL syringe, and mounted on two separate syringe drivers (PHD Ultra, Harvard Apparatus). The THF:water volumetric ratio (solvent jump) used was 1:9 with mixing speeds of 12 mL/min and 108 mL/min

(36 mL/min per stream) for the organic and aqueous phases, respectively. Other solvent jumps used were 1:3 and 1:12. For the 1:3 jump, the velocities of each stream were 30 mL/min (aqueous and organic). For the 1:12 jump, the velocity of the aqueous stream was 6 mL/min, while for the aqueous phases they were 36 mL/min. Samples were collected in clean scintillation vials and dialyzed (6-8 kDa MWCO, Spectrapor) against Nanopure water for 24 h. Water was replenished every 4 h throughout the dialysis process. Suspensions were stored in clean scintillation vials at 4 °C for further use.

b) By dialysis

For the dialysis method, 2.5 mg/mL of polymer solution in THF was transferred to a dialysis membrane (6-8 kDa MWCO, Spectrapor) and dialyzed against water under mild stirring for 24 h. Approximately 5 mL of the polymer solution (in THF) was loaded into a dialysis membrane and placed into a 1 L beaker containing 1 L of Nanopure water (final resistance of 18.2 mΩ). The contents of the beaker were stirred with a magnetic stir bar at ~200 rpm. The dialysis bag did not touch the bottom of the beaker to prevent interference with stirring. Dialysis took place for 24 h at room temperature. During the first 12 h, water was replenished three times (approximately every 3 hours). The suspension was left in the water used for the fourth replenishment overnight. The contents of the dialysis bag were then carefully transferred into clean and dry scintillation vials for storage.

2.3 Result and Discussion

2.3.1 Synthesis of Amphiphilic Molecular Brush

Amphiphilic asymmetric macromolecular brushes were constructed by a combination of "graft from" and "graft onto" strategies, as shown in Scheme 2.1. Poly(ethylene glycol) (PEG) and poly(D,L-lactide) (PLA) were chosen as hydrophilic and hydrophobic side chain components, respectively. Brush hydrophilic ratio, expressed in terms of the weight fraction of PEG (w_{PEG}), was varied by changing the length of the PLA block (Table 2.1). Grafted PEG chains had a fixed molecular weight of 750 Da (PEG_{16}, subscript represents repeat units).

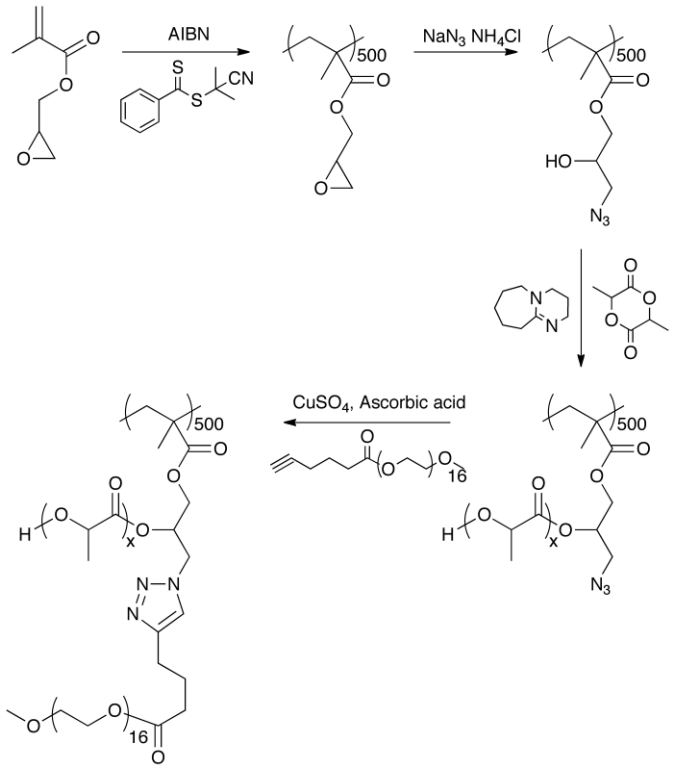

Scheme 2.1. Synthesis of molecular brushes with amphiphilic branched-side chains by a combination of "grafting from" and "grafting onto" routes.

2.3.2 Rapid Assembly of Amphiphilic Molecular Brushes

Self-assembly was triggered by a rapid change in solvent quality inside a multi-inlet vortex mixer (MIVM), which allows controllable changes in the magnitude and rate of solvent quality jump. We will refer to this assembly method as a rapid assembly process, to contrast it to conditions that favor thermodynamic equilibration (i.e., dialysis). In the MIVM, micromixing occurs in the millisecond range, thus providing a homogeneous environment for hydrophobic association to occur. Relevant process parameters include: i) the final non-solvent: solvent ratio (H_2O:THF, v/v); and ii) mixing velocity, expressed as the Reynolds number (Re), which could be calculated based on the velocities of all streams according to

$$Re = \sum_{i=1,N} \frac{V_i}{v_i} D$$

where D is the chamber diameter, V_i and v_i are the velocity and kinematic viscosity of the *n*-th inlet stream, and N the number of inlet streams.[28] Complete removal of the organic solvent was achieved by dialysis against water; dialyzed samples were imaged by transmission electron microscopy to examine assembly morphology.

Figure 2.8 (A through C) shows the resulting structures from the rapid self-assembly of molecular brushes with amphiphilic branched side chains as functions of w_{PEG}. The system with the highest PEG content ($PGMA_{500}$-*g*-(PEG_{16}/PLA_{11}) is characterized by forming homogeneous spherical micelles, with an average size of ~20 nm. Decreasing PEG content (w_{PEG} = 0.28) results in the formation of a cornucopia of toroidal structures coexisting with others, such as long rods, "8" shaped, and lassos. Finally, vesicles are obtained at the lowest w_{PEG}. As shown in Figure 2, a few of the

latter collapsed during the drying process for TEM sample preparation. Samples B and C in Figure 2.8 exhibit morphologies entirely different from the conventional spherical shapes generally produced by this method from linear diblock copolymer amphiphiles.[28,40,99]

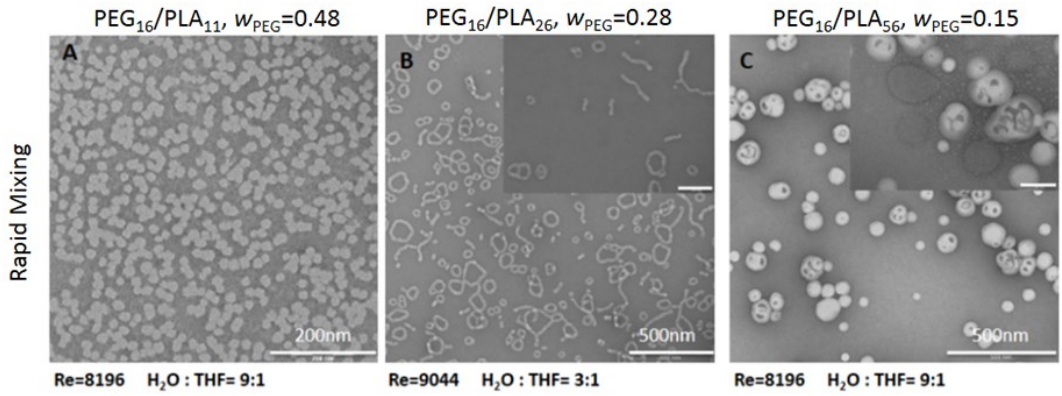

Figure 2.8. Transmission electron micrographs of aggregate morphologies of amphiphilic branched brush copolymers, prepared by a rapid mixing process. Differences in aggregate structure reflect the molecular characteristics of the block copolymers, with decreasing hydrophilic content from left to right. Samples A, B, and C correspond to PGMA$_{500}$-*g*-(PEG$_{16}$/PLA$_{11}$), PGMA$_{500}$-*g*-(PEG$_{16}$/PLA$_{26}$), and PGMA$_{500}$-*g*-(PEG$_{16}$/PLA$_{56}$), respectively.

2.2.3 Equilibrium Assembly of Amphiphilic Molecular Brushes

To further investigate the importance of medium conditions on the self-assembled structures from molecular brushes, we prepared samples by dialysis. This method differs from the rapid assembly both in the rate of solvent change and mixing energy. The resulting morphologies are also shown in Figure 2.9. While spherical micelles are also present for the sample with highest w_{PEG}, a few larger aggregates are also observed, leading to higher polydispersity than those obtained from rapid quenching in the MIVM. As w_{PEG} drops, a network of cylindrical micelles form and, compared

to its quenched equivalent, only a few toroidal structures are observed. The slow change in solvent quality results in the formation of a network-like structure and aggregates of rods, in contrast to the quenched sample wherein no large aggregates were observed (Figure 2.9B vs. Figure 2.8B). Lastly, giant vesicles were observed for the amphiphiles with the lowest PEG content, which were considerably larger than the equivalent bilayer aggregates formed by the rapid assembly method.

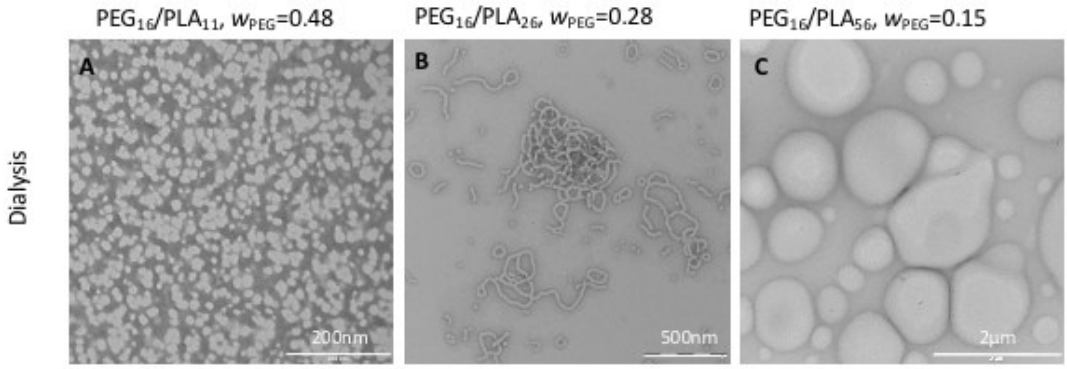

Figure 2.9. Transmission electron micrographs of aggregate morphologies of amphiphilic branched brush copolymers, prepared by dialysis. Samples A, B, and C correspond to PGMA$_{500}$-*g*-(PEG$_{16}$/PLA$_{11}$), PGMA$_{500}$-*g*-(PEG$_{16}$/PLA$_{26}$), and PGMA$_{500}$-*g*-(PEG$_{16}$/PLA$_{56}$), respectively.

Results from dynamic light scattering experiments of micellar and bilayer aggregates formed using the two assembly routes examined show that, when subject to a rapid change in solvent quality, aggregates exhibit monomodal particle size distribution curves (Figure 2.10). Under these conditions, aggregates are generally smaller and more monodisperse than those assembled under conditions favoring thermodynamic equilibration. These size distributions contrast to the bimodal (highly polydisperse) samples produced *via* dialysis. We attribute these morphological differences to a combination of shear effects and the rapid change in solvent quality.

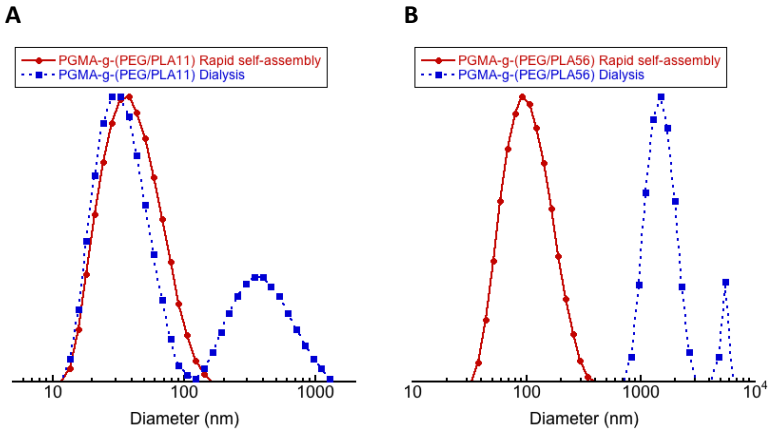

Figure 2.10. Particle size distributions of spherical particles from $PGMA_{500}$-*g*-(PEG_{16}/PLA_{11}) (**A**) and vesicles from $PGMA_{500}$-*g*-(PEG_{16}/PLA_{56}) (**B**), formed under conditions of rapid self-assembly and dialysis. Aggregates prepared under a rapid change in solvent quality generally exhibit narrower distributions and better control over size compared to the dialysis method that involves a slow change in solvent quality.

2.2.4 Self-assembly Mechanisms and Packing Geometries

Morphological diversity in the self-assembled forms of linear amphiphiles is dictated by a balance of the interfacial curvature between unlike blocks, solvent selectivity, and coronal interactions.[8,22,23,31,84,91] Prior work on linear amphiphilic polymers and rod shaped amphiphiles has shown that their morphological transitions, from spheres to cylinders and eventually to bilayer structures, occurs with decreasing hydrophilic fraction.[7,8,23] Interestingly, despite their difference in molecular structure, the morphological progression of brush amphiphiles on decreasing hydrophilic content parallels that of linear ones.[52] Since the amphiphiles examined have identical hydrophilic components (PEG_{16}) we exclude coronal repulsion effects as the determining factor. Instead, in analogy with linear amphiphiles, we attribute morphological diversity to the role of interfacial curvature or the interaction between dissimilar blocks. While the crowded grafted chains of molecular brushes would lead to a more rigid molecular structure compared to flexible linear diblock copolymers,

particularly for long grafts, they are able to adopt analogous aggregate forms.

To understand brush packing, static light scattering experiments were performed on spherical aggregates from $PGMA_{500}$-*g*-(PEG_{16}/PLA_{11}) (w_{PEG}=0.28), by comparing their molecular weight (1.62×10^6 Da) to that of the molecular brush (1.44×10^6 Da). The similarity between both suggests that the structures shown in Figure 2.8A consist of unimolecular aggregates. For unimolecular micelles, the hydrophobic backbone and PLA collapse to form the core in the presence of water while PEG chains stretch out and act as a steric stabilizing layer, preventing micelle fusion. As PLA length increases, PEG stabilization becomes insufficient for unimolecular structures, requiring brushes to undergo intermolecular association into a cylindrical morphology. Careful examination of the structures shown in Figure 2.8 A and B revealed that the average diameter of rods and toroids are similar to those of unimolecular micelles (~ 20-25 nm). Finally, a further decrease in hydrophilic fraction results in the formation of vesicles, in which case PEG chains stretch out from inside and outside the membrane to stabilize the hydrophobic interlayer.

2.2.5 Effects of Processing Parameters on aggregate morphology

$PGMA_{500}$-*g*-(PEG_{16}/PLA_{26}) forms an unusual toroidal morphology when assembled by a rapid and large change in solvent quality (Fig. 2.8 B). Morphological differences between this sample and that produced by dialysis suggest that the combined effect of shear forces and the rate and magnitude of solvent jump induce network separation and facilitate the end-to-end connection of cylinders into closed geometries. Shear

flow is known to influence ring formation,[90] and in our system the shear rate can achieve values of ~9300 s^{-1}, which we suspect is enough to influence structure formation particularly for worm-like aggregates. The sample prepared by dialysis was subject to vigorous stirring after assembly, however, no apparent differences were observed with respect to the non-stirred sample (Figure 2.11). Preservation of aggregate morphology despite energetic stirring suggests that shear effects and solvent quality change will conjunctly direct assembly morphology. Toroid formation via end-to-end connection of cylinders was recently shown for the co-assembled structures of graft copolymers and hydrophobic homopolymers,[100] and prior work on linear diblock copolymer self-assembly showed that external forces (e.g., shear flow) can direct structure formation.[90,101] To further investigate the process parameters leading to this unique morphology, we examined different assembly conditions.

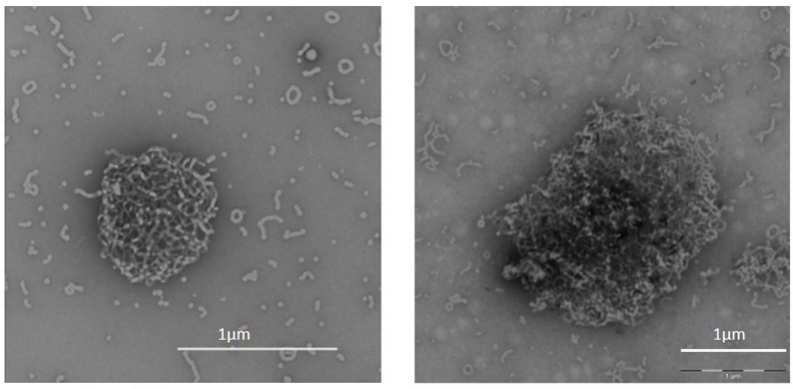

Figure 2.11. Network structure formed by the self-assembly of $PGMA_{500}$-*g*-(PEG_{16}/PLA_{56}) under dialysis showing the effect of stirring on aggregate morphology.

For nanoparticles formed by linear diblock copolymers, differences in aggregate size with final solvent content are related to brush repulsion characteristics and core

swelling.[40] We examined the effect of final solvent quality (non-solvent:solvent ratio) on aggregates from $PGMA_{500}$-*g*-(PEG_{16}/PLA_{26}) for three different ratios (3, 9 and 18) at relatively similar mixing velocities. The results are shown in Figure 2.8 B and 2.12 B and C (1B, 2B and C). We observe that, while toroid width remained relatively constant (~20 nm), its average diameter decreases with an increase in solvent quality. For the lowest solvent ratio, the majority of ring diameters exceed 100 nm, with some exceptions in the range between 50-100 nm. At intermediate ratios we see a decrease in average ring diameter to values between 50-100 nm, while at the highest ratio ring diameters take their lowest value (<50 nm). Noting that a better solvent quality (lower solvent jump) also results in a higher local polymer concentration during mixing suggests that both concentration and solvent quality may facilitate cylinder growth over end-to-end connection.

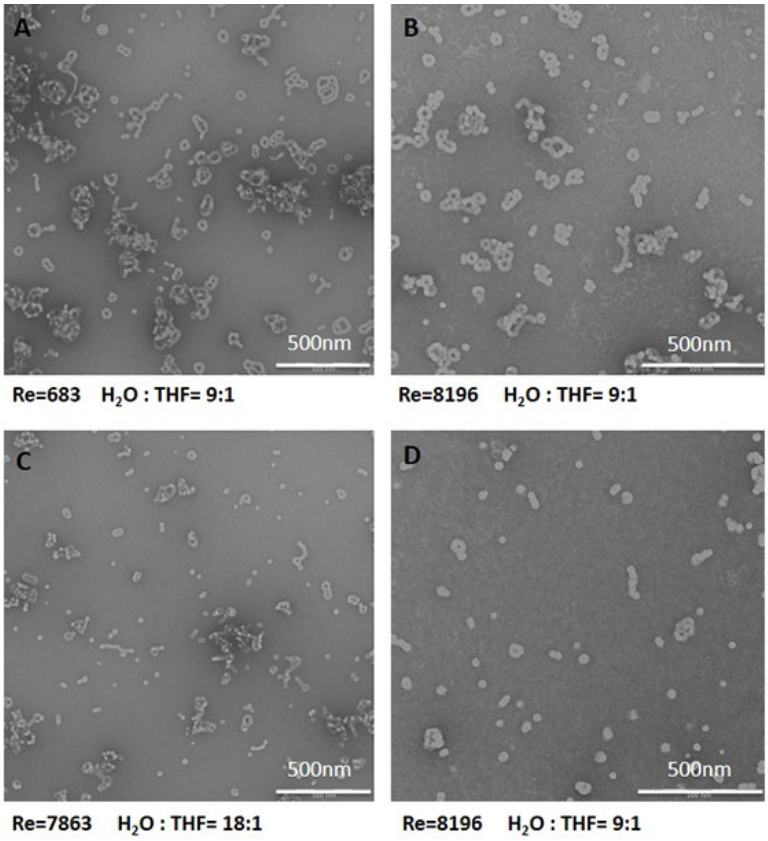

Figure 2.12. Transmission electron micrographs of aggregate morphologies of $PGMA_{500}$-*g*-(PEG_{16}/PLA_{26}), prepared by a rapid mixing process. The initial polymer concentration of samples A through C was 2.5 mg/mL, while sample D was prepared at 0.5 mg/mL. Reynolds number (Re) and final solvent quality (H_2O:THF) are specified in each case.

Assembly kinetics of linear diblock copolymers are also greatly influenced by mixing velocity.[40] We compared aggregate structures from samples prepared using the same solvent jump but with a large difference in mixing velocity (Fig. 2.12 A and B). While no apparent differences were observed in terms of feature diameters, we did notice mild aggregation for samples prepared with the lowest mixing velocity.

Finally, we compared the effect of initial polymer concentration on aggregate morphology, as shown in Figure 2.12 B and D. At lower initial concentration we

observed more short rods and spheres, and fewer closed structures, suggesting that a certain local concentration is necessary for cylinders to form closed structures, as previously discussed. Based on our observations we hypothesize that a certain cylinder length is necessary for toroid formation, which will be mediated by process parameters during mixing.

2.2.6 Effects of Molecular Brush Backbone Length on aggregate morphology

The self-assembly mechanism of grafted polymers is more complex than that of linear ones since it involves both intra- and intermolecular associations. Multi-domain nanostructures can result from the intermolecular association of brush macromolecules.[60] We suspect that the dimension of brush amphiphile intramolecular aggregates may also have impact on the final self-assembled nanostructures. Therefore, we further examined the assembled morphologies of molecular brushes possessing different molecular sizes. For this purpose, a series of molecular brushes with different PGMA (backbone) lengths were synthesized, while maintaining the side-chain lengths that lead to toroid-forming aggregates ($PGMA_{500}$-*g*-(PEG_{16}/PLA_{26})). PGMA repeat units ranged from 68 to 721, and their molecular properties are summarized in Table 2.4.

Table 2.4. Molecular characteristics of amphiphilic brush copolymers with different backbone repeat units.

	copolymer	M_n[a] (kg/Mol)	w_{PEG}
PGMA68	$PGMA_{68}$-*g*-(PEG_{16}/PLA_{34})	226.98	0.22
PGMA114	$PGMA_{114}$-*g*-(PEG_{16}/PLA_{32})	359.56	0.22
PGMA273	$PGMA_{273}$-*g*-(PEG_{16}/PLA_{33})	930.93	0.22
PGMA500	$PGMA_{500}$-*g*-(PEG_{16}/PLA_{26})	1453.00	0.28
PGMA721	$PGMA_{721}$-*g*-(PEG_{16}/PLA_{29})	2250.96	0.24

[a] Determined from ^{1}H NMR spectra.

Copolymer self-assembly was triggered by a rapid change in solvent quality, as described previously, under the same processing conditions (Re=9044, H_2O:THF=3:1). Assembly morphologies were examined by TEM and are provided in Figure 2.13. As observed in Figure 2.13 (C through E), it is evident that a longer backbone length favors the formation of rod-like and toroidal structures. In contrast, molecular brushes from shorter backbones ($PGMA_{68}$ and $PGMA_{114}$), result in spheres, as shown in Figure 2.13A and B. Toroidal species starts to appear when the DP of the backbone DP reaches 273, though a large population of rods and spheres are still observed. As brush size further increased (PGMA500 and PGMA721), more closed features were formed. More compound structures (interconnected toroids) were found for the longest backbone.

In order to understand the multimolecular packing geometry in toroidal assemblies, cylinder width was analyzed for all samples, and the results are provided in Figure 2.14. The results indicate that homogenous cylinder widths with small deviation were obtained in all cases. We noticed that similar widths were found in sample PGMA273

and PGMA721, whereas a smaller value was found in sample PGMA500. Careful inspection of brush amphiphiles reveals that the PLA length in PGMA500 is slightly shorter than the other two, and this difference was also reflected in its higher w_{PEG} (0.28). The small variation in hydrophilic/ hydrophobic balance among brush amphiphiles might influence both of their intra- and intermolecular association, resulting in different assembled feature sizes. Specifically, the lower hydrophilic ratio (w_{PEG}) seems to promote a higher level of intermolecular associations, leading to the formation of thicker cylinder. Hence, the width of toroid exhibits an inverse dependence on the w_{PEG} of brush amphiphiles.

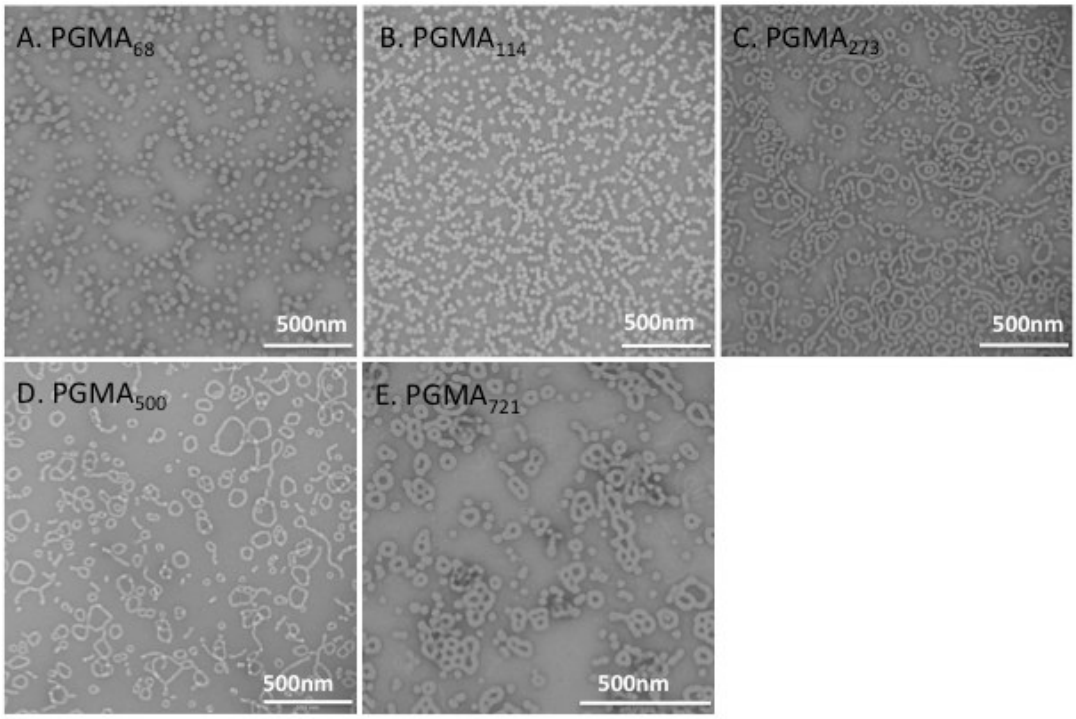

Figure 2.13 Transmission electron micrographs of aggregate morphologies of amphiphilic brush copolymers, prepared by a rapid mixing process. Differences in aggregate structure reflect the molecular characteristics of the block copolymers, with increasing backbone repeat units. Samples A-E correspond to molecular brushes with backbone DP of 68,114,273,500, 721 respectively.

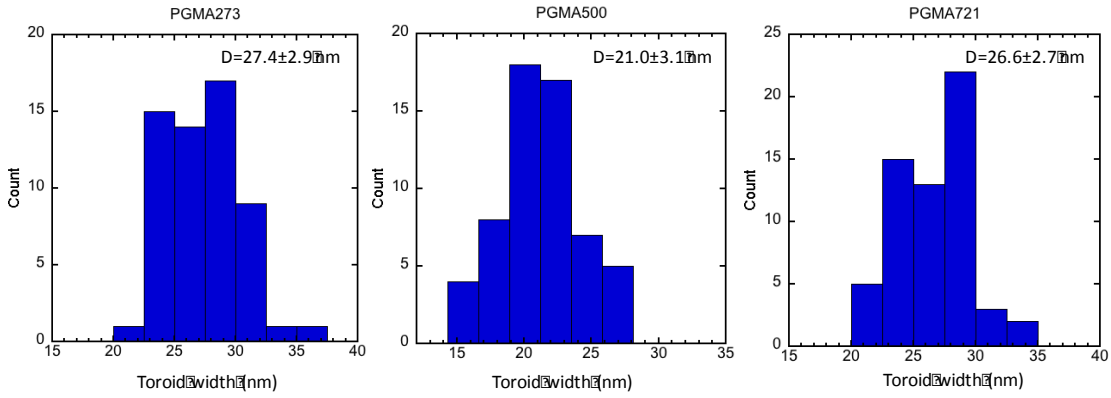

Figure 2.14. Widths of toroidal assembly from molecular brushes with different backbone repeating units. Samples were prepared with Water:THF=3:1 (25% THF), A-C correspond to PGMA273, PGMA500 and PGMA721 respectively.

2.4 Conclusions

A variety of self-assembled structures were obtained through manipulation of the amphiphilic character of a series of PLA/PEG-grafted molecular brushes, the morphological transitions of which were shown to parallel those of linear diblock amphiphiles. The combination of shear effects and a rapid and large change in solvent quality resulted in self-assembled structures distinct from those achieved under equilibrium conditions. More importantly, we report on the toroid formation from the self-assembly of molecular brush amphiphiles and the molecular and process parameters involved in their formation, demonstrating how kinetic features of the assembly process can be used to direct the formation of unique morphologies from architecturally complex macromolecules.

Chapter III: Self-assembly of Amphiphilic Branched Copolymers

3.1 Introduction

The solution-based assembly of amphiphilic copolymers has been developed as a promising way to fabricate nano objects, intended for potential application in the areas of drug delivery and bioimaging. In solution, the interactions between the solvent and unlike blocks induces the formation of well-defined nanostructures.[23] The resulting aggregates can increase the solubility of poorly water-soluble drugs by solubilizing them in their hydrophobic core, preventing their degradation by limiting their interaction with the surrounding environment, and stabilizing them through a hydrophilic corona, thus largely increasing their bioavailability and in vivo circulation time.[102] Linear amphiphilic diblock copolymers are among the most widely studied materials for these applications, and aggregate structures can be manipulated through chemical diversity as well as kinetic features of the assembly process.[7,32,88,101]

Advances in polymerization techniques have enabled access to polymers with more complex molecular architectures or topologies compared to linear chains, such as branched and graft structures.[58,61] Macromolecular architecture is a known determinant of the physicochemical properties of a polymer, including its degree of crystallinity, maximal melting temperature, etc.[48,77] The topological complexity of macromolecules is crucial parameter in aggregation and structure formation –as it may involve both intra- and intermolecular processes– while also influencing macromolecular interfacial behavior.[79] Polymer structure is known to play a crucial

role in determining conformational packing geometry within a micellar structure[103]. Hence, micellar morphologies and their physicochemical properties are greatly influenced by polymer structure.[49] Despite this, a full understanding of the (polymer) structure-(micelle) property relation, in the context of macromolecular architecture, is still lacking.[103]

The macromolecular nature of the building blocks, and their characteristically long time-scales, provides an additional handle to tune the properties of solution-based self-assemblies through the processing method. Examples of this include control the assembly pathway of charged amphiphilic block copolymers using a combination of solvent mixing and the complexation with divalent organic counter ions, generating kinetically trapped assemblies.[31] In another example, the external shear force exerted by an on-chip assembly process could offer sufficient energy to overcome repulsive interparticle potentials, resulting in assembled structures that are distinct from the off-chip equilibrium structure.[32] Lastly is the rapid self-assembly of a linear diblock copolymer into kinetically frozen nanoparticles, produced by a large and rapid change in solvent quality for the amphiphile solution. In this case, the rate of solvent quality change and the degree of supersaturation of the block copolymer (concentration above the critical micelle concentration) will determine the mechanism of assembly and particle size.[29] No prior work is known regarding the kinetics of aggregation of graft/brush-polymer systems, which as previously mentioned, become increasingly complex because of intra/intermolecular association phenomena.

Hydrophobic solutes, either molecularly dissolved or suspended, can be successfully

encapsulated in polymer nanoparticle cores produced by rapid self-assembly given that their nucleation/growth times and/or aggregation times are shorter than the time necessary to complete particle formation. The flexibility of rapid self-assembly allows loading of multiple solutes in the same particle, a feature that is difficult to achieve in traditional colloidal systems.[104]

In this Chapter, in order to establish a preliminary understanding of structure-property relation between branched copolymers and their assemblies, a group of amphiphilic branched copolymers with different macromolecular architectures, including molecular brush, graft and toothbrush-like copolymers were synthesized. These were designed such that they maintained the same hydrophilic content while varying their molecular architecture (i.e., side chain arrangement). This study encompasses their aggregation structures and micellar properties, assembly kinetics under different conditions (amphiphile concentration and mixing velocity), and their ability for solute stabilization through hydrophobic interaction.

3.2 Materials and Methods

3.2.1 Materials and Characterization

All reagents were commercially available and used as received unless otherwise noted. Glycidyl methacrylate (GMA, Aldrich 97%) was passed through a short basic alumina column to remove the inhibitor. Poly(ethylene glycol) methacrylate (PEGMa, sigma) was dissolved in a small amount of tetrahydrofuran and passed through a short basic alumina column to remove the inhibitor. 2,2′-Azobis(isobutyronitrile) (AIBN)

and D,L-lactide were recrystallized from methanol and anhydrous ethyl acetate, respectively. 1,8-Diazabicyclo[5.4.0]undec-7-ene (DBU) was kept over molecular sieves (3 Å) overnight. Deionized water was purified in a Barnstead Nanopure system to a final resistance of 18.2 mΩ; it will be referred to as Nanopure water.

Gel permeation chromatography (GPC) was performed on a Waters 1515 Isocratic HPLC equipped with two Styragel® columns (HR4, HR3, 300 mm x 7.8 mm) connected in series, a differential refractive index detector (Waters 2414) and a UV-visible detector (Waters 2489). HPLC grade tetrahydrofuran was used as the eluent, at a flow rate of 1 mL/min. Molecular weights are reported referenced to polystyrene standards (Shodex SL-105). ^{1}H NMR spectra were recorded on a Bruker AV 400 MHz spectrometer in either $CDCl_3$ or DMSO-d_6. Spectra were referenced to $CHCl_3$ (7.26 ppm) or DMSO (2.50 ppm). Bright-field transmission electron microscopy (TEM) was performed on a FEI Tecnai 12 TWIN transmission electron microscope operated at an acceleration voltage of 100 kV. TEM images were recorded by a SIS Megaview III wide-angle CCD camera. Carbon-coated copper grids (Electron Microscopy, Hatfield, PA) were ionized under plasma before sample preparation. Grids were placed on a drop of aggregate suspension (20 μL). After 5 min, the grid was washed under five drops of doubly distilled water and placed onto a drop (20 μL) of a 2 wt% aqueous uranyl acetate solution for 30 s. Grids were then blotted with filter paper and samples were allowed to dry at room temperature prior to imaging.

3.2.2 Synthesis of Amphiphilic Molecular Brushes

$PGMA_{68}$-g-(PEG_{16}/PLA_8) (**B1**)

Amphiphilic molecular brush **B1** was synthesized an approach similar to that described in Chapter II. A brief description of the steps involved (*i-iv*) is provided herein. *i*) GMA (3 mL, 0.022 mol), 2-cyano-2-propyl benzodithioate (CPB) (43.8 μL, 0.22 mmol,) and AIBN (3.68 mg, 0.022 mmol) were dissolved in 3.2 mL of benzene, and the mixture was bubbled with nitrogen for 1 h prior to reaction at 60 °C for 16 h. Polymerization was quenched by cooling the mixture in an ice bath and exposing the contents to atmosphere. Samples were diluted with dichloromethane and precipitated in methanol. The resulting precipitate was dried under vacuum. GPC: M_n=10.58 kDa, M_w/M_n=1.23. The degree of polymerization was estimated from monomer conversion. *ii*) Azidolysis of the resulting $PGMA_{68}$ was conducted by dissolving the backbone (1 g, 7.03 mmol epoxy groups) in 30 mL of *N*,*N*-dimethylformamide (DMF), followed by addition of sodium azide (1.37 g, 21.1 mmol) and ammonium chloride (1.13 g, 21.1 mmol). The reaction was conducted at 50 °C for 24 h. ^{1}H NMR signals indicate complete conversion. *iii*) $PGMA_{68}$-g-N_3 (240.7 mg, 1.3 mmol) and D,L-lactide (1.311g, 9.1mmol) were dried under high vacuum for ~5 h. After backfilling with nitrogen, anhydrous DMF was added to dissolve the reagents. DBU (39 μL, 0.26 mmol) was then injected, and the reaction was allowed to proceed for 1.5 h before quenching by addition of benzoic acid (79 mg, 0.65 mmol). The product was purified by precipitation into a mixture of water and methanol (1:1, vol.). *iv*) Alkynyl-terminated PEG_{16} was tethered onto this construct by a 'click' reaction, catalyzed by $CuSO_4$•$5H_2O$/ascorbic acid. The molar ratio of N_3, alkynyl groups, $CuSO_4$•$5H_2O$ and ascorbic acid was kept at 1:1:0.2:1. After complete dissolution in DMF, ascorbic acid

was added and the solution was bubbled with nitrogen for 30 min. $CuSO_4 \cdot 5H_2O$ was then added under nitrogen and the reaction proceeded for 12 h. Polymers were purified by dialysis against Nanopure water for 4 days and the final product was recovered by lyophilization. ^{1}H NMR spectra of products from each step are shown in Figure 3.1, and GPC chromatogram of final B1 is provided in Figure 3.6.

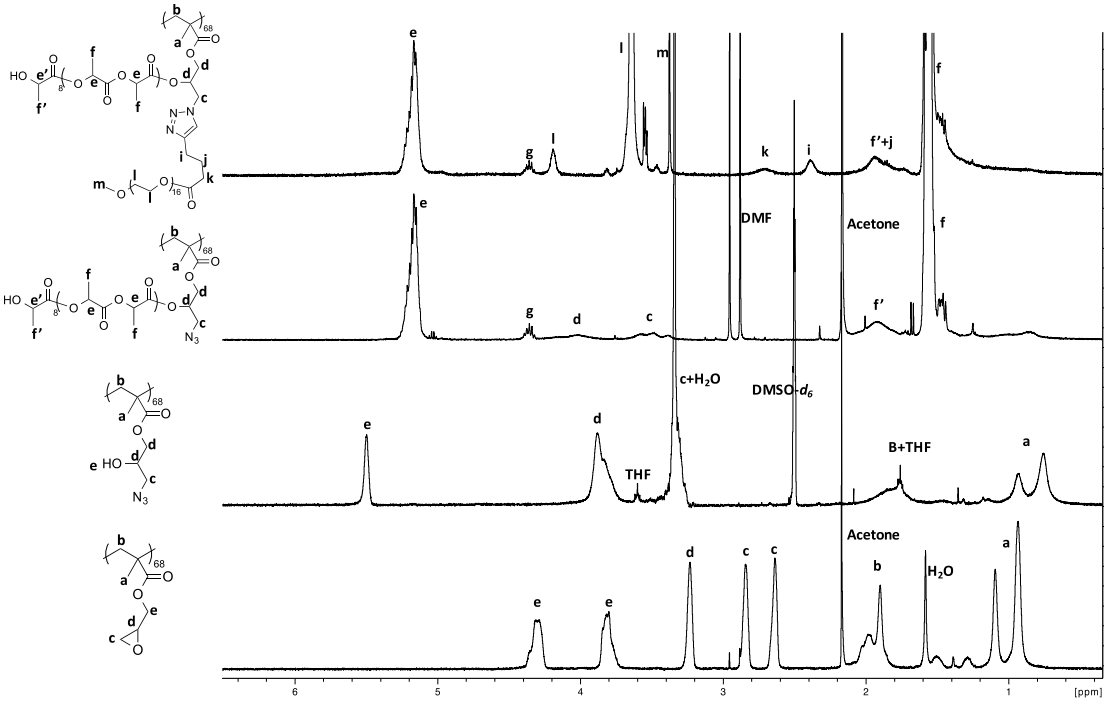

Figure 3.1. ^{1}H NMR spectra, and peak assignments, of products from each step of the synthesis of $PGMA_{68}$-*g*-(PEG_{16}/PLA_8).

P((GMA-g-PLA$_8$)$_{0.59}$-r-PEGMa$_{0.41}$)$_{126}$ (**B2**)

i) $P(GMA_{0.41}$-*r*-$PEGMa_{0.59})_{126}$ was synthesized by the RAFT copolymerization of poly(ethylene glycol) methacrylate ($PEGMa_{22}$, 22 repeat units of ethylene glycol) and GMA. Briefly, PEGMa (2 g, 1.87 mmol), GMA (330 μL, 2.5 mmol), 2-cyano-2-propyl benzodithioate (CPB) (6.9 mg, 0.031 mmol,) and AIBN (0.5 mg, 0.003 mmol)

were dissolved in 2.3 mL of DMF, and the mixture was bubbled with nitrogen for 1 h. The reaction was conducted at 85 °C for 40 h, quenched by immersing the flask in an ice bath and opening it to atmosphere. Aliquots were taken to evaluate monomer conversion. Samples were purified by dialysis against water for 3 days, followed by lyophilization to yield the final product. GPC: M_n=63.58 kDa, M_w/M_n=1.33. Conversions (92.5% GMA, 86.7% PEGMa) were determined based on monomers conversions, and DPs were calculated accordingly. *ii*) Azidolysis of P($GMA_{0.41}$-*r*-$PEGMa_{0.59}$)$_{126}$ (342.9 mg, 0.63 mmol epoxy groups) was carried out by dissolving the polymer in *N*,*N*-dimethylformamide (DMF, 16 mL), followed by addition of sodium azide (122.9 mg, 1.89 mmol) and ammonium chloride (101.1 mg, 1.89 mmol). The reaction was conducted at 50 °C for 24 h. The product was purified by dialysis against water for 2 days, and then recovered by lyophilization. ^{1}H NMR signals indicated complete conversion. *iii*) P((GMA-*g*-N_3)$_{0.59}$-r-$PEGMa_{0.41}$)$_{126}$ (200.6 mg, 0.21 mmol hydroxyl groups) and D,L-lactide (262.7 mg, 1.82 mmol) were dried under high vacuum for ~5 h. After backfilling with nitrogen, anhydrous DMF was added to dissolve the reagents. DBU (10 μL, 0.067 mmol) was then injected, and the reaction was allowed to proceed for 1.5 h before quenching by addition of benzoic acid (20.5 mg, 0.17 mmol). The polymer was purified by dialysis against Nanopure water for 3 days, and the final product was recovered by lyophilization. ^{1}H NMR spectra of products from steps *i*-*iii* are shown in Figure 3.2, and GPC chromatogram of final B1 is provided in Figure 3.6.

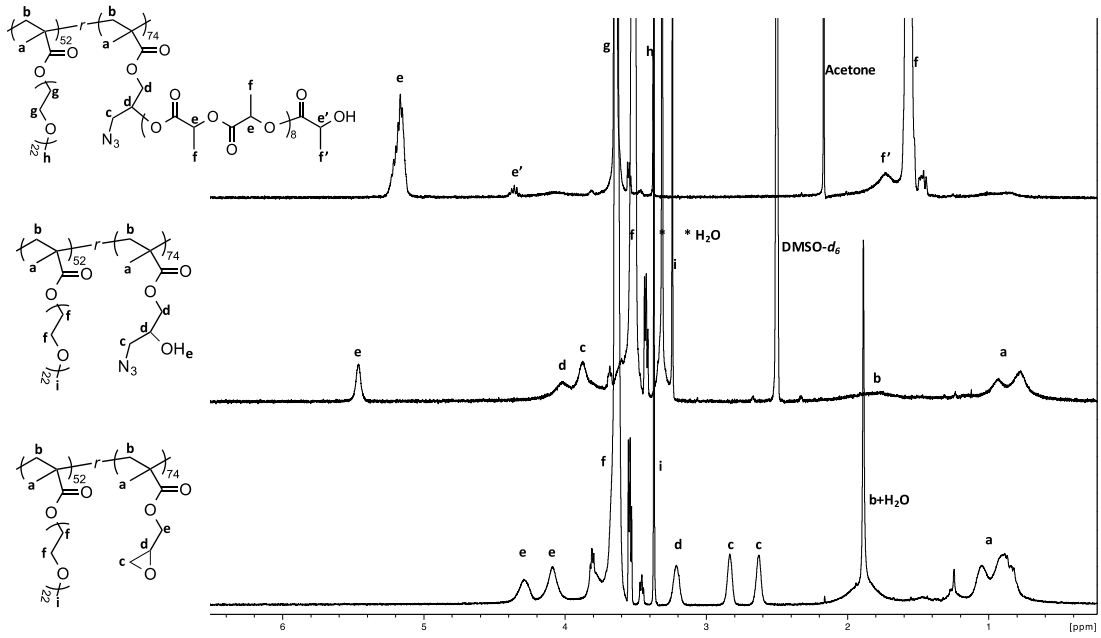

Figure 3.2. ^{1}H NMR spectra, and peak assignments, of products from each synthesis step of P((GMA-*g*-PLA$_8$)$_{0.59}$-*r*-PEGMa$_{0.41}$)$_{126}$.

P(GMA$_{0.93}$-r-PEGMa$_{0.07}$)$_{69}$ (**G1**)

GMA (0.75 mL, 5.6 mmol), PEGMa$_{22}$ (530 mg, 0.5mmol), 2-cyano-2-propyl benzodithioate (CPB) (15.7 mg, 0.007 mmol,) and AIBN (1.2 mg, 0.007 mmol) were dissolved in 1.5 mL of DMF, and the mixture was bubbled with nitrogen for 1 h. The reaction was conducted at 85 °C for 16 h, quenched by immersing the flask in an ice bath and opening it to atmosphere. The polymer was dialyzed against water for 4 days, and the final product was recovered by lyophilization. Conversions of GMA and PEGMa$_{22}$ were 93.8% and 85.7% respectively, calculated based on ^{1}H NMR. ^{1}H NMR and GPC chromatogram of the final product are shown in Figure 3.3 and Figure 3.6 respectively.

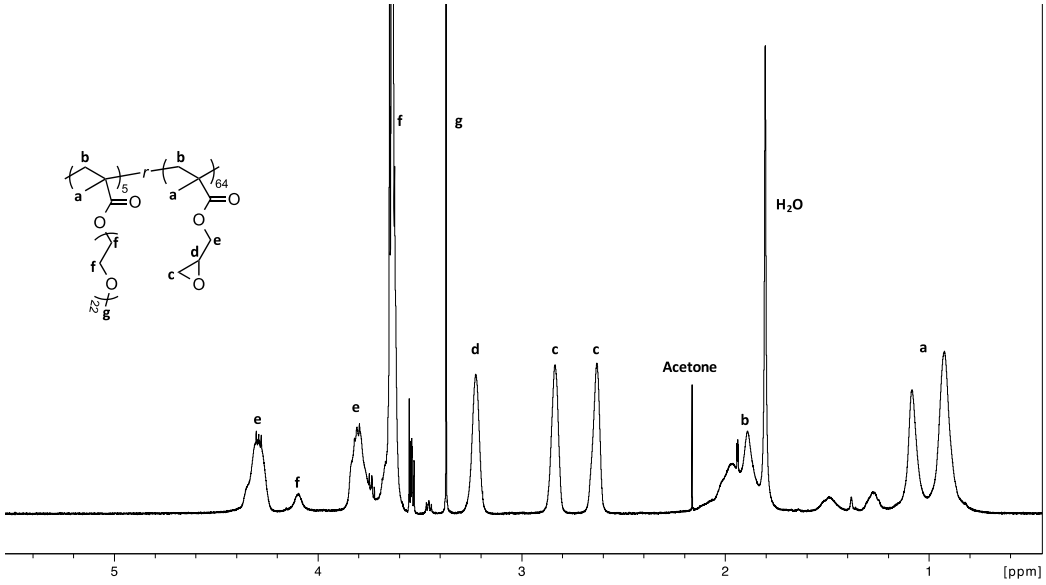

Figure 3.3. ^{1}H NMR spectrum, and peak assignments, of P(GMA$_{0.93}$-*r*-PEGMa$_{0.07}$)$_{69}$.

PGMA$_{75}$-b-PPEGMa$_{6}$ (**T1**)

PGMA$_{75}$ macro CTA was obtained as follows. *i*)GMA (4 mL, 0.030 mol), 2-cyano-2-propyl benzodithioate (CPB) (66.9 mg, 0.30 mmol,) and AIBN (4.9 mg, 0.03 mmol) were dissolved in 4 mL of benzene, and the mixture was bubbled with nitrogen for 1 h prior to react at 60 °C for 16 h. Polymerization was quenched by immersion in an ice bath and exposure to atmosphere. The sample was diluted with dichloromethane and precipitated in methanol. *ii*) The sequential RAFT polymerization of PEGMa$_{22}$ was conducted by dissolving PEGMa (601.1 mg, 0.56 mmol), PGMA$_{75}$ (1 g, 0.09 mmol) and AIBN (1.5 mg, 0.009 mmol) together in DMF (3 mL). The reaction was conducted at 85 ^{o}C under nitrogen for 3 days, and aliquots were taken to examine PEGMa$_{22}$ conversion prior to stopping reaction. The polymer was then dialyzed against water for 4 days, and the final product was recovered by lyophilization. The conversions of PEGMa$_{22}$ was 85%, calculated based on ^{1}H NMR. The degree of polymerization of PEGMa$_{22}$ was determined accordingly. ^{1}H NMR spectra of

products from *i* and *ii* are shown in Figure 3.4. A GPC chromatogram of the final product is provided in Figure 3.6.

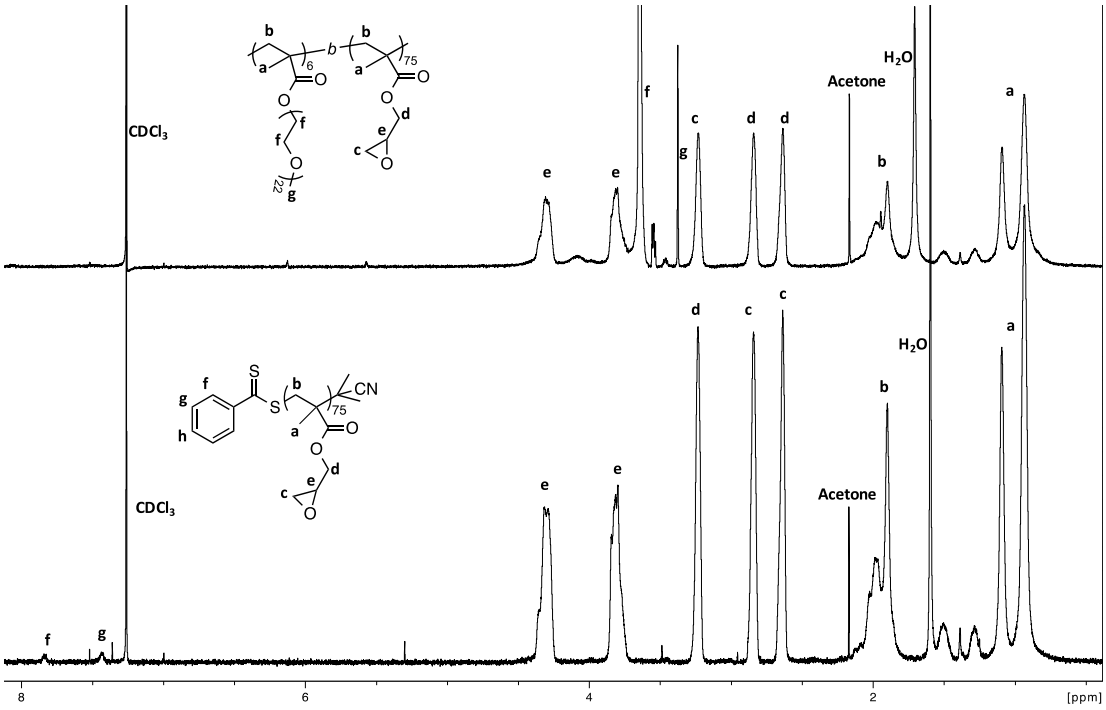

Figure 3.4. ^{1}H NMR spectra, and peak assignments, of products from each synthesis step of PGMA$_{75}$-*b*-(PPEGMa$_{22}$)$_6$.

PGMA$_{72}$-b-PPEGMa$_{14}$ (**T2**)

PGMA$_{72}$ macro CTA was obtained as follows. *i*) GMA (3 mL, 0.023 mol), 2-cyano-2-propyl benzodithioate (CPB) (62.8 mg, 0.3 mmol,) and AIBN (4.7 mg, 0.03 mmol) were dissolved in 3 mL of benzene, and the mixture was bubbled with nitrogen for 1 h prior to reaction at 60 °C for 16 h. Polymerization was quenched by cooling the reaction in an ice bath and exposing the contents to atmosphere. Samples were diluted with dichloromethane and precipitated in methanol. *ii*) PEGMa$_8$ (473.6 mg, 1.05 mmol), PGMA$_{72}$ (698.7 mg, 0.067 mmol) and AIBN (1.2 mg, 0.007 mmol) were

dissolved in DMF (3 mL). The reaction was conducted at 85 ºC under nitrogen for 3 days, and aliquots were taken to examine $PEGMa_8$ conversion prior to stopping the reaction. The polymer was dialyzed against water for 4 days, and the final product was recovered by lyophilization. Conversions of $PEGMa_8$ was 89.4%, calculated by ^1H NMR. The degree of polymerization of $PEGMa_8$ was determined by monomer conversion. ^1H NMR spectra of products from each step are shown in Figure 3.5. GPC chromatogram of final product is provided in Figure 3.6.

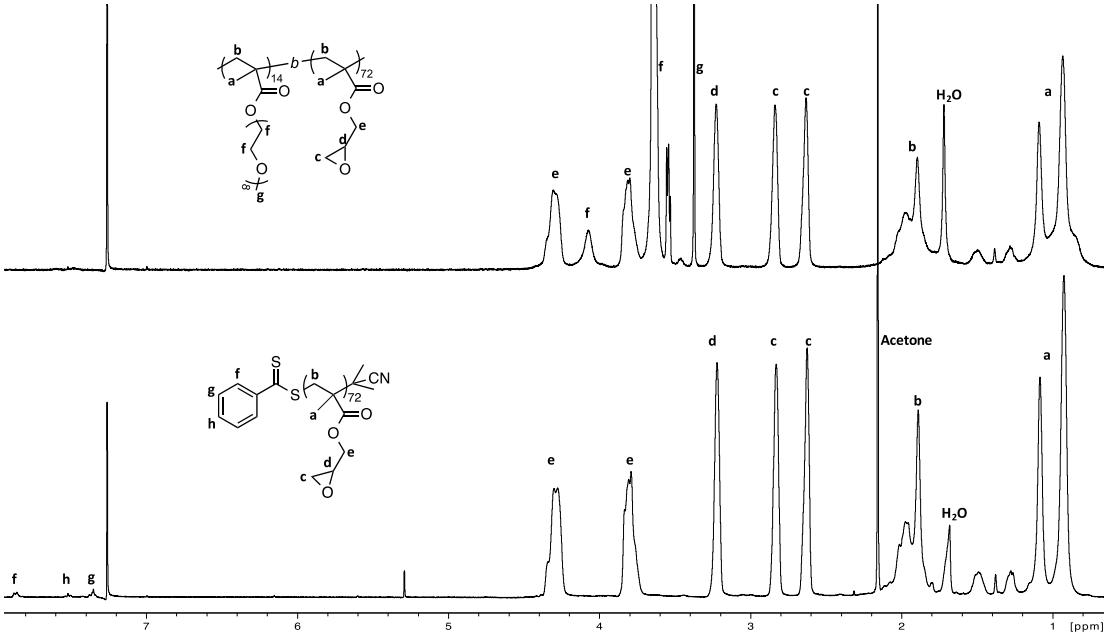

Figure 3.5. ^1H NMR spectra, and peak assignments, of products from each synthesis step of $PGMA_{72}$-*b*-$PPEGMa_{14}$.

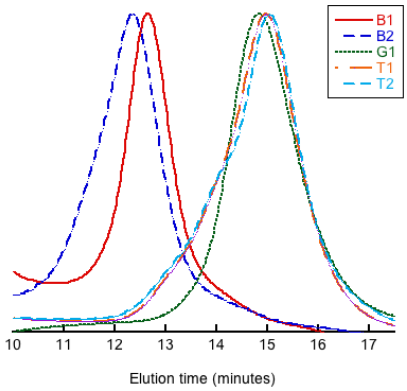

Figure 3.6. Gel permeation chromatograms of amphiphilic copolymers.

3.2.3 Critical micelle concentration

C_{CMC} of polymers were measured by using pyrene as a probe. For this, 50 µL of a pyrene solution in acetone (6×10^{-5} M) were loaded into a 5 mL scintillation vial and left open under the hood to allow for complete evaporation of the solvent. 50 µL of polymer solution (0.001 to 2 mg/ mL in acetone) were then added to each of 10 vials containing pyrene, followed by 1 mL of water. Final amphiphile concentration ranged from 50 µg/mL to 0.1 mg/mL. Samples were vigorously stirred with a vortex mixer (~ 1 min), and left to shake gently overnight to evaporate acetone. Excitation and emission spectra were recorded by fluorescence spectroscopy. Pyrene excitation was scanned from 300 to 360 nm at an emission wavelength of 390 nm. Excitation and emission bandwidths were set at 2 nm. The intensity ratio from the signals at 336 and 334 nm (I_{336}/I_{334}) was analyzed as a function of polymer concentration. C_{CMC} values were read from the intersection between curve tangents at low and high concentrations.

3.2.4 Self-assembly of Amphiphilic Copolymers

Self-assembly was carried out in a four-inlet vortex mixer, the details of which are provided elsewhere.[28] Nanopure water was charged into three 50 mL syringes (Hamilton, NJ) and the organic solution into a 10 mL syringe, and mounted on two separate syringe drivers (PHD Ultra, Harvard Apparatus). Polymers were dissolved in THF at 5 mg/mL. The THF: water volumetric ratio (solvent jump) used was 1:9 with mixing speeds of 12 mL/min and 108 mL/min for the organic and aqueous phases, respectively, resulted in final THF concentrations 10% (v/v). Samples were collected and dialyzed (6-8 kDa MWCO, Fisherbrand) against Nanopure water for 24 h at 20 °C. Water was replenished every 4 h throughout the dialysis process. Samples were stored in clean scintillation vials, and unless otherwise noted, kept under refrigeration at 4 °C.

3.2.5. Flash Nanoprecipitation

The protocol described above was used to prepare solute loaded nanoparticles, with the exception that both the polymers and Rose Bengal lactone (RBL) were dissolved together in tetrahydrofuran (prior to mixing). Polymer concentration was at 5 mg/mL, and solute concentration was 20% $w/w_{polymer}$. Dialyzed samples were collected and filtered through 0.45 μm PVDF syringe filters (Thermo Scientific) and stored in clean centrifuge tubes (Falcon® Tube). Loading capacity (LC) and efficiency (LE) in nanoparticles (NP) were estimated as:

$$Loading\ capacity\ (LC,\%) = \frac{Mass\ of\ solute\ in\ NP}{Mass\ of\ NP} \times 100$$

$$Loading\ efficiency\ (LE,\%) = \frac{Mass\ of\ solute\ in\ NP}{Mass\ of\ solute\ in\ feed} \times 100$$

LC and LE of RBL were determined with a Varian Cary 50 UV/Vis spectrophotometer (Agilent Technologies, Santa Clara, CA). Loaded micelles were lyophilized and the resulting powders were re-suspended in DMF. The concentration of RBL was calculated based on a calibration curve of RBL in DMF, referencing its absorbance at 558 nm.

3.2.6 PEG Exposure in Nanoparticles

A suspension of nanoparticles (10mL) was loaded into an Amicon Ultra centrifugal filter (100 kDa MWCO), and concentrated to < 100 μL by centrifugation at 5000 g for 25 min (Allegra 64R, Beckman Coulter). D_2O (600 μL) and methanol (3 μL, external standard) were then added, followed by homogenization by vortexing for 1 min. Samples were analyzed by ^1H NMR (Bruker AV 400 MHz) by transferring a known volume of concentrated sample (300 μL) into a clean Eppendorf tube, and mixing it with acetone-d_6 (1mL), and sonicating for 10 min. The samples were allowed to dissolve over 4 h and sonicated again for 10 min prior to analysis. The polymers, as unimers, were analyzed by ^1H NMR in acetone-d_6.

3.3 Results and Discussion

3.3.1 Synthesis of Amphipihlic Block Copolymers

To compare the structural effects of amphiphilic copolymers on the properties of their

aggregates, five copolymers possessing different molecular architectures, but with similar hydrophilic content, were synthesized. Poly(ethylene glycol) (PEG) was chosen as hydrophilic side chain component, with poly(D,L-lactide) (PLA) and/or poly(glycidyl methacrylate) (PGMA) composing the hydrophobic parts. The molecular structures of resulting copolymers are illustrated in Scheme 3.1. Subscripts represent the number of repeat units.

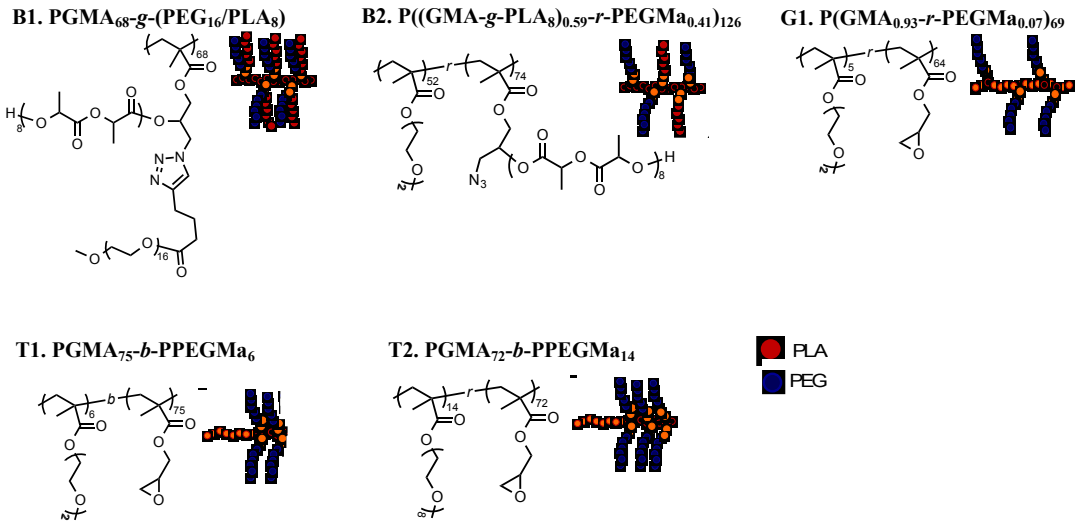

Scheme 3.1. Molecular structures and illustrations of molecular architectures of amphiphilic molecular brushes **B1** and **B2**, graft copolymer **G1** and toothbrush-like copolymers **T1** and **T2**.

According to their grafting density and side chain arrangement, copolymers are grouped into three types: (i) molecular brushes **B1** and **B2** ($PGMA_{68}$-*g*-(PEG_{16}/PLA_8) and P((GMA-*g*-PLA_8)$_{0.59}$-*r*-$PEGMa_{0.41}$)$_{126}$, respectively) for which there are one or more grafts per backbone repeat; (ii) graft copolymer **G1** (P($GMA_{0.93}$-*r*-$PEGMa_{0.07}$)$_{69}$) which has PEG side chains sparsely attached along the PGMA backbone; (iii) toothbrush-like copolymers **T1** and **T2** ($PGMA_{75}$-*b*-$PPEGMa_6$ and $PGMA_{72}$-*b*-

PPEGMa$_{14}$, respectively) which have PEG brushes densely grafted at one end of the backbone, bearing more resemblance to a block copolymer.

The ratio between unlike blocks is an important factor that influences the properties of amphiphilic self-assemblies.[8] Herein, to better understand the effect of amphiphile architecture on self-assembly properties, we maintained the hydrophilic ratio (w_{PEG}) constant. Based on earlier results, we targeted w_{PEG} at ~ 30%,[105] to promote the formation of spherical aggregates. The molecular characteristics of all amphiphilic copolymers used in the study are summarized in Table 3.1, from where it can be seen that w_{PEG} narrowly varied between 31.0% to 34.6% among all samples.

Table 3.1. Molecular characteristics of amphiphilic copolymers used in the study.

copolymer	M_n [a] (kg/mol)	M_w [b] (kg/mol)	$Đ$[b]	w_{PEG}[a] (% *w*t)
B1	84.83	153.54	1.20	33.2
B1	128.85	128.85	1.26	32.0
G1	17.81	111.78	1.29	34.0
T1	21.04	17.06	1.40	34.6
T2	20.57	16.55	1.39	31.0

[a]Determined from ^{1}H NMR spectra. [b]Measured by gel permeation chromatography.

3.3.2. Self-assembly of Amphiphilic Copolymers

Self-assembly of amphiphilic copolymers was triggered by a rapid and large change in solvent quality inside a multi-inlet vortex mixer (MIVM). More details regarding this method were provided in Chapter II. High Reynolds number (Re>2000) were used in this experiment to achieve homogenous mixing, and the final non-solvent: solvent ratio (H_2O:THF, v/v) was kept at 9:1. All nanoparticles were dialyzed to

remove THF prior to characterization.

Figure 3.7 shows aggregate structures obtained from the three types of amphiphilic copolymers, which consisted exclusively of spherical particles. However, subtle differences exist among samples, reflected in their average size and quality. Relatively mono-dispersed spheres were observed in assemblies from **B1**, **B2**, **T1** and **T2** (Figure 3.7 A, B, D and E), whereas larger aggregates were present in **G1** (Figure 3.7 C). The difference between **G1** and the rest is that its PEG branches were more loosely distributed along the backbone, whereas for the others the density of PEG grafting is higher, either along the backbone or in one localized area of the backbone. The higher local density of PEG side chains promotes their overlap,[106] and a higher packing of PEG on nanoparticles surface might further increase the stability of assembled structures.

Sizes of brush- and toothbrush-based assemblies were measured by TEM. The average particles size of **B1** and **B2** assemblies is ~ 23.5 nm. However, despite the much smaller molecular weight in toothbrush-like molecules, larger particles sizes were found for these systems (26.4 nm for **T1** and 27.5nm for **T2**). The corresponding size distributions of nanoparticles were provided in Figure 3.7 F, wherein narrow distributions were observed for all samples. Similar with TEM analysis, smaller particle sizes were found for brush samples. The smaller size of brush assemblies might be directly related with their unique molecular architecture, wherein the dense grafting results in less intermolecular entanglement,[57] resulting in smaller particles with lower aggregation numbers. The small peaks observed at larger sizes are

attributed to contaminants (dust) since large aggregates were not visualized by TEM.

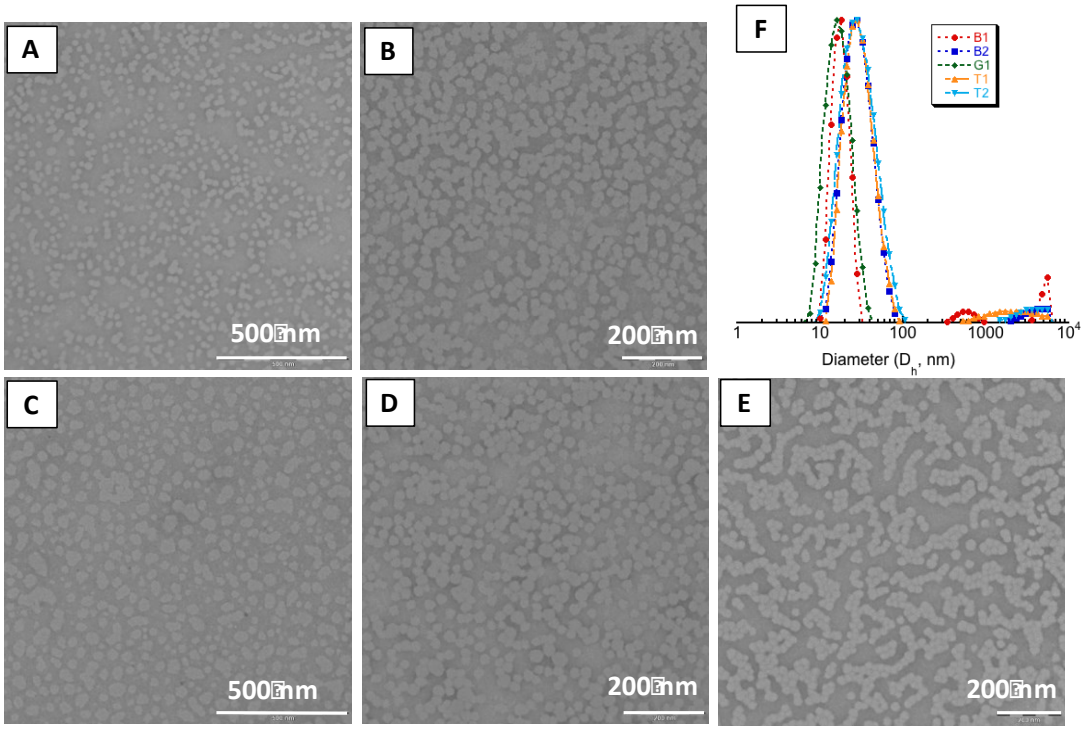

Figure 3.7. (A-E) Transmission electron micrographs of aggregate morphologies of amphiphilic copolymers, prepared by a rapid mixing process. (A-E) correspond to polymer B1, B2, G1, T1 and T2 respectively. (F) Dynamic light scattering distributions of nanoparticles from all copolymer samples, corresponding to image (A-E).

3.3.3 Properties of Micelles from Different Amphiphiles

The critical micelle concentration (CMC) is the minimum concentration required for amphiphiles to form micelles in solution. The CMC is used to characterize the thermodynamic stability of micelles, and a lower C_{CMC} indicates a higher thermodynamic stability in micelle systems.[18] C_{CMC} is related with molecular compositions of amphiphiles, wherein a longer hydrophobic block and higher density of surface PEG normally result in a lower C_{CMC}.[18] C_{CMC} values for all copolymers are

summarized in Table 3.2. While low C_{CMC} were obtained for all, their values differ according to chain architecture despite similarity in w_{PEG}. Small variations among C_{CMC} values of samples **B2**, **G1** and **T1** were observed, however the more dramatic effects of chain architecture were found for **B1** and **T2**, which exhibit the lowest and highest C_{CMC}, respectively. **B1** has the highest PEG grafting density, whereas **T2** has the shortest PEG branches. These observations suggest that higher PEG grafting density as well as longer PEG branches might be desired for a more thermodynamically stable micellar system.

Table 3.2. Micellar properties of amphiphilic copolymers.

copolymer	CMC[a] (10^{-3} mg/mL)	PEG exposure %[b]	Supersaturation
B1	2.95	43.33	169.5
B2	4.44	83.13	112.6
G1	5.03	92.98	99.4
T1	5.04	62.89	99.2
T2	7.49	--	66.8

[a] Determined by fluorescence spectroscopy. [b] Calculated from ^{1}H NMR measurement of PEG proton signal of micelles in D_2O versus in $CDCl_3$.

Having established the C_{CMC} of all polymers, their self-assembly was carried out by a rapid change in solvent quality. A single polymer concentration was used for nanoparticle formation, which translates into different supersaturations depending on the C_{CMC} of the polymer. Supersaturation is defined as the ratio of initial unimer concentration, with respect to its C_{CMC},[29] and the resulting values are also presented in Table 3.2. A high initial supersaturation (S_o > 100) is crucial in the rapid self-assembly of copolymers, wherein self-assembly proceeds by a diffusion-limited fusion mechanism, producing kinetically arrested nanoparticles.[29]

The core-shell structure of the resulting nanoparticles was examined by NMR studies of their suspension in D_2O. For all the samples studied here (**B1**, **B2**, **G1**, **T1**), only the PEG signal was visible by ^1H NMR, (PLA and/or PGMA signals were absent), supporting that core-shell nanoparticles were formed, with PLA and PGMA forming the hydrophobic core, and PEG serving as the protecting shell. PEG exposure was quantified by comparing the amount of PEG on micelle surface (in D_2O) with the total PEG amount of unimers dissolved in a good solvent (acetone-d_6), using methanol as an external standard. It could provide further insights into how efficiently the PEG component participates in the steric stabilization process. As shown in Table 3.2, nanoparticles from both **B2** and **G1** exhibit ideally high PEG exposure (83.13% and 92.98%, respectively), whereas lower exposures were observed for **B1** and **T1** (43.13% and 62.89, respectively). Surprisingly, the molecular brush **B1** shows the lowest PEG exposure (43.33%), which we suspect is related its crowded grafting, as well as short PEG branches. PLA is known to have good miscibility with PEG,[19] and the vicinity of PEG and PLA chains in **B1**, could further induce the insufficient phase segregation between PEG and PLA in aqueous environment. Consequently, more PEG might be buried inside the PLA core or within the PLA/ PEG interface, rather than extending out to the aqueous phase.

3.3.4 Rapid Assembly Kinetics

In the rapid self-assembly of amphiphilic diblock copolymers, nanoparticle formation occurs according to a diffusion-limited growth mechanism, wherein evolution occurs by unimer diffusion and coupling and small micelle fusion (small micelle refers to aggregates of dimers or trimers). In this process, the characteristic aggregation time of

the copolymer is given by the characteristic time of unimer coupling, given by the distance traveled by a unimer and its diffusion coefficient. The average distance that a unimer has to diffuse in solution is on the order of $\left[\frac{(N_A + N_B)}{C}\right]^{1/3}$, where N_A and N_B are measures of is the block length of the hydrophobic (A) and hydrophilic (B) blocks (i.e., the number of A and B segments), and c is the bulk concentration of the polymer (i.e., the number of chains per volume). From this it follows that the characteristic time for unimer coupling is $\tau_{dif}^{un} \approx \left[\frac{N_A + N_B}{c}\right]^{2/3} \frac{1}{D_o^{un}}$, where D_o^{un} is the diffusion coefficient of chain.[24] In an explicit form, the diffusion coefficient is given by $D_o^{un} = \frac{kT}{\eta_s N_B^v \upsilon^{1/3}}$. Likewise, the distance small micelles diffuse in semi-dilute media is $\left[\frac{Q(N_A + N_B)}{(c - c_{cmc})}\right]^{1/3}$, where Q is the aggregation number and c_{cmc} is the critical micelle concentration. Thus, the characteristic time for fusion of small micelles is $\tau_{dif}^{o} \approx \left[\frac{Q(N_A + N_B)}{(c - c_{cmc})}\right]^{2/3} \frac{1}{D_o^{mic}}$. Diffusion coefficients of unimer and small micelles are $D_o^{un} = \frac{kT}{\eta_s N_B^v \upsilon^{1/3}}$ and $D_o^{mic} = \frac{kT}{\eta_s N_B^v \upsilon^{1/3} Q^{1/5}}$, respectively. In terms of the Kuhn statistical length, a, and the bulk solution volume fraction of the polymer, ϕ_o, the distance of a chain must travel is given by $\frac{a}{\phi_o}$, and therefore, the characteristic time is $\tau \approx \frac{a^2}{D\phi_o^2}$.

According to the diffusion-limited mechanism, what follows is brush penetration by

unimers which has a much longer time scale (> 1000 ms) compared to that required for diffusion to nucleate a new particle (~ 10 ms). Nanoparticles growth essentially ceases when the hydrophilic component on the surface of the particles reaches the overlapping brush regime. At this point, particles are considered to be kinetically frozen.[29] In this sense, the starting concentration of block copolymer should have little effect on the final critical size of the particles. However, a higher starting concentration decreases the length scale between molecules, or the diffusion time, and a decrease in characteristic aggregation time could be expected according to equation 3.1.[29] Furthermore, the molecular characteristics of the copolymer would also be expected to influence the aggregation time as it is an explicit function of its molecular weight and its diffusion coefficient, which itself depends on molecular weight.

This mechanism was established by examining the self-assembly of a poly(*t*-butyl acrylate)-*b*-poly(acrylic acid) diblock copolymer with block sizes of 7.5 kg/mol for both blocks. The characteristic assembly time of this copolymer was found to be 26 to 60 ms, estimated by the use of an analytical confined impinging jet (CIJ) mixer.[29] The dependence of mixing time on Reynolds number and geometry in a confined impinging jet (CIJ) mixer was established, using the conversion of competitive reactions, and the characteristic mixing time is found to be proportional to the inverse of the velocity to the three halves power.[107] For the MIVM used in our rapid mixing process, sufficient micromixing could be achieved at Re > 1600, where the characteristic mixing time of the MIVM is in the range of milliseconds.[28] The Reynolds number (Re) could be calculated based on the velocities of all streams

according to $\mathrm{Re} = \sum_{i=1,N} \frac{V_i}{v_i} D$, where D is the chamber diameter, V_i and v_i are the velocity and kinematic viscosity of the *n*-th inlet stream, and N the number of inlet streams.[28]

We examined the rapid self-assembly of amphiphilic copolymers **B1** and **T2** by relating mixing velocity (Re) and particle size, to provide a scope of the contribution of structural features of the copolymer on its self-assembly kinetics. In this study, the final non-solvent:solvent ratio (H_2O:THF, v/v) was kept at 9:1, and nanoparticle samples containing 10 % THF were characterized by dynamic light scattering. Nanoparticles were prepared by varying the Re from ~ 300 to ~ 13,000. Hydrodynamic diameters (D_h) of the resulting particles were recorded and plotted against Re. The same procedure was repeated for a range of copolymer concentrations with a three-fold difference, from 5 mg/ mL to 15 mg/mL (0.5 wt % - 1.5 wt %).

As shown in Figure 3.8 A and B, nanoparticle size is a function of Re for both copolymers, dropping with an increase in Re until reaching a breakpoint, above which size becomes independent of mixing velocity. Interestingly, **B1** –a brush copolymer with hydrophilic and hydrophobic units pendant from each repeat unit of the backbone– behaves analogous to linear diblock copolymers by exhibiting essentially no variability in particle size ($\Delta D_h \pm 2$ nm) with polymer concentration. On the other hand, **T2** –the toothbrush copolymer with an isolated PEG brush domain– shows a very strong dependence of particle size with respect to polymer concentration ($\Delta D_h \pm$ 14 nm), particularly for the lowest concentrations. One possibility is that, at the final

solvent conditions (10% solvent), the lowest concentration of T2 (5 mg/mL) is close to its critical micelle concentration, and nanoparticle growth would therefore not be expected to follow the proposed mechanism since it is based on the premise of starting with a solution of unimers well above their critical micelle concentration. When we compare their supersaturation, defined as the ratio of the bulk polymer concentration to its C_{CMC}, that of **T2** at 5 mg/mL is only $S_{\mathbf{T2}} = 67$, compared to $S_{\mathbf{B1}} = 170$. At 7.5 mg/mL, $S_{\mathbf{T2}} = 100$, which is closer to the predicted supersaturation for diffusion-limited self-assembly ($S > 100$),[29] and the average particle size is closer to the values attained at the two highest concentrations, for which $S_{\mathbf{T2}} > 133$ and particle size is relatively insensitive to concentration. Nevertheless, a clear difference in particle size between **B2** and **T2** is observed at the highest concentration ($\Delta D_h \pm 10$ nm), which reflects differences in the molecular characteristics of the polymers.

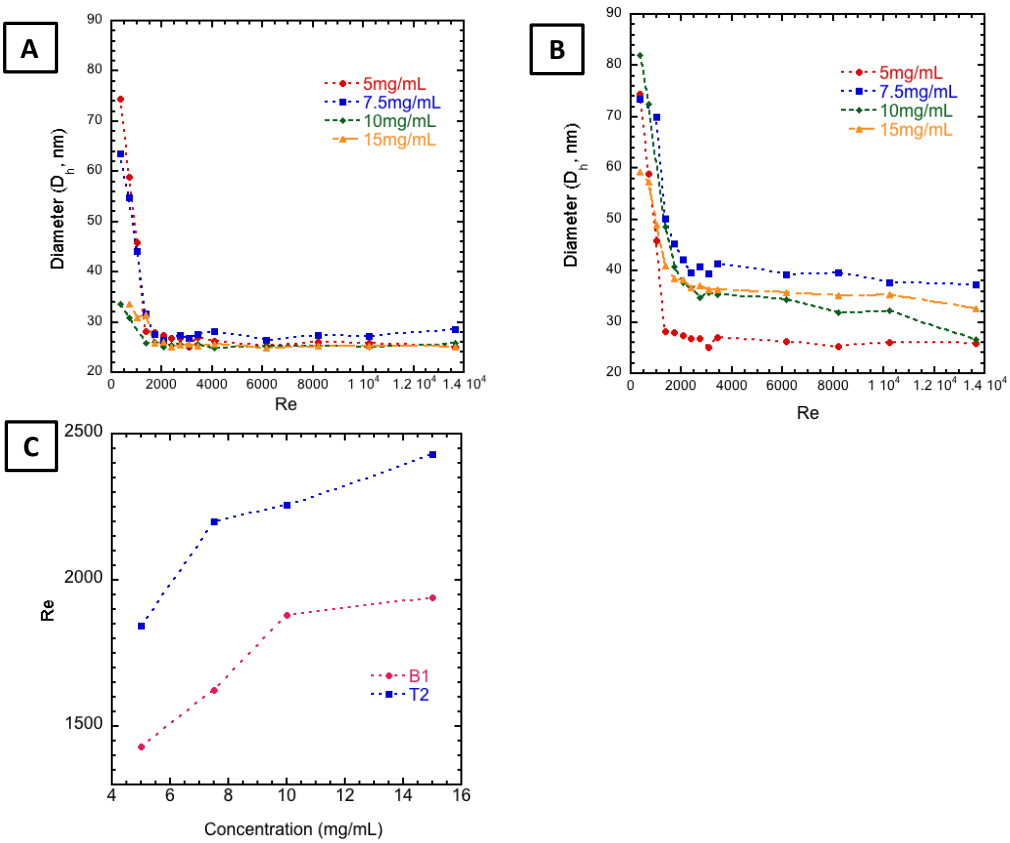

Figure 3.8. Rapid mixing of copolymers **B1** (A) and **T2** (B) with the aid of a MIVM, with Re ranging from ~ 300 to ~ 13,000. The resulting hydrodynamic diameters of particles, determined by dynamic light scattering, were shown to be dependent on Re. (C) The break point positions of copolymers as functions of copolymer concentration for **B1** (red) and **T2** (blue).

3.3.5 Copolymers as Hydrophobic Solute Stabilizer

Finally, the branched copolymers were further studied as stabilizers for a hydrophobic solute. Rose Bengal lactone (RBL) (clogP = 9.31), a known potent inhibitor of kinesin and an effective sensitizer of singlet oxygen,[108,109] was selected as the model drug. RBL was loaded into brush micelles in a similar rapid assembly process, except for the fact that the drug and amphiphiles were dissolved together in tetrahydrofuran, prior to the rapid mixing process. Solute feed was kept at 20% w/w_P. Molecular brushes **B1** and **B2**, and the graft copolymer **G1** were selected as stabilizer candidates,

so as to compare the effect of grafting density on stabilization properties.

Morphologies of solute nanoparticles were recorded by TEM, provided in Figure 3.9. For molecular brush **B1**, monodisperse solute nanoparticles were observed, and there is a small increase in nanoparticle size after solute loading (from 23.5nm to 24.6nm, according to TEM). However, for molecular brush **B2**, heterodisperse nanoparticles were found in the loaded samples, exhibiting a smaller average size (~18.1 nm) compared with the empty ones (~23.5 nm). Similarly, in the graft copolymer **G1**, small particles with poorly defined structure were observed.

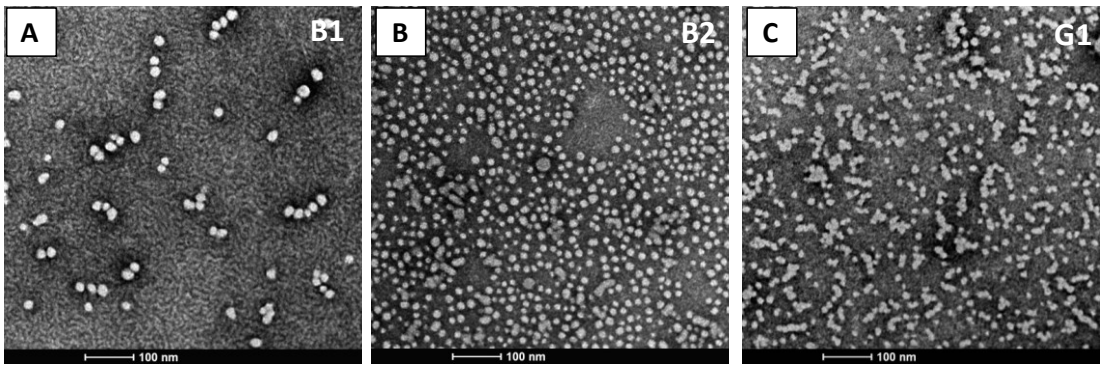

Figure 3.9. Transmission electron micrographs of RBL nanoparticles, stabilized by amphiphilic copolymers, prepared by a rapid mixing process. A, B and C correspond to polymer **B1**, **B2**, and **T1** respectively.

The loading capacity (*LC%*) and loading efficiency (*LE%)* of RBL from the different copolymers were compared and summarized in Table 3.3. High *LC%* and *LE%* were demonstrated by both molecular brushes **B1** and **B2**, while much lower values were recorded in the loosely grafted **G1**. The higher solute stabilization capability in molecular brushes might be attributed to the their higher local concentration of hydrophobic chains, which may serve as a site for solute adsorption or nucleation,[110]

acting to assist solute incorporation. The above observations in solute nanoparticles suggest that a higher grafting density in graft copolymer is desirable for promoting their solute stabilization capability as well as improving the quality of solute nanoparticles.

Table 3.3. Loading capacity (*LC%*) and loading efficiency (*LE%)* of RBL stabilized by copolymer B1, B2, and G1.

Copolymer	*LC%*	*LE%*
B1	14.1	80.2
B2	15.0	80.5
G1	9.35	51.52

2.4 Conclusion

In this chapter, a variety of amphiphilic copolymers possessing different molecular architectures, including molecular brush, graft, and toothbrush-like structures, were successfully synthesized. Self-assembly of these copolymers was triggered by a rapid change in solvent quality, resulting in spherical nanoparticles in all cases. Nanoparticle size and quality were shown to be influenced by the topological properties of the branched copolymers: a higher side chain grafting density promotes the formation of smaller particles, with possibly lower aggregation numbers. Also, a higher local density of PEG brushes facilitates the formation of more uniform nanoparticles. Micelles from copolymers with a higher grafting density appear to have a better thermodynamic stability, implicated by the lower measured C_{CMC}. An NMR study of the nanoparticles in D_2O demonstrates that a core-shell structure was formed in all samples. However, lower PEG exposure ratio was observed in nanoparticles

from the highly grafted **B1**. PEG burial inside nanoparticles could be related with the high miscibility between closely attached PLA and PEG blocks in **B1**. The assembly kinetics of molecular brush and toothbrush-like copolymer was examined, by varying mixing conditions (i.e., mixing velocity expressed in terms of Re). For both copolymers, in low Re region, nanoparticles sizes were found to be dependent on mixing velocity (Re). In the high Re region, where mixing velocity becomes shorter than the polymer aggregation time, particle sizes are independent of mixing velocity (Re). The breakpoint, which reflects polymer aggregation time, is dependent on polymer architecture and concentration. These observations indicate that the molecular brush **B1** has a longer aggregation time compared with the less grafted toothbrush-like **T2**. However, more details on assembly kinetics of copolymers, e.g. absolute assembly time remains unknown and will be determined in future work. Finally, copolymers were examined as solute stabilizers, by using RBL as a model drug. Solute particles, protected by amphiphilic branched copolymers, were successfully prepared by the rapid assembly method. Molecular brushes with dense grafting have demonstrated advantages, achieving higher *LC%* and *LE%* of RBL, as well as better defined solute nanoparticles.

Chapter IV. Macromolecular Brushes as Stabilizers of Hydrophobic Solute Nanoparticles

4.1 Introduction

The study of materials and techniques that enable the formation of efficient carriers of hydrophobic drug compounds is a topic of continuous interest from scientific and technological perspectives. The limited water solubility of approximately 70% of promising new drug candidates restricts their development because of expected poor bioavailability.[2] Alternatives include conversion to higher solubility salts provided the drug is ionizable, through the use of cosolvents or solubilizing agents, by producing higher-solubility polymorphs of the drug, or by decreasing particle size.[111-114] In the form of nanoparticles, with high surface area to volume ratios, the bioavailability of poorly water-soluble drugs should exhibit significant improvement.

Nanoparticle fabrication is broadly divided in two techniques: micronization (attrition) and precipitation. In precipitation by solvent shifting, particle formation occurs by a decrease in the solvent quality of the fluid phase with respect to the solute, increasing its supersaturation, through addition to/of a miscible nonsolvent. The resulting particle size, size distribution, and morphology will be determined by the kinetics of nucleation and growth of the solute, the rate and magnitude of supersaturation, mixing intensity, and occurrence of secondary processes such as Ostwald ripening, secondary crystallization, and aggregation.[115-118] In addition to the solute and the mutually miscible solvent/ nonsolvent pair, additives such as stabilizers

or emulsifiers and hydrophobic polymers are also present during the solvent-shifting process, and the exact mechanism by which they influence particle formation is complex.[115] The presence of a hydrophobic polymer, while nonessential for producing stable nanoparticles, serves to entrap the drug by concomitant precipitation and can control release rate. The emulsifier effects steric or electrostatic stabilization by reducing collisions or ensuring repulsive interactions between particles that would otherwise lead to agglomeration[119] and to suppress solvent-mediated interparticle solute migration resulting in Ostwald ripening. The function of each additive, however, is complicated by the fact that they can also act as nuclei for particle growth and influence crystallization.[115] Examples exist where encapsulation and emulsification are simultaneously achieved by the use of block copolymers,[120,121] designed to entrap the drug through interactions with its hydrophobic block, and facilitate nanoparticle dispersion via its hydrophilic block.[122-124] In this sense, the properties of a nanoparticle will depend strongly on the physicochemical characteristics of all the components comprising the system.

Flash nanoprecipitation (FNP), an example of arrested precipitation, occurs under conditions wherein the kinetics of solute nucleation and growth and those of emulsifier adsorption onto growing nuclei or self-assembly are balanced to produce particles in the nanometer range.[37] Nanoparticle size and particle size distribution will depend on matching these characteristic times. A key factor in flash nanoprecipitation is mixing intensity.[37,104,116,125] Its relevance relies on enhancing mass transfer to achieve high supersaturation rates with uniform spatial distribution, resulting in smaller particles with narrow polydispersity. Achieving homogeneous precipitation

conditions, especially at high supersaturations, is challenging and most effectively accomplished with high-energy micromixing (mixing on a molecular scale) methods.[126]

Polymer-based stabilizers are particularly useful given their chemical, compositional and architectural versatility, and enhanced stability compared to their small-molecule analogues.[35] Monomer type, copolymer composition, molecular weight, and chain architecture are engineered to control polymer degradation rate and therefore achieve desired drug release profiles, protect against enzymatic degradation or hydrolysis during transport, reduce systemic toxicity, and enable active delivery.[127-129] A number of combinations of hydrophobic solutes (drugs and imaging agents) and polymer stabilizers have been evaluated in the context of nanoprecipitation to establish general guidelines regarding the physicochemical parameters that will ultimately lead to stable nanoparticles.[19,41,104,130,131] These include high solute hydrophobicity and hydrophobic block chemistry; the latter will determine the glass transition temperature and the ability of the polymer to crystallize. The majority of stabilizers examined consist of systems based on poly(ethylene glycol) as the hydrophilic component, and a diversity of hydrophobic polymers including poly(D,L-lactide), poly(D,L-lactide-*co*-glycolide), poly(ε-caprolactone), and poly(propylene oxide).

In contrast to the widespread use of diblock copolymers bearing an amphiphilic character, considerably less is known regarding the use of polymers with a branched architecture as stabilizers, despite their ability to form stable micelles (or vesicles) in a selective solvent.[52,103,132-134] An interesting example is the use of branched vs. linear

poly(ethylene imine)s in which case more effective steric stabilization of β-carotene was achieved with the higher molecular weight branched polymer.[135] Among the many examples of branched polymers, we are interested in asymmetric macromolecular brushes, which consist of a linear backbone densely grafted with two different side-chains on each repeat unit.[52,132] As we have previously shown, asymmetric macromolecular brushes are known to self-assemble into a variety of morphologies in selective solvents including spheres, worms, or toroids, and bilayer structures, according to side-chain lengths and hydrophilic fraction.[136] Unlike linear copolymers, the self-assembly of grafted polymers bearing an amphiphilic character involves a balance between intra- and intermolecular association, strongly dependent on polymer chemistry and assembly conditions. Given their unique molecular structure and characteristic associations, we were interested in evaluating the ability of brush copolymers to stabilize hydrophobic molecules and examining the effect, if any, their molecular structure would have on the properties of the nanoparticles stabilized by them in contrast to more commonly used linear diblock copolymers.

Herein we examine the use of an asymmetric macromolecular brush based on poly(ethylene glycol) and poly(D,L- lactide) as the stabilizer of hydrophobic solutes and compare nanoparticle properties to those formed by a linear diblock copolymers with the same block chemistry. While some of the solutes and PEG/PLA-based copolymers used in this study have been previously examined in the context of nanoparticle formation by flash nanoprecipitation, as we explain, the molecular structure of the polymer has important consequences on nanoparticle properties, specifically related to nanoparticle propensity to undergo solvent-mediated effects

such as Ostwald ripening.

4.2 Materials and Methods

4.2.1 Materials and Characterization

All reagents were commercially available and used as received unless otherwise noted. The styrene oligomer (SO) used was purchased from Shodex (SL-105, S-0.7; M_n = 740 g/mol, M_w = 820 g/mol). Glycidyl methacrylate (GMA, Aldrich 97%) was passed through a short basic alumina column to remove the inhibitor. 2,2′-Azobis(isobutyronitrile) (AIBN) and D,L-lactide were recrystallized from methanol and anhydrous ethyl acetate, respectively. 1,8-Diazabicyclo[5.4.0]- undec-7-ene (DBU) was kept over molecular sieves (3 Å) overnight. Deionized water was purified in a Barnstead Nanopure system to a final resistance of 18.2 mΩ.

Gel permeation chromatography (GPC) was performed on a Waters 1515 Isocratic HPLC equipped with two Styragel columns (HR4 and HR3, 300 mm × 7.8 mm) connected in series, a differential refractive index detector (Waters 2414) and a UV-visible detector (Waters 2489). HPLC grade tetrahydrofuran was used as the eluent, at a flow rate of 1 mL/min. Molecular weights are reported referenced to polystyrene standards (Shodex SL-105). ^{1}H NMR spectra were recorded on a Bruker AV 400 MHz spectrometer in either $CDCl_3$ or DMSO-d_6. Spectra were referenced to $CHCl_3$ (7.26 ppm) or DMSO (2.50 ppm). Dynamic light scattering (DLS) experiments were conducted on a Malvern Instruments Nano- ZS ZetaSizer equipped with a 4 mW He−Ne laser operating at 633 nm. All measurements were performed at 25 °C at a

scattering angle of 173°. Static light scattering (SLS) was performed with DAWN HELEOS II (Wyatt Technology) with 120 mW GaAs linearly polarized laser operated at 658 nm. Fluorescence spectroscopy was carried out on a Fluorolog-3 system (HORIBA Jobin Yvon Inc., NJ). Bright-field transmission electron microscopy (TEM) imaging was performed on a FEI Tecnai 12 TWIN transmission electron microscope operated at an acceleration voltage of 100 kV. TEM images were recorded by a SIS Megaview III wide-angle CCD camera. TEM grids (carbon-coated copper grids from Electron Microscopy, Hatfield, PA) were ionized under plasma before preparation. Grids were placed on a drop of sample suspension (20 μL) for 5 min, washed with 5 drops of doubly distilled water, and placed onto a drop of 2 wt % aqueous uranyl acetate solution for 30 s. Excess solution was blotted with filter paper, and samples were allowed to dry at room temperature prior to imaging.

4.2.2 Synthesis of Macromolecular Brushes

Synthesis of the $PGMA_{273}$ backbone

Glycidyl methacrylate (3 mL, 0.022 mol), 2-cyano-2-propyl benzodithioate (CPB, 6.26 μL, 0.032 mmol,) and azobisisobutyronitrile (AIBN, 0.7452 mg, 0.0064 mmol) were added to a clean and dry round bottom flask equipped with a magnetic stir bar and a septum. Reagents were dissolved in 3 mL of benzene, and the mixture was bubbled with argon for 1 h. The reaction was conducted at 60 °C for 16 h. Polymerization was stopped by immersing the flask in an ice bath and opening it to atmosphere. Aliquots were taken to evaluate monomer conversion. Samples were diluted with dichloromethane and precipitated in methanol. The resulting precipitate

was dried under vacuum. Yield: 28.8%. Monomer conversion was 39%, determined by ^{1}H NMR and the degree of polymerization (DP) of PGMA was estimated based on conversion. ^{1}H NMR of resulting polymer is shown in Figure 4.1 and the corresponding chromatogram of the polymer is included in Figure 4.7.

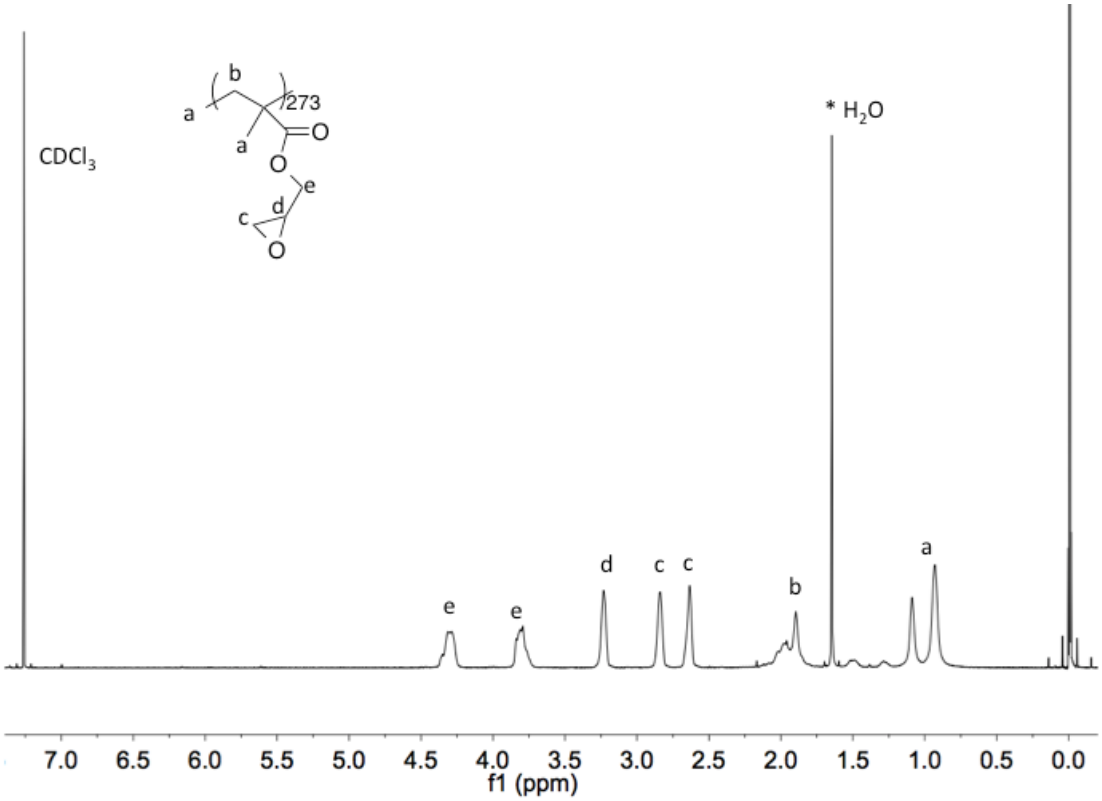

Figure 4.1.^{1}H NMR and peak assignments of the PGMA$_{273}$ backbone.

Azidolysis of PGMA$_{273}$ (PGMA$_{273}$-N$_3$)

PGMA (801.7 mg, 5.64 mmol epoxy groups) was added to a round bottom flask and dissolved in 20 mL of N,N-dimethylformamide (DMF). Sodium azide (1.098g, 16.89 mmol) and ammonium chloride (905.9 mg, 16.94 mmol) were added once the polymer was completely dissolved. Azidolysis was conducted at 50 °C under argon for 24 h. The resulting solution was cooled to room temperature and diluted with

tetrahydrofuran. Salts were filtered off and the solution was concentrated before precipitation into Nanopure water. Solids were lyophilized. Yield: 39.0%. ^{1}H NMR peaks assignments are shown in Figure 4.2. Signals indicate quantitative conversion.

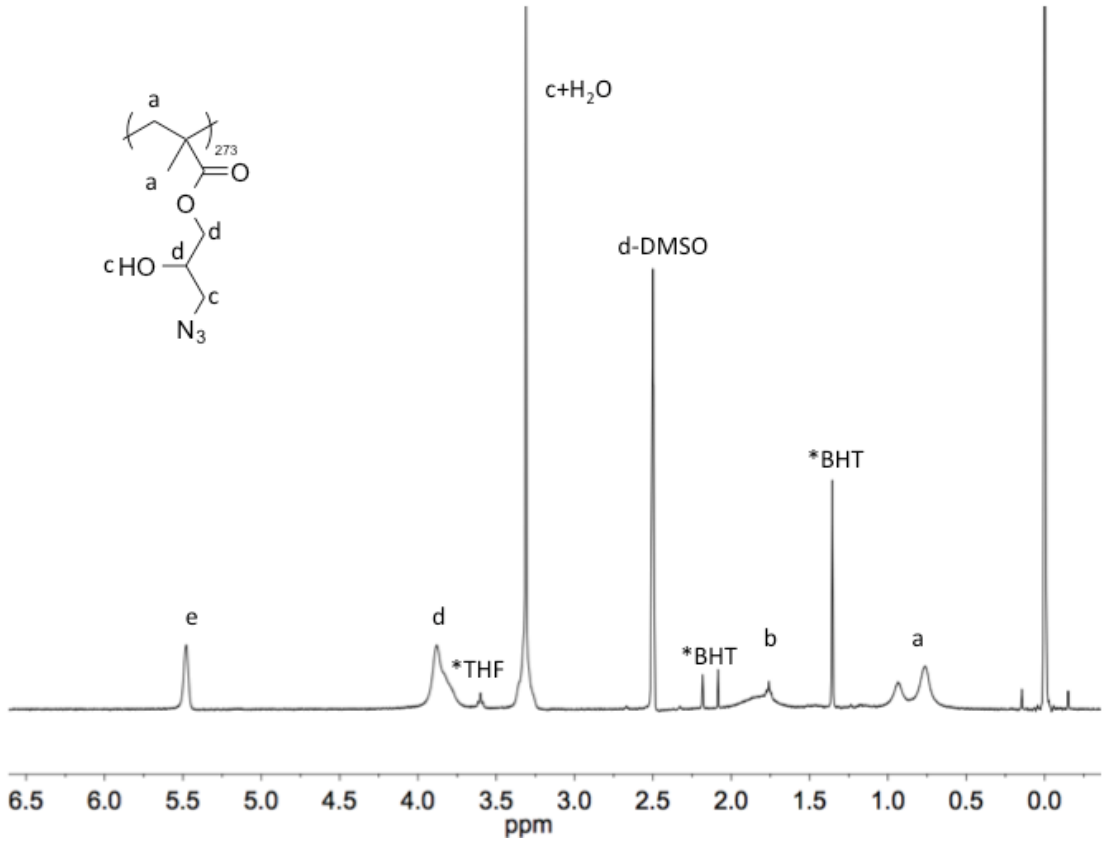

Figure 4.2. ^{1}H NMR and peak assignments of $PGMA_{273}$-N_3.

Synthesis of $PGMA_{273}$-g-PLA_{17}

$PGMA_{273}$-N_3 (200 mg, 1.08 mmol –OH group) and D,L-lactide (2.162 g, 15 mmol) were loaded into a round bottom flask, and placed under high vacuum at 36 °C for ~5 hours. After backfilling with argon, ~10mL of anhydrous DMF was added to dissolve the reagents. 1,8-Diazabicyclo[5.4.0]undec-7-ene (DBU, 83.2 µL, 0.56 mmol) was then injected and the reaction was allowed to proceed for 1.5 h under argon at room

temperature. Polymerization was quenched by addition of benzoic acid (170 mg, 1.39 mmol). DMF was removed under vacuum and the polymer was re-dissolved in THF, followed by precipitation into a mixture of Nanopure water and methanol (1:1, vol). Solids were lyophilized to remove water. Yield: 86.8%. ^{1}H NMR of the resulting grafted polymer is shown in Figure 4.3. The chromatogram of this polymer is included in Figure 4.7. The degree of polymerization of PLA side chains was calculated based on signals e and e'.

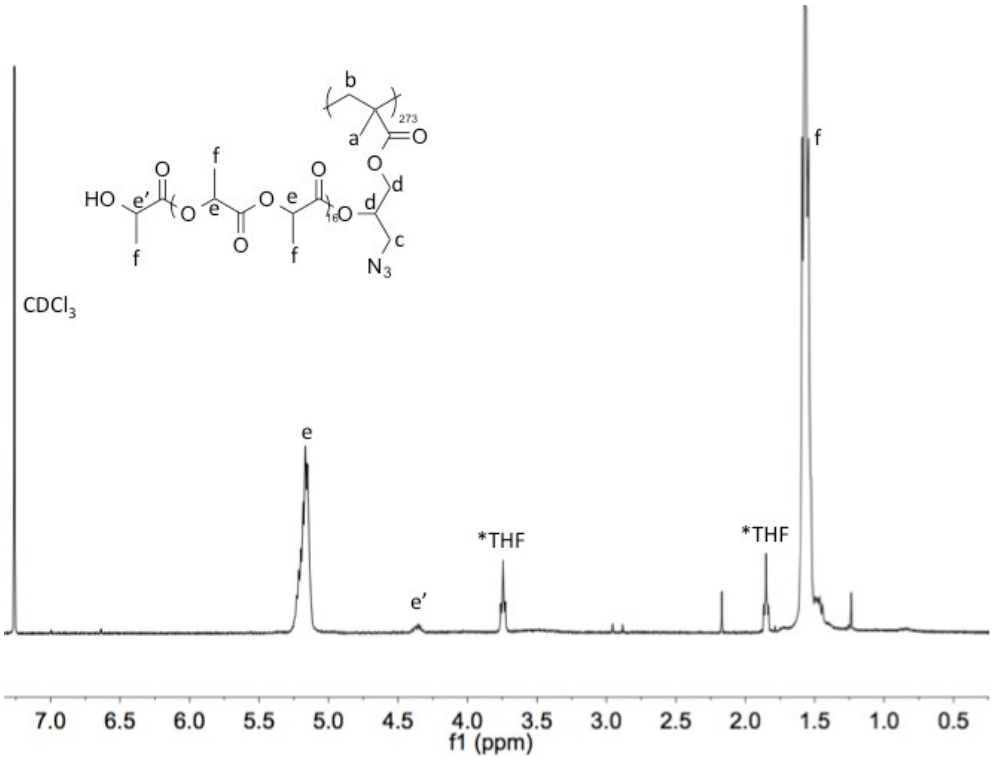

Figure 4.3. ^{1}H NMR and peak assignments of $PGMA_{273}$-*g*-PLA_{17}.

Synthesis of $PGMA_{273}$-g-PEG_{17}/PLA_{17}

Alkynl-PEG was grafted onto $PGMA_{273}$-g-PLA_{17} using 'click' chemistry, catalyzed by $CuSO_4 \cdot 5H_2O$/ascorbic acid. The molar ratio of $-N_3$, alkynyl groups, $CuSO_4 \cdot 5H_2O$ and ascorbic acid used was 1:1.1:0.2:1. $PGMA_{273}$-g-PLA_{17} (500 mg, 0.19 mmol) and

alkynyl-PEG (182.6 mg, 0.21 mmol) were dissolved in DMF inside a round bottomed flask. Ascorbic acid (34.4 mg, 0.19 mmol) was then added and the solution was bubbled with argon for 30 min. $CuSO_4 \cdot 5H_2O$ (9.8 mg, 0.04mmol) was then added under argon and reacted for 12 h under an inert atmosphere. The resulting polymer was purified by dialysis against Nanopure water for 7 days and lyophilized. Yield: 85.4%. The ^{1}H NMR spectrum of the final product is provided in Figure 4.4. PEG grafting was estimated at 96.7%. The chromatogram of this sample could not be acquired in our current setup because of a molecular weight limitation, so polydispersity was estimated by comparing M_n (from ^{1}H NMR) and M_w from static light scattering.

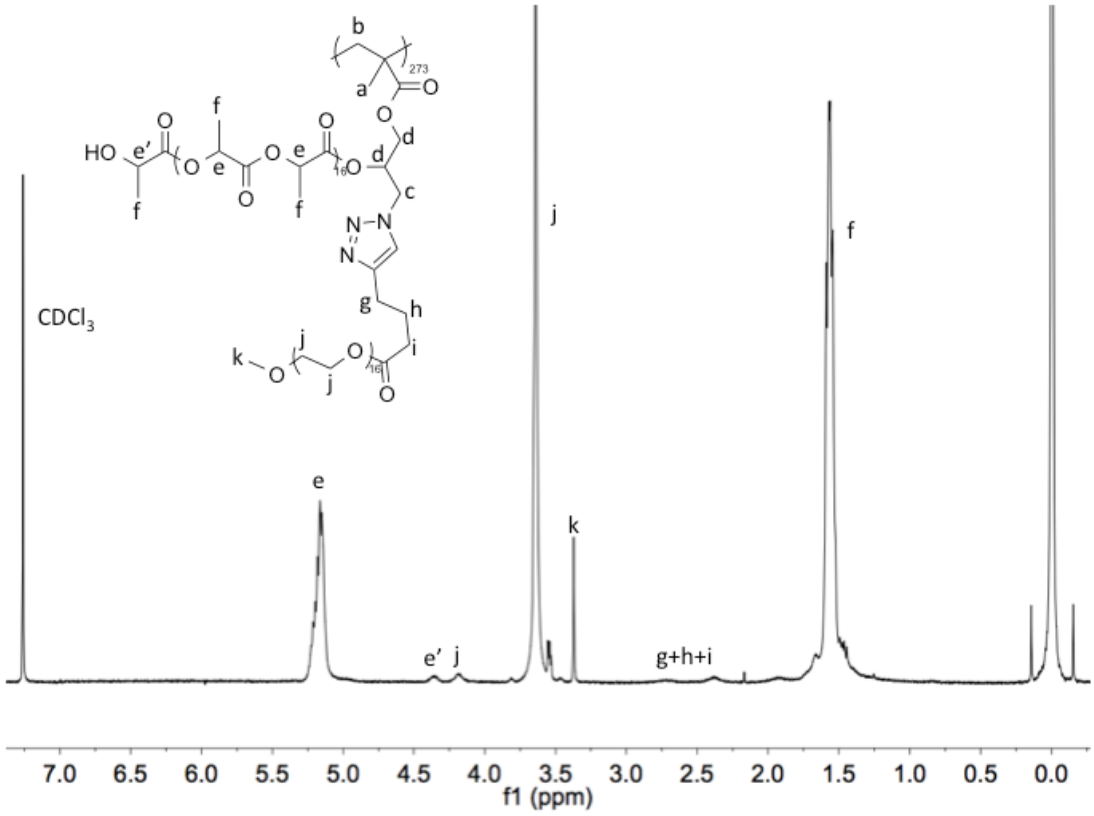

Figure 4.4. ^{1}H NMR and peak assignments of $PGMA_{273}$-*g*-PEG_{17}/PLA_{17}.

Synthesis of PEG_{16}-b-PLA_{16} and PEG_{45}-b-PLA_{85}

Monomethoxypoly(ethylene glycol) (mPEG) was loaded into a round bottom flask, and placed under high vacuum at 90 °C for ~1 h. After cooling and backfilling with argon, D,L-lactide was added to the flask and placed under high vacuum at 36 °C for ~3 h. After backfilling with argon, anhydrous dichloromethane was added to dissolve all reagents. DBU was then injected and the reaction was allowed to proceed for 1 h under argon at room temperature. Polymerization was quenched by addition of benzoic acid, followed by precipitation into 2-propanol. Resulting ^{1}H NMR spectra and chromatograms are given in Figures 4.5 and Figure 4.6. Exact quantities of each reagent, and yields, are provided in the table below. For PEG_{16}-b-PLA_{16}, ^{1}H NMR M_n = 4.3 kDa, GPC: M_w = 3.9 kDa, Đ = 1.16.

Table 4.1. Synthesis details of PEG_{16}-b-PLA_{16} and PEG_{45}-b-PLA_{85}

	PEG_{45}-*b*-PLA_{85}	PEG_{16}-*b*-PLA_{16}
mPEG, mg (mmol OH)	203.8 (0.10)	317 (0.42)
D,L-lactide, g (mmol)	1.223, 8.49	0.845, 5.86
DBU, µL (mmol)	12.7, 0.085	8.8, 0.059
dichloromethane, mL	8	8
benzoic acid, mg (mmol)	31, 0.253	24, 0.197
yield (%)	83.5	53.5

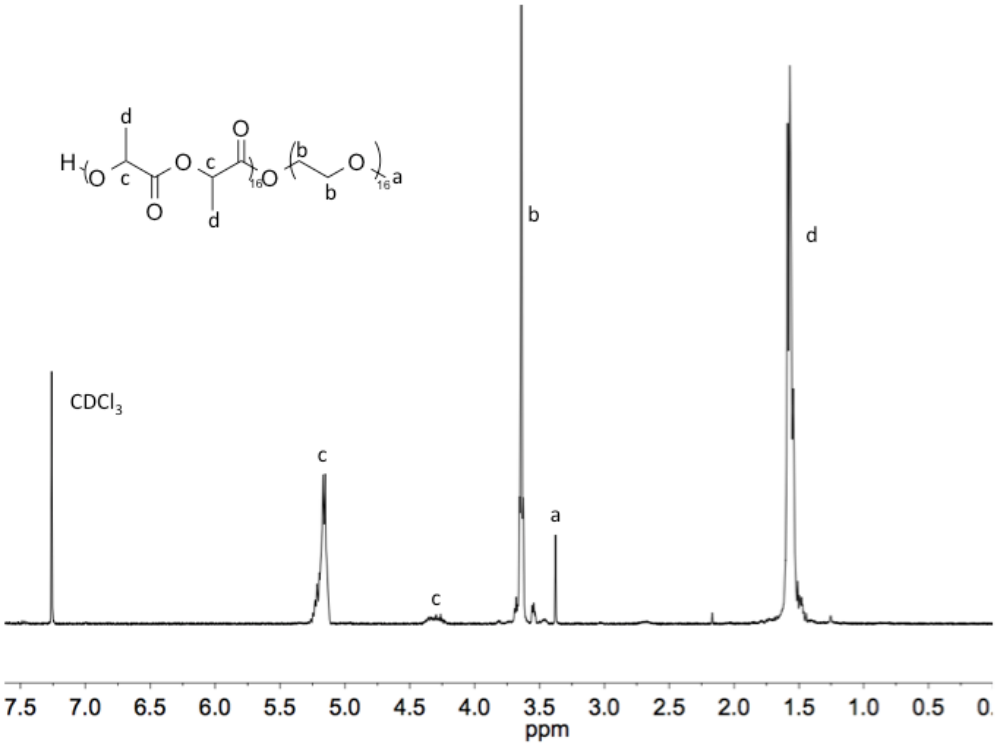

Figure 4.5. ^{1}H NMR and peak assignments of PEG$_{45}$-*b*-PLA$_{85}$.

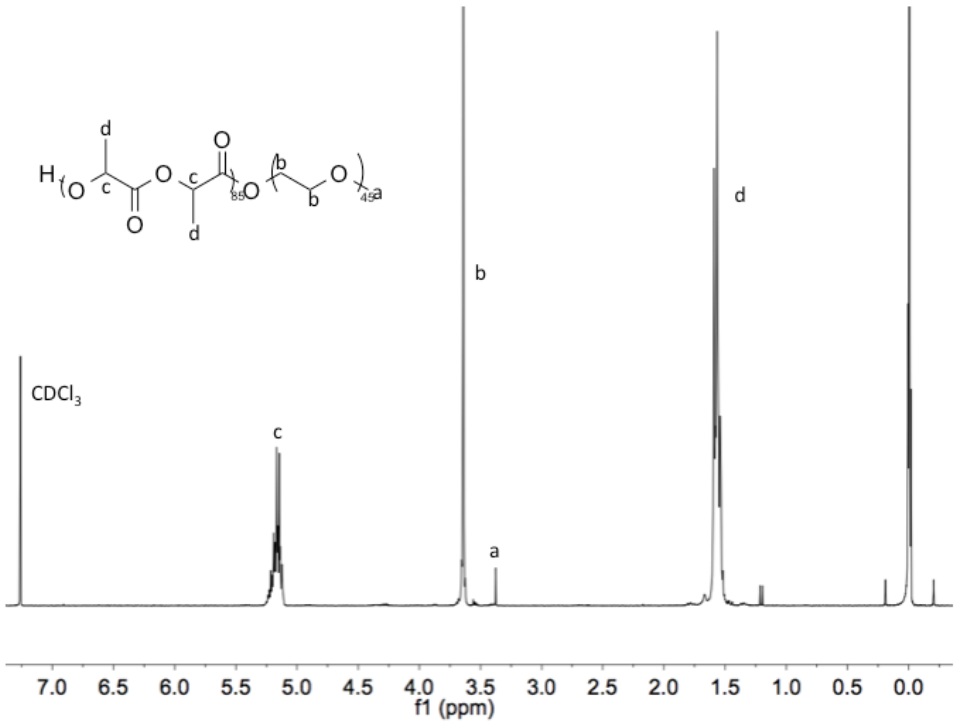

Figure 4.6. ^{1}H NMR and peak assignments of PEG$_{16}$-*b*-PLA$_{16}$.

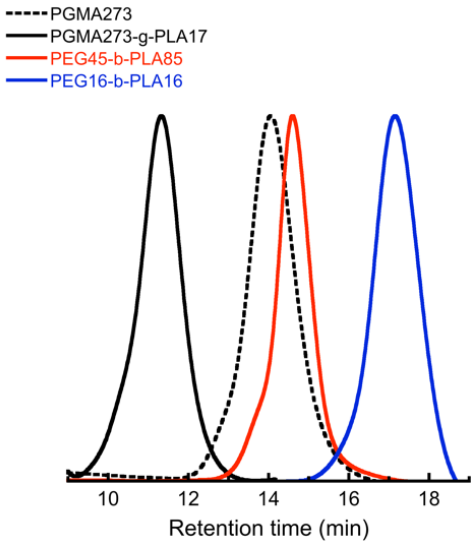

Figure 4.7. Gel permeation chromatograms of linear and branched copolymers.

4.2.3. Protocol for the synthesis of gold nanoparticles (C-18 Au NPs)

$HAuCl_4 \cdot 3H_2O$ (100 mg) was loaded into a three necked flask. Oleylamine (1 mL) and 1-octadecene (10 mL) were injected into the flask. The resulting yellow/orange mixture was vigorously stirred and heated to 75 °C under a continuous stream of nitrogen for 2 h. After this time, the solution was cooled to room temperature and transferred to centrifuge tubes (with hexane). The solution was then diluted 8 times with ethanol and particles were collected by centrifugation at 10,000 rpm for 10 min. The resulting precipitate was suspended in hexane and washed twice following the same protocol. The concentration of Au NPs in solution was determined by gravimetry. A representative TEM image of the synthesized Au NPs is provided in Figure 4.8.

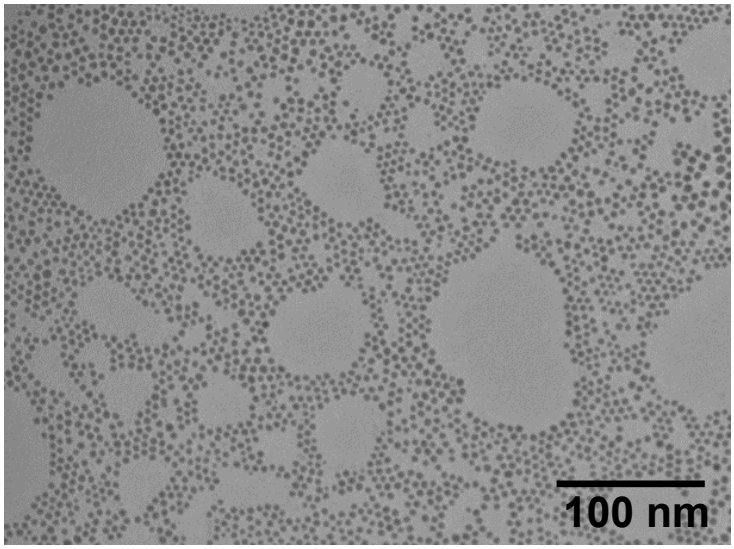

Figure 4.8. Representative TEM image of synthesized gold nanoparticles (Au NPs).

4.2.4 Differential Refraction Index Measurement

Measurements were performed on an Optilab-rEX refractive index detector (Wyatt Technology) at a wavelength of 658 nm. The flow cell temperature was set at 25 °C. Polymer solutions in anhydrous dimethylformamide (DMF), with concentrations ranging from 0.2 to 2 mg/mL, were filtered through 0.45 μm PVDF syringe filters (Thermo Scientific) prior to measure- ments. Solutions were injected with a syringe pump (New Era Pump System, NE-1000) at 0.2 mL/min. dn/dc values were analyzed using an Astra 6.1 software.

4.2.5 Static Light Scattering

Static light scattering measurements were conducted on the filtered solutions of the polymer in DMF described above. Pump velocity and flow cell temperature were kept at 0.2 mL/min and 25 °C, respectively. Measurements were normalized with

polystyrene (20 kDa, Fluka; 5 mg/ mL solution in dimethylformamide). dn/dc values were used to determine polymer absolute molecular weight. M_w was extracted from Zimm plots using the Astra 6.1 software and the Debye model.

4.2.6 Critical Micelles Concentration

C_{CMC} of polymers were measured by using pyrene as a probe. For this, 50 μL of a pyrene solution in acetone (6×10^{-5} M) was loaded into a 5 mL scintillation vial and left open under the hood to allow for complete evaporation of the solvent. Fifty microliters of polymer solution (0.001 to 2 mg/mL in acetone) was then added to each of 10 vials containing pyrene, followed by 1 mL of water. Final amphiphile concentration ranged from 50 μg/ mL to 0.1 mg/mL. Samples were vigorously stirred with a vortex mixer (~1 min) and left to shake gently overnight to evaporate acetone. Excitation and emission spectra were recorded by fluorescence spectroscopy. Pyrene excitation was scanned from 300 to 360 nm at an emission wavelength of 390 nm. Excitation and emission bandwidths were set at 2 nm. The intensity ratio from the signals at 336 and 334 nm (I_{336}/I_{334}) was analyzed as a function of polymer concentration. C_{CMC} values were read from the intersection between curve tangents at low and high concentrations.

4.2.7 X-ray Scattering

X-ray scattering of *β*-carotene powder and lyophilized nanoparticle samples was carried out on a Phillips X'Pert X-ray diffractometer with CuKα radiation (λ = 1.5406 Å) at 45 kV and 40 mA.

4.2.8 Polymer Self-Assembly

Polymers were dissolved in tetrahydrofuran (THF) at 2.5 mg/mL. Self-assembly was carried out in a four-inlet vortex mixer, the details of which are provided elsewhere.[28] Nanopure water was charged into three 50 mL syringes (Hamilton, NJ) and the organic solution into a 10 mL syringe, and mounted on two separate syringe drivers (PHD Ultra, Harvard Apparatus). Three solvent (tetrahydrofuran, THF) concentrations were examined: 25%, 10%, and 5% (v/v). Flow rates of water and organic streams were as follows: i) for 25% THF, 30 mL/min (water) and 30 mL/min (THF); ii) for 10% THF, 36 mL/min (water) and 12 mL/min (THF); iii) for 5% THF, 36 mL/min (water) and 9 mL/min (THF). Samples were collected and dialyzed (6−8 kDa MWCO, Fisherbrand) against Nanopure water for 24 h at 20 °C. Water was replenished every 4 h throughout the dialysis process. Samples were stored in clean scintillation vials and, unless otherwise noted, kept under refrigeration at 4 °C.

4.2.9 Flash Nanoprecipitation

The protocol described above was used to prepare solute loaded nanoparticles, with the exception that both the polymer and the solute (*β*-carotene, styrene oligomer or Au NPs) were dissolved together in tetrahydrofur- an. Polymer concentration was kept at 2.5 mg/mL, while solute concentration varied between 5% and 100% w/w_p. Dialyzed samples were collected and filtered through 0.45 μm PVDF syringe filters (Thermo Scientific) and stored in clean centrifuge tubes (Falcon Tube). Loading capacity (LC) and efficiency (LE) in nanoparticles (NP) are estimated as

$$Loading\ capacity\ (LC,\%) = \frac{Mass\ of\ solute\ in\ NP}{Mass\ of\ NP} \times 100$$

$$Loading\ efficiency\ (LE,\%) = \frac{Mass\ of\ solute\ in\ NP}{Mass\ of\ solute\ in\ feed} \times 100$$

LC and LE of *β*-carotene were determined with a Varian Cary 50 UV/vis spectrophotometer (Agilent Technologies, Santa Clara, CA). Loaded micelles were lyophilized and the resulting powders were resuspended in chloroform. The concentration of *β*-carotene was calculated with a calibration curve of *β*-carotene in chloroform, based on its absorbance at 456 nm. LC and LE of styrene oligomer (SO) solute was calculated by ^{1}H NMR. SO-loaded particles were lyophilized and dissolved in $CDCl_3$, and the ratio of SO was calculated by comparing proton numbers of SO and of the stabilizing polymer.

4.3 Results and Discussion

4.3.1 Amphiphiles and Solutes

Structures and characteristics of the poly(ethylene glycol)/ poly(D,L-lactide) (PEG/PLA) copolymers and hydrophobic solutes examined are given in Figure 4.9 and Table 4.2.

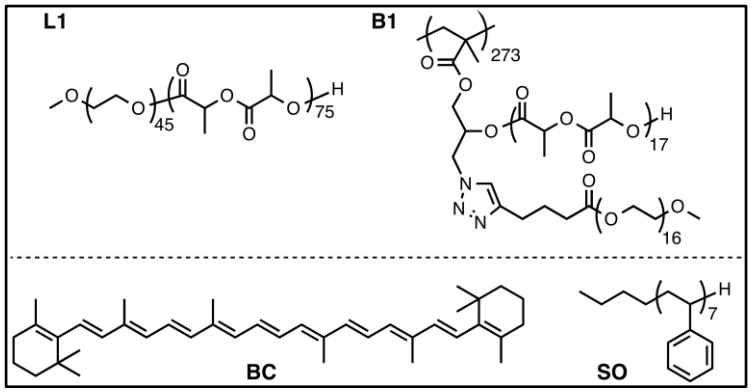

Figure 4.9. Structures of linear (L1) and brush (B1) copolymers, and hydrophobic solutes *β*-carotene (BC) and styrene oligomer (SO).

Table 4.2. Characteristics of PEG/PLA copolymers used in this study.

	polymer	w_{PEG}[a] (% wt)	M_n[a] (kg/mol)	M_w[b,c] (kg/mol)	$Đ_M$[b]	R_g[c] (nm)	C_{cmc}[d] (10^{-3} mg/mL)
L1	PEG_{45}-*b*-PLA_{85}	14.0	14.2	22.7 [b]	1.16	-	0.94
B1	$PGMA_{273}$-*g*-(PEG_{16}/PLA_{17})	22.0	930.9	1356.0 [c]	1.46 [d]	22.4	0.83

[a] Determined from ^{1}H NMR spectra. [b] Measured by gel permeation chromatography. [c] Determined by static light scattering in dimethylformamide. [d] Estimated as M_w(SLS)/M_n(^{1}H NMR). [e] Determined by fluorescence spectroscopy using pyrene as hydrophobic probe.

Nanoparticle properties of hydrophobic solutes stabilized by the brush copolymer (B1) were compared with those generated by using PEG-b-PLA copolymers (L1 and L2). L1 has larger hydrophilic and hydrophobic blocks than B1, as well as a lower PEG weight fraction; however, copolymers with compositions and block lengths similar to L1 were found throughout the literature to form stable nanoparticles.[6,137] L2 has the same hydrophilic and hydrophobic block lengths as B1, allowing for a direct comparison of the effect of polymer architecture on nanoparticle properties; however, nanoparticles formed by this polymer (with or without solute) underwent considerable aggregation. For this reason, we will largely focus our discussion comparing nanoparticles formed by B1 and L1.

4.3.2 Self-assembly of Amphiphiles

Unless otherwise specified, solute nanoprecipitation and polymer self-assembly were carried out inside a multi-inlet vortex mixer (MIVM), triggered by mixing an organic solution containing the polymer (and solute, when applicable) with water, a nonsolvent for PLA. Modeling studies of this system have shown that homogeneous mixing is effectively achieved at a Reynolds number of ~2000, defined as $Re = \square_{I,N} V_i L / v_i$, where N is the number of streams (in this case, 4), V_i and v_i are the velocity and kinematic viscosity of stream i, and L is the chamber diameter.[28] All experiments were carried out at Re > 2000. Unless otherwise specified, nanoparticle suspensions were transferred from the water-organic mixture used for their preparation into water through dialysis for 24 h at room temperature. Prior to evaluating their ability to stabilize hydrophobic solutes, self-assembled structures of polymers L1 and B1 were examined by transmission electron microscopy (TEM). Average dimensions were either directly measured from micrographs (in the case of nonspherical nanoparticles) yielding number-average sizes or determined by dynamic light scattering (z-average). Representative images are provided in Figure 4.10.

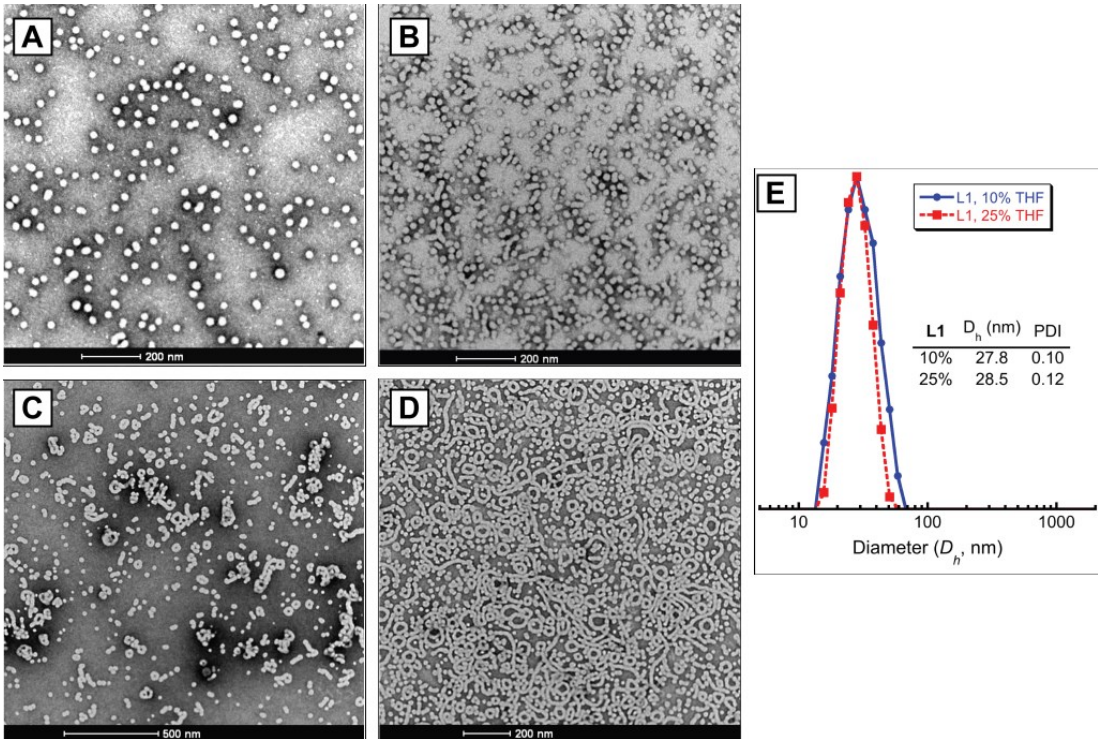

Figure 4.10. A-D: representative transmission electron micrographs of dialyzed self-assemblies from L1 (**A**, **B**) and B1 (**C**, **D**), prepared with final THF contents of 10% vol (**A**, **C**) or 25% (**B**, **D**). **E**: dynamic light scattering distributions of nanoparticles from L1, corresponding to images **A** and **B**.

As shown in Figure 4.10, regardless of final solvent content, L1 self-assembles exclusively into spheres, with an average diameter of 28 nm (by DLS, Figure 4.10 E). The brush copolymer, however, adopts a variety of coexisting morphologies, including spheres, worms, and toroids. At 10% THF, primarily spheres and small toroids are observed, whereas larger toroids and long worms exist at higher solvent content. The diversity of assembled structures from B1 results from a competition between intrachain collapse and interchain association, in which hydrophilic chains are preferentially located on the periphery of the aggregates, providing steric stabilization. Differences in solvent quality are expected to influence particle size by changing brush repulsion characteristics and core swelling.[29] Our initial study on this

system also revealed that the end-to-end connection of cylindrical aggregates into toroids results from the combined effects of shear forces and polymer concentration.[136] As we observed previously, average toroid minor diameter and sphere diameters are not very different from each other, in this case, 28 and 31 nm, respectively.

4.3.3 Effect of Solute Type and Concentration on Nanoparticle Properties

β-carotene (BC) is the most investigated of the carotenoids, a family of natural pigments exhibiting a conjugated bond structure. When ingested, BC is enzymatically converted into vitamin A; however, it has low oral bioavailability due to its poor water solubility.[138,139] Because of its hydrophobic character (octanol/water partition coefficient logP = 9.8, *www.molinspiration.com*), BC is an attractive solute to contrast the encapsulation ability of the branched B1 with respect to the linear diblock L1.[41,115,117,130,140] A representative image of *β*-carotene precipitated in the absence of a stabilizer, showing the ill-defined morphology of the resulting particles, is provided in Figure 4.11 as reference. To examine polymer stabilization, *β*-carotene nanoparticles with either 50% or 100% ($w/w_{polymer}$) feed were prepared with a final solvent content of 10% vol. Aggregate morphologies were recorded by TEM and are shown in 4.12 (for 50% BC feed).

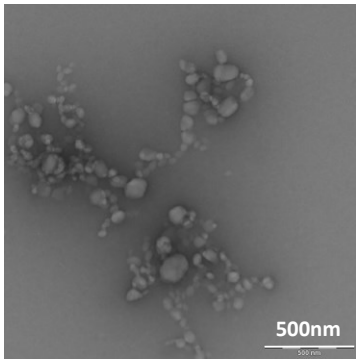

Figure 4.11. Representative TEM image of β- carotene precipitated without a stabilizer.Initial concentration was 1.25mg/mL in THF, solvent jump was 1:9 (THF: H_2O).

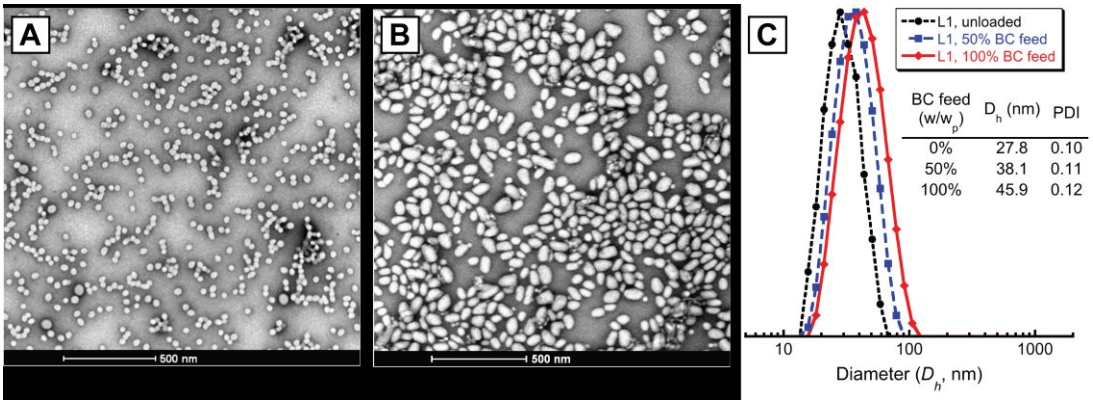

Figure 4.12. (A, B) TEM images of β-carotene nanoparticles (50% w/w_p in feed), stabilized by L1 (A) or B1 (B). C: size distributions of BC-L1 nanoparticles with different solute concentrations in the feed, as indicated.

Similar to nanoparticles of (unloaded) L1, β-carotene nanoparticles stabilized by L1 (or BC-L1), with either 50% or 100% solute feed, maintained a well-defined spherical shape. Average particle size increased with solute loading, as shown in Figure 4.12 and Table 4.3. This increase suggests that solute nucleation and growth occur faster than polymer self-assembly, allowing solute nanoparticles to grow larger prior to polymer adsorption. A similar observation was made for β-carotene stabilization by a poly(ethylene glycol)-b-poly(ε-caprolactone) copolymer.[104] Unlike BC-L1, BC-B1

nanoparticles exhibited a dramatic departure from the self-assembled morphologies of the (unloaded) polymer; rather, a mixture of spherical and predominantly ellipsoidal nanoparticles were formed. This is, to the best of our knowledge, the first occasion that nonspherical nanoparticles have been produced by flash nanoprecipitation. The development of techniques to fabricate nonspherical particles is a relevant topic in drug delivery since nanoparticle size, surface chemistry, and shape play important roles in determining their interaction with cells. As numerous experimental and simulation works have shown, there exist notable differences in biocirculation, biodistribution, and cellular uptake (kinetics and predominant mechanism) between spherical and nonspherical particles.[141-145] In this sense, it is important to understand the influence of the molecular characteristics of the stabilizing polymer on nanoparticle properties.

Table 4.3. Loading capacity and efficiency of β-carotene and polystyrene nanoparticles stabilized by L1 or B1.

	β-carotene feed [a]				PS feed [b]	
	50%		100%		100%	
	LC (%)	LE (%)	LC (%)	LE (%)	LC (%)	LE (%)
L1	35.1	92.7	49.0	84.5	-	-
B1	30.5	74.3	31.8	56.9	51.8	77.9

[a] Measured by fluorescence spectroscopy. [b] Estimated by gravimetric analysis.

To study the role of solute concentration on aggregate morphology, we examined BC-B1 nanoparticles by TEM over a range of solute feeds, from 5% to 100% w/w_p. As shown in Figure 4.13, there is a notable decrease in toroid population even at low solute feed (5%). Ellipsoid population increased with solute content until ~40%, after

which point no toroidal/ worm-like aggregates were observed. Ellipsoid size also increased with solute content with no large variation in aspect ratio: average major and minor diameters increased from 56 to 80 nm, and 38 to 58 nm, respectively. Aside from ellipsoids, spherical aggregates were also observed in this sample, as previously noted for the polymer. However, unlike ellipsoids, average sphere diameter did not change considerably with increasing solute concentration ($\Delta d \approx 2$ nm from 0% BC to 50% BC in the feed).

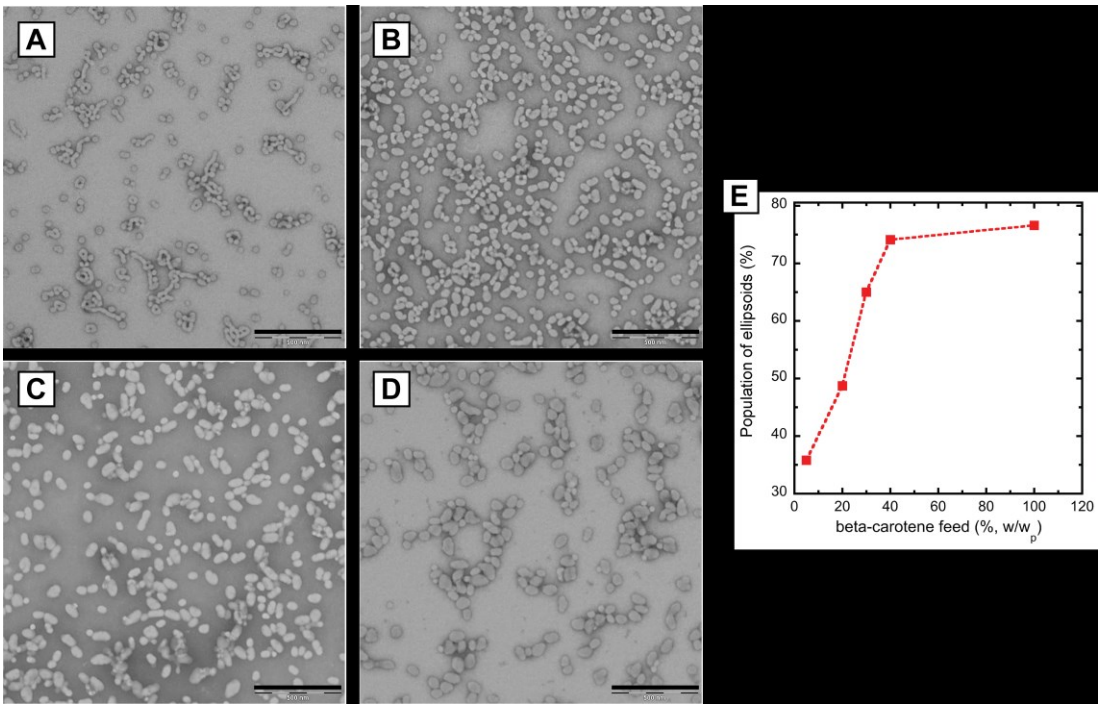

Figure 4.13 (A-D) TEM images of dialyzed *β*-carotene nanoparticles stabilized by B1. Solute feed increased from A through D as 5%, 20%, 40%, 100%. (E) ellipsoid population and average aspect ratio measured from TEM images. Scale bars correspond to 500 nm

A similar study was carried out for a styrene oligomer (SO, 7 repeat units) as the

solute. SO was chosen because it has a similar logP to β-carotene (log P = 10.6, *www.molinspiration.com*) and is amorphous. SO feed varied from 10% to 100% *w*/ w_p; aggregate morphologies are shown in Figure 4.14. In contrast to BC-B1, SO-B1 nanoparticles were spherical but also exhibited a broad particle size distribution. Similar to BC-B1, a decrease of toroid population with SO feed was observed; however, toroidal/worm-like aggregates were still present even at the highest SO concentration (100%), accounting for a very small fraction of the total number of particles. Average size also increased with solute feed as seen for BC-B1.

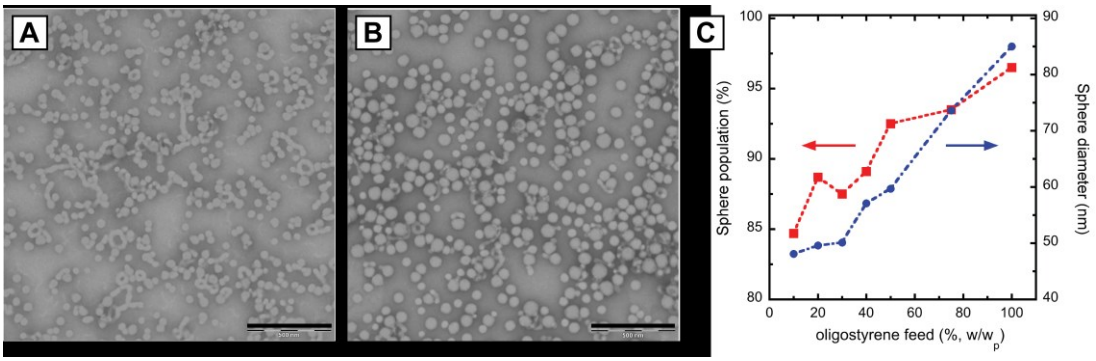

Figure 4.14. (A, B) TEM images of dialyzed polystyrene nanoparticles stabilized by B1. Solute feed corresponded to 40% (A) and 75% (B). (C) nanoparticle population and average sphere diameter measured from TEM images.

Drug induced morphological transitions of polymer assemblies, as is the case of nanoparticles stabilized by B1, have been observed in the past.[146-150] Loaded drugs can shift the balance from spherical to worm-like micelles,[147,148] and defects in the micellar shell can induce partial exposure of the hydrophobic core, initiating a sphere-to-rod transition. [151]Although solute induced rod-to-sphere transitions are less prevalent, they have been attributed to compaction of the micellar core by the solute, reducing the probability of hydrophobic chains from being exposed on the surface of

the micelles, therefore preventing the formation of worm-like structures.[146] Modeling studies also demonstrate that the introduction of solute particles into copolymer−solvent systems could impact the morphological phase behavior and the addition of solute shifts micelles to higher packing.[152] From a kinetic perspective, the presence of growing solute nuclei likely results in an alteration of the intra- and intermolecular associations that would otherwise lead to worm/toroids, minimizing the overall energy of the system by adsorption.

In flash nanoprecipitation, solute nuclei can form by homogeneous or heterogeneous mechanisms; the former generally occurs at higher solute concentrations than the latter.[37] Solute supersaturation is defined as the ratio of the total mass of solute fed, divided by the final solution volume (c), with respect to its bulk solubility at the final conditions (c_∞). At 50% and 100% feed concentrations of BC, supersaturation values are 1.5 and 3.1, respectively, both of which are low, pointing to heterogeneous nucleation as the most probable mechanism of nanoparticle formation. In this sense, the hydrophobic moieties of the stabilizing amphiphile may influence nanoparticle properties by lowering their activation energy for growth or by adsorbing onto solute nuclei. Furthermore, given the structure of B1 and its ability to undergo intramolecular association, it is possible that the high local concentration of hydrophobic chains could serve as a site to induce solute nucleation.

To further confirm the change in morphology induced by solute loading, we encapsulated C_{18}-stabilized gold nanoparticles (Figure 4.8) with B1. As shown in Figure 4.15, the toroidal/worm-like aggregates that remain, as well as a few small

spheres (indicated with arrows), do not contain gold nanoparticles, unlike the larger spherical aggregates. In contrast to other examples of polymer-stabilized gold nanoparticle clusters,[153,154] there appears to be a large distance separating individual gold colloids, indicative of a strong interaction between them and the polymer, resulting in high polymer content. This may be attributed to the branched structure of the copolymer and the high local concentration of hydrophobic chains on it that serve as a site for adsorption or nucleation.

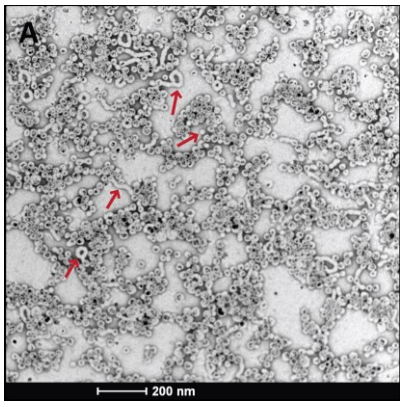

Figure 4.15. Representative micrograph of C-18 Au-NPs stabilized by B1. The sample was prepared at 25% THF with 50% w/w_p of gold nanoparticles. Arrows indicate original polymer morphologies (not incorporating the solute).

4.3.4 Effect of Preparation Method on Nanoparticle Properties

One of the advantages of the rapid mixing method used is that it establishes homogeneous precipitation conditions. We contrasted the morphology of particles produced by this method to one in which the stabilizing copolymer and solute (previously mixed) were added dropwise to a beaker containing water under rapid stirring. Polymer and solute concentration, as well as final solvent content, were

adjusted to achieve the same conditions as those used for rapid assembly in the MIVM with 50% BC. As shown in Figure 4.16, a few large ellipsoids were present; however, a large fraction of the polymer adopted the toroidal/worm-like morphology. This suggests that the ellipsoidal shape results from a specific interaction between the solute and the brush copolymer and provides evidence of a spatially nonuniform precipitation in a transport-limited system.

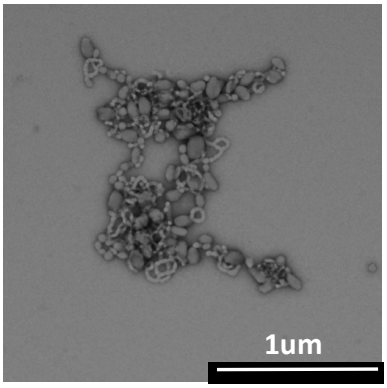

Figure 4.17. TEM of BC-B1 prepared by drop-wise addition of the organic phase into a stirred beaker containing water. Final conditions were 10% vol. THF, 50% w/w_p β-carotene.

4.3.5 Mechanism of Ellipsoidal Nanoparticle Formation

To understand the formation of β-carotene ellipsoids, we followed the morphological evolution of nanoparticles stabilized by L1 and B1 at different solvent contents and temperatures. Representative images of nanoparticles with 50% BC in the feed and 10% final solvent content are provided in Figure 4.18.

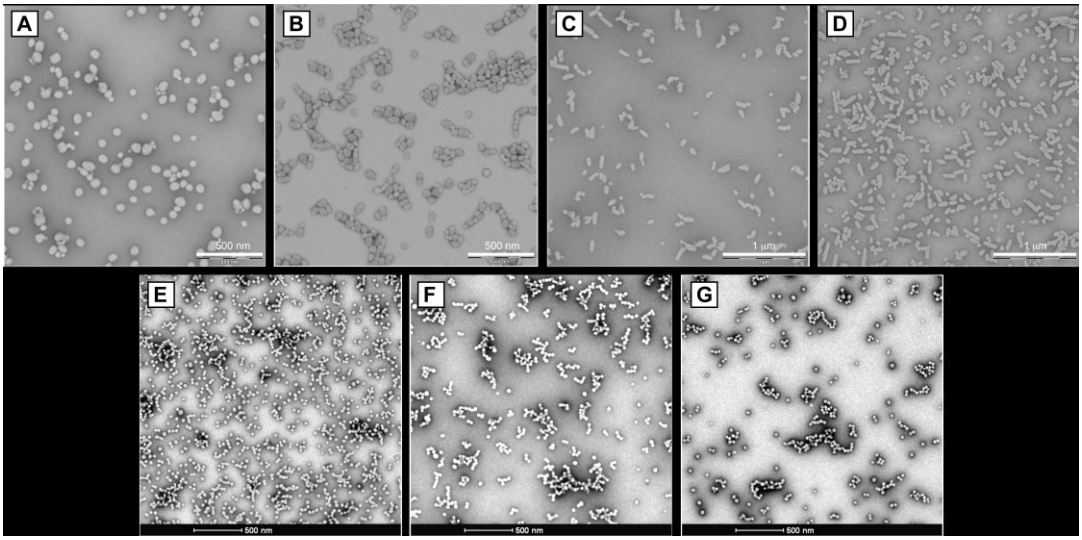

Figure 4.18. BC nanoparticles stabilized with B1 (top row) or L1 (bottom row) in 10% THF; solute content was 50% w/w_p in both cases. As-prepared samples (A, E) were either dialyzed at 20 °C for 24 h against water to remove the organic solvent (B) or incubated in the presence of solvent at 4 °C for 24 h (C,F) and 48 h (D,G)

Within 30 min of preparation (still in the presence of 10% THF), BC-B1 nanoparticles appear to be nearly spherical. Average major and minor diameters were 74 and 65 nm, respectively (Figure 4.19). After dialysis (24 h exchange at 20 °C), no significant changes were observed in the average major diameter, whereas the minor diameter decreased to 50 nm. When incubated at 4 °C in 10% THF (i.e., no dialysis), aggregates further developed a rod-like morphology, with lengths between 100 and 200 nm and widths of 60 nm (Figure 4.20). An increase in rod population was observed over time at this temperature. This unique rod-like shape is lost at higher temperature or higher solvent content (Figure 4.21), giving rise to spheres and long rods. In contrast, BC-L1 nanoparticles retained their original well-defined spherical shape throughout dialysis and after incubation at 4 °C for up to 48 h.

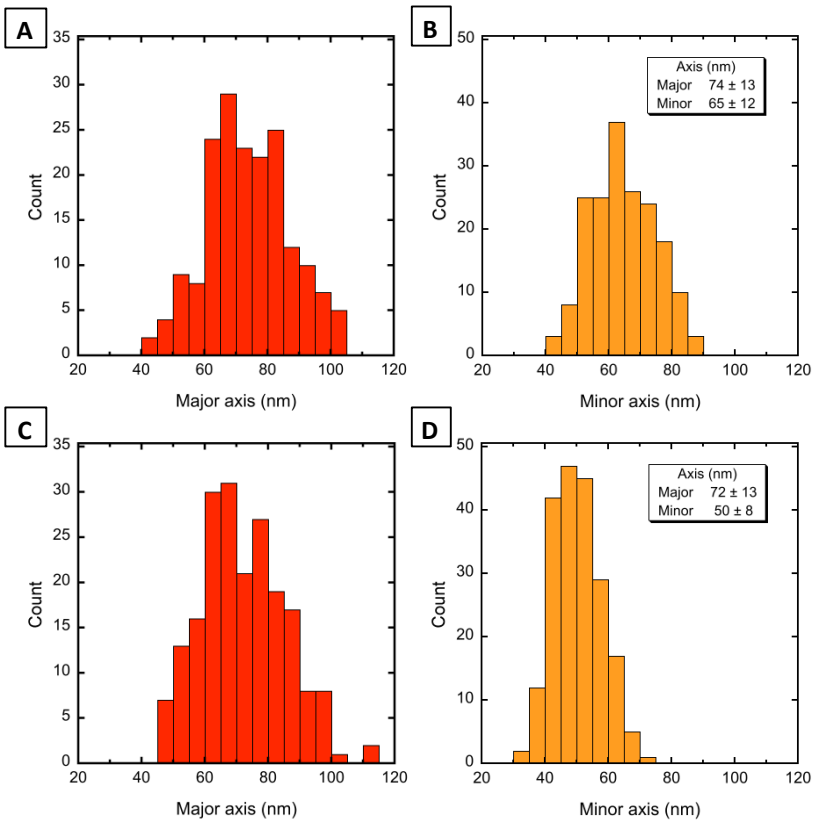

Figure 4.19. Ellipsoid dimensions of BC-B1 nanoparticles before (A,B) and after (C,D) dialysis. Nanoparticles were prepared using 10% THF with 50% w/w_p β-carotene. Dialysis was performed at 20 °C for 24 h.

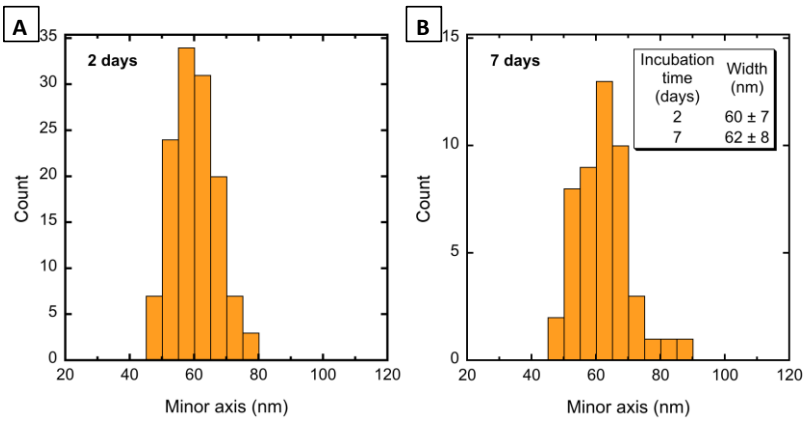

Figure 4.20. Width of short rods after incubation for 2 and 7 days at 4 °C, as indicated. Nanoparticles were prepared using 10% THF with 50% w/w_p β-carotene (feed).

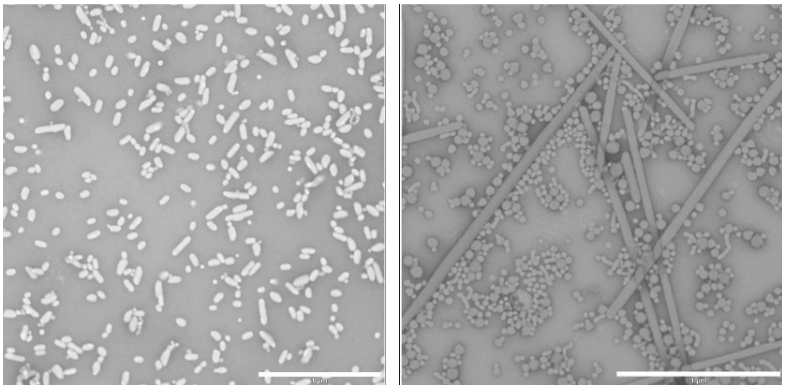

Figure 4.21. BC-B1 nanoparticles after incubation at 20 °C in 10% THF (A) or at 4 °C in 25% THF (B). Scale bars correspond to 1 µm.

Long-term stability of nanoparticle suspensions is influenced by solvent-mediated effects such as Ostwald ripening and secondary crystallization, and by the physicochemical properties of the stabilizing polymer.[37,130,131] Ostwald ripening, a process of dissolution and reprecipitation wherein larger particles grow at the expense of smaller ones shrinking, is driven by interfacial energy and strongly dependent on particle size distribution. It is caused by the increased solubility (c) of smaller particles, as described by[115]

$$c(r) = c^{\infty} exp(\frac{2v\gamma}{rRT}) \quad (4.1)$$

where r is the radius of a particle, c^{∞} is the bulk equilibrium solubility of the solute, γ is the solid-liquid interfacial tension of the solute, v is solute molar volume, R is the gas constant, and T the temperature.

In the absence of a stabilizer, the diffusion-controlled growth kinetics of particles with radius r is given by[140]

$$\frac{dr}{dt} \approx \frac{\gamma v^2 D c^{\infty}}{3RTr^2} \quad (4.2)$$

where D is the diffusion coefficient of a solute molecule in solution. Although the effect of the stabilizer is not accounted for in eq 4.2, amphiphilic block copolymers have been shown to lower the time scale for Ostwald ripening.[131] Furthermore, higher solvent content will lead to faster particle growth kinetics as the bulk equilibrium solubility of *β*-carotene increases exponentially with a linear increase in solvent composition.[140] Decreasing solubility by addition of antisolvent is an efficient way to slow Ostwald ripening, as shown when comparing Figures 4.12B (the dialyzed sample) and Figure 4.22 (the dialyzed sample aged for 7 days at 4 °C), where no observable change in particle dimensions was noted after removal of the organic solvent.

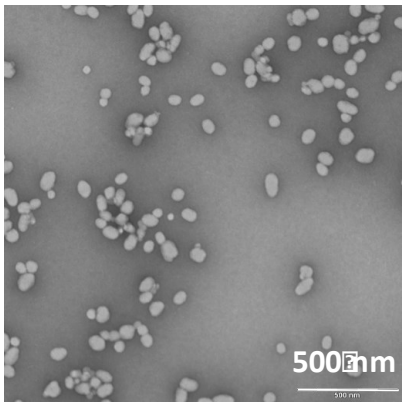

Figure 4.22. Dialyzed BC-B1 nanoparticles stored at 4 °C for 7 days.

β-carotene nanoparticles were also stabilized by PEG_{16}-*b*-PLA_{16}, a diblock copolymer with the same block lengths as those grafted onto B1. In contrast to either B1 or L1, and as shown in Figure 4.23, nanoparticles stabilized by this linear polymer

had irregular shapes and underwent considerable aggregation, demonstrating the importance of polymer architecture on nanoparticle properties.

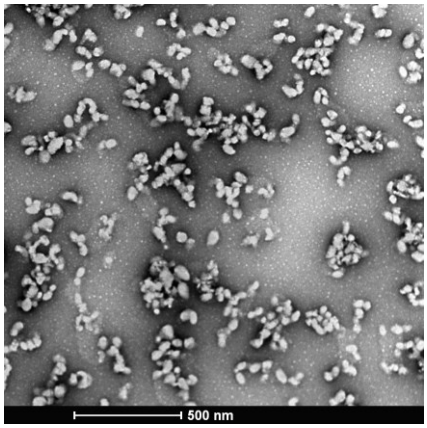

Figure 4.23. Nanoparticles of *β*-carotene stabilized by PEG_{16}-*b*-PLA_{16}. Final conditions were 10% vol. THF, 50% w/w_p *β*-carotene.

As mentioned above, BC-B1 nanoparticles are originally nearly spherical (aspect ratio 1.1) but rapidly (<24 h at 20 °C) adopt an ellipsoidal morphology (aspect ratio 1.4) even as the solvent content in the aqueous phase decreases during dialysis. The change in morphology is accompanied by a ~25% decrease in area. A decrease in particle size after dialysis is not uncommon in flash nanoprecipitation and has been explained as displacement of the organic solvent from the core,[29] leading to smaller nanoparticles through core compaction. It is also likely that Ostwald ripening is contributing to the decrease in size, attributed to mass diffusion. As the solute partitions from the core, where it may have higher solubility if it is present in an amorphous phase,[113] through the polymer layer, it either deposits on the PEG/PLA interface of other (larger) particles or partitions inside their core, to produce the observed changes in average particle size. The morphological evolution from spheres

to ellipsoids must be indicative of anisotropic reorganization, possibly of solute ordering, to decrease the overall free energy of the system despite the penalty of an increase in surface energy associated with the change in morphology.

Long-term suspension properties are also strongly determined by the stabilizing ability of the polymer, implicit in the argument above. According to block chemistry, size, and, as shown here, structure, the polymer may influence nanoparticle suspensions to the extent to which it can affect optimal steric stabilization or by posing diffusional resistance to solute partitioning.[131] We presume both effects contribute to the differences observed between L1- and B1-stabilized samples, as explained below.

PEG length and grafting density contribute to micellar stability based on steric considerations.[155,156] In our case, there is a 3-fold difference in molecular weight of PEG chains between the linear and brush copolymers. The invariability of particle size and shape in BC-L1 samples points to a high steric stability, possibly due to PEG chain length. However, the growth of rod-like nanoparticles in BC-B1 (see Figure 4.18C,D) and the fact that the polymer can self-assemble into worm-like and toroidal structures (Figure 4.10 C,D) would suggest that particles from this polymer have a relatively low barrier to anisotropic aggregation, similar to that observed for polyelectrolyte stabilized nanoparticles.[157]

However, the PLA block of the copolymer, assumed to adsorb to solute nanoparticles through hydrophobic interaction and arrest their growth, can act as a barrier to solute

diffusion depending on its physical state. Studies regarding the diffusion of small molecule probes through thin polymer films have shown that probe diffusion depends on its molecular volume as well as on the proximity of the system temperature to the glass transition temperature of the polymer matrix (T_g).[158-160] For a given solute, translational diffusion coefficients can increase by orders of magnitude with a relatively modest rise in temperature within the proximity of T_g. The dependence of the glass transition temperature on the number-average molecular weight of a polymer (M_n) is given by the Flory-Fox equation

$$T_g = T_g^{\infty} - \frac{K}{M_n} \quad (4.3)$$

where T_g^{∞} is the glass transition temperature of polymer with an infinitely high molecular weight and K is a constant that takes into consideration the excess free volume associated with chain ends. For PLA, these parameters are T_g^{∞} = 57 °C and K = 7.4 × 10^4.[161] Assuming that surface PLA chains have only one free chain end (the other is either attached to the PEG block or to PGMA through a linker), the value of K would be half of that reported (3.7 × 10^4) according to free volume considerations. L1 and B1 have PLA blocks with considerably different molecular weights (85 vs. 17 repeat units, respectively) and, therefore, different glass transition temperatures as predicted according to eq 4.3, $T_g^{\text{PLA inL1}}$ =54°C and T_g^{PLAinB1} =42°C. The latter is in close agreement with the experimentally determined glass transition temperature of the PLA side-chain (with 18 repeat units) pendant from a polynorbornene backbone (T_g = 45 °C).[162]

The thermal properties of B1 were examined by differential scanning calorimetry. As shown in Figure 4.24, a single glass transition is observed at 13 °C, which is reasonable since PEG and PLA have excellent miscibility.[19,163] When the polymer has undergone collapse in water, the T_g of PLA is expected to increase as PEG should segregate to the aqueous phase and reduce plastization. In that case, however, water may act to enhance the segmental mobility of PLA.[164,165] While we ignore the extent to which this occurs on L1- or B1-nanoparticle surfaces, we believe that the accelerated ability of BC-B1 toward Ostwald ripening in cosolvent mixtures may be influenced by increased mobility of the PLA block, facilitating solute diffusion through it. This enhanced mobility of the PLA block may also enable the solute to adopt a preferred short-range order, manifested in anisotropic particle growth and aggregation.

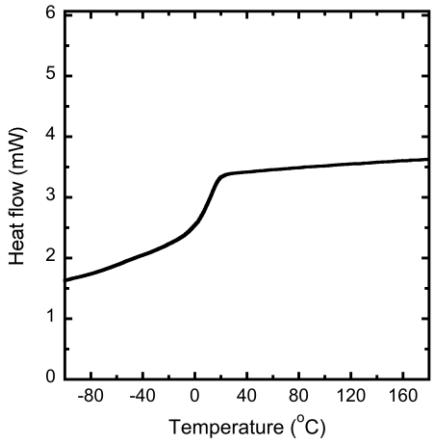

Figure 4.24. Differential scanning calorimetry trace of B1, showing the glass transition of the PLA block at 13 °C.

The presence of rod-like structures in BC-B1 samples aged in cosolvent mixtures indicates nonisotropic particle growth, possibly resulting from solute ordering.

Among the three solutes studied (β-carotene, styrene oligomer, and AuNPs), this effect was only observed for the crystallizable β-carotene. To examine the presence of β-carotene crystals in nanoparticles, particularly in ellipsoidal ones, we performed X-ray scattering and electron diffraction on a sample prepared with 10% THF and dialyzed, and a sample annealed in 25% THF in which long rods had formed. TEM images of both are included in Figure 4.25.

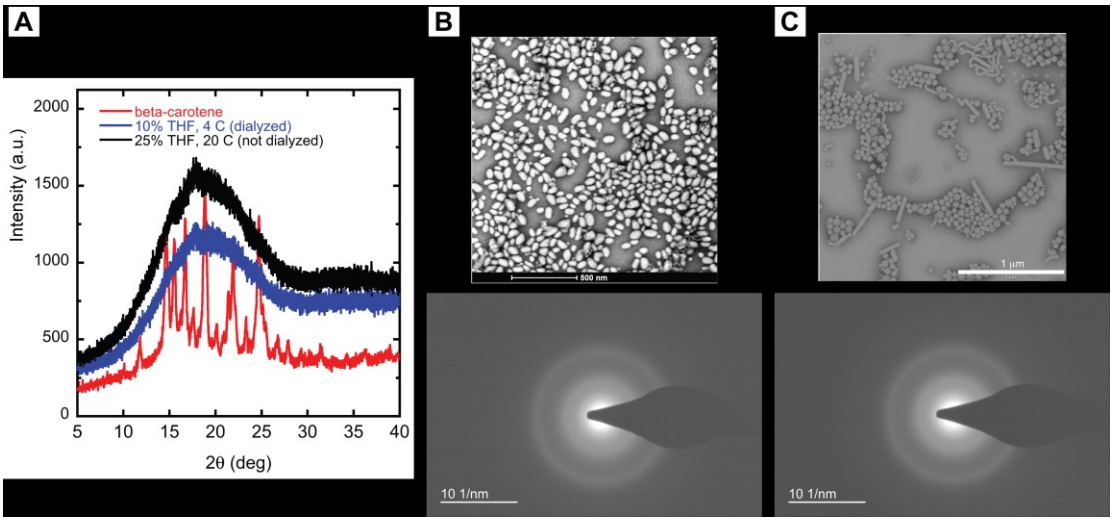

Figure 4.25. XRD of β-carotene and dialyzed BC-B1 nanoparticles.

As shown, X-ray scattering from both BC-B1 samples revealed only an amorphous phase, as the strong Bragg peaks characteristic of the solute were absent. Prior studies of solid dispersions of crystalline drugs have shown that laboratory scale wide-angle X-ray scattering has a low detection limit of crystals corresponding to 5% vol.[166] Hence, we examined electron diffraction patterns acquired from TEM but found no sharp spots, indicating that β-carotene was not present in a crystalline state in either case. The presence of long rods observed for the sample prepared at higher cosolvent content, along with the absence of diffraction spots, is suggestive of short-range

solute ordering; however, we cannot exclude crystal damage caused by exposure to high electron dosage, which can ultimately destroy organic crystals.[166]

4.4 Conclusions

We examined the ability of an asymmetric macromolecular brush, bearing poly(ethylene glycol) and poly(D,L-lactide) side chains, to stabilize hydrophobic solute nanoparticles formed by a rapid change in solvent quality. In contrast to linear diblock copolymers consisting of the same components and longer block lengths, which formed spherical nanoparticles, or the same block lengths, which resulted in ill-defined aggregates, the brush amphiphile enabled the formation of particles exhibiting unique morphologies, highly dependent on the physicochemical characteristics of the solute. Unusual ellipsoidal β-carotene nanoparticles, and moreover, the rod-like particles that result from their anisotropic evolution in cosolvent mixtures, appear to be the product of a combination of Ostwald ripening and particle aggregation, enabled by the mobility of the hydrophobic component of the polymer, which itself is attributed to low molecular weight and low glass transition temperature. The architecture of the polymer is believed to influence particle formation by its ability to undergo intramolecular collapse, resulting in nanoparticles with high polymer content, as shown for the encapsulation of AuNPs. As shown here, asymmetric amphiphilic molecular brushes may be used as hydrophobic drug stabilizers and potentially assist the shape control of nonspherical aggregate morphologies.

Chapter V: Amphiphilic Brush Copolymers as Single-molecule Carriers of Hydrophobic Solutes

5.1 Introduction

The self-assembly of amphiphilic polymers in a selective solvent for one of the components is a commonly used method for the formation of nanostructures with applications ranging from drug delivery to oil recovery.[8,57,167] Depending on the chemical structure of the polymer, hydrophobic association –counterbalanced by hydrophilic repulsion– can occur as an intermolecular process or intramolecularly, leading to unimolecular micelles or unimer micelles.[168-174] For their structural similarity to proteins, the formation of unimer micelles has largely been examined for random copolymers of monomers bearing short hydrophilic and hydrophobic moieties, on occasions referred to as protein-like copolymers.[172-174] However, the advancement of controlled polymerization methods enabling the synthesis of complex macromolecular architectures has also allowed the study of intrachain association of polymers with more complex architecture such as graft copolymers that possess a hydrophobic backbone and hydrophilic side-chains.[50,81,106] For both systems, it is generally recognized that the parameters that influence intra- vs. intermolecular assembly include the type of hydrophobes, hydrophobe sequence distribution and grafting density, hydrophilic-to-hydrophobic balance, and polymer concentration.[81,106,168,169,171,172] Hydrophobically-driven self-assembly of macromolecular brushes –graft copolymers wherein graft length exceeds graft spacing– exhibiting an amphiphilic character are far less studied. For this class of

macromolecules, side-chain excluded volume effects force the backbone to adopt an extended conformation resulting in a cylindrical worm-like morphology.[65,175,176] Similar to their short side-chain counterparts, amphiphilic macromolecular brushes can also self-assemble into unimer micelles, the morphology of which will be influenced by the arrangement of hydrophilic and hydrophobic chains within the molecule.[66,136,177]

In previous work we have shown that, depending on the hydrophilic/hydrophobic balance and processing method (i.e., rapid vs. slow change in solvent quality), macromolecular brushes bearing relatively short hydrophilic and hydrophobic side-chains can assemble into a variety of structures, including unimolecular spheres, and multimolecular worms or toroids.[136] In the context of drug delivery, unimolecular micelles have unique properties that distinguish them from intermolecular constructs including higher stability to dilution - relevant for injection into the bloodstream, conditions[9,17,51] and a worm-like morphology - relevant for circulation time and biodistribution.[73,177] Despite the tremendous potential of unimer micelles in drug delivery, there is to the best of our knowledge, no detailed study which examines their use as stabilizers of hydrophobic solutes via non-specific interactions.

In this chapter, we discuss the intramolecular association of macromolecular brushes to produce unimolecular spherical micelles, triggered by the presence of hydrophobic solutes. The formation of spherical unimolecular aggregates is sensitive to solute concentration, above which stabilization becomes a multimolecular event.

5.2 Materials and Method

5.2.1 Materials and Characterization

All reagents were commercially available and used as received unless otherwise noted. Glycidyl methacrylate (GMA, Aldrich 97%) was passed through a short basic alumina column to remove initiator. 2,2′-Azobis(2-methylpropionitrile) (AIBN) and D,L- lactide were recrystallized from methanol and anhydrous ethyl acetate respectively. 1,8-Diazabicyclo[5.4.0]undec-7-ene (DBU) was kept over molecular sieves (3 Å) overnight. Deionized water was purified in a Barnstead Nanopure system to a final resistance of 18.2 mΩ; it will be referred to as Nanopure water.

Gel Permeation Chromatography (GPC) was performed on a Waters 1515 Isocratic HPLC equipped with three Styragel® columns (HR4, HR3, 300 mm x 7.8 mm) connected in series, a differential refractive index detector (Waters 2414) and a UV-visible detector (Waters 2489). HPLC grade THF was used as the eluent, at a flow rate of 1 mL/min. Molecular weights are reported referenced to polystyrene standards (Shodex SL-105). ^{1}H NMR spectra of polymers were recorded on a Bruker AV 400 MHz spectrometer in either $CDCl_3$ or DMSO-d_6, ^{1}H NMR spectra of micelles were recorded in either D_2O or a mixture of D_2O and Acetone-d_6. Spectra were referenced to $CHCl_3$ (7.26 ppm) or DMSO-d_6 (2.50 ppm). Diffusion ordered spectroscopy (DOSY) were performed on a Bruker AV 400 MHz spectrometer, equipped with a 5 mm PABBO-BB ^{1}H probe. Dynamic Light Scattering was conducted on a Malvern Instruments Nano-ZS ZetaSizer equipped with a 4 mW He-Ne laser operating at 633 nm. All measurements were performed at 25 °C at a scattering angle of 173°.

Fluorescence spectroscopy was carried out on a Fluorolog-3 system (HORIBA Jobin Yvon Inc., NJ). Bright-field TEM imaging was performed on a FEI Technai 12 Twin Transmission Electron Microscope operated at an acceleration voltage of 100 kV. All TEM images were recorded by a SIS Megaview III wide-angle CCD camera. TEM grids (carbon-coated copper or formvar-carbon grid, Electron Microscopy, Hatfield, PA) were ionized under plasma before preparation. Grids were placed on top of a single drop of sample suspension (20 μL) for 5 minutes, washed with 5 drops of doubly distilled water and placed onto a drop of 2 wt% aqueous uranyl acetate solution for 30s. Excess solution was blotted off with filter paper and samples were allowed to dry at room temperature prior to imaging.

5.2.2 Polymer Synthesis

The amphiphilic brush copolymer was synthesized by a four-step reaction.[105] Details of each step are provided below.

Synthesis of the $PGMA_{721}$ backbone

GMA (4 mL, 0.029 mol), 2-cyano-2-propyl benzodithioate (CPB) (5.8 µL, 0.030 mmol,) and AIBN (0.99 mg, 0.0085 mmol) were added to a clean and dry round bottom flask equipped with a magnetic stir bar and a septum. Reagents were dissolved in 4 mL of benzene, and the mixture was bubbled with argon for 1 h. The reaction was conducted at 60 °C for 16 h. Polymerization was stopped by immersing the flask in an ice bath and opening it to atmosphere. Aliquots were taken during the polymerization to evaluate monomer conversion. Samples were diluted with

dichloromethane and precipitated in methanol and the resulting precipitate was dried under vacuum. Yield: 67.4%. Monomer conversion (determined by ^{1}H NMR) is 72.1%. The degree of polymerization (DP) of PGMA was estimated by conversion. The ^{1}H NMR spectrum of the resulting polymer is provided in Figure 5.1. Polydispersity was determined by GPC: Mw = 92,597 g/mol, $Đ$ = 1.18.

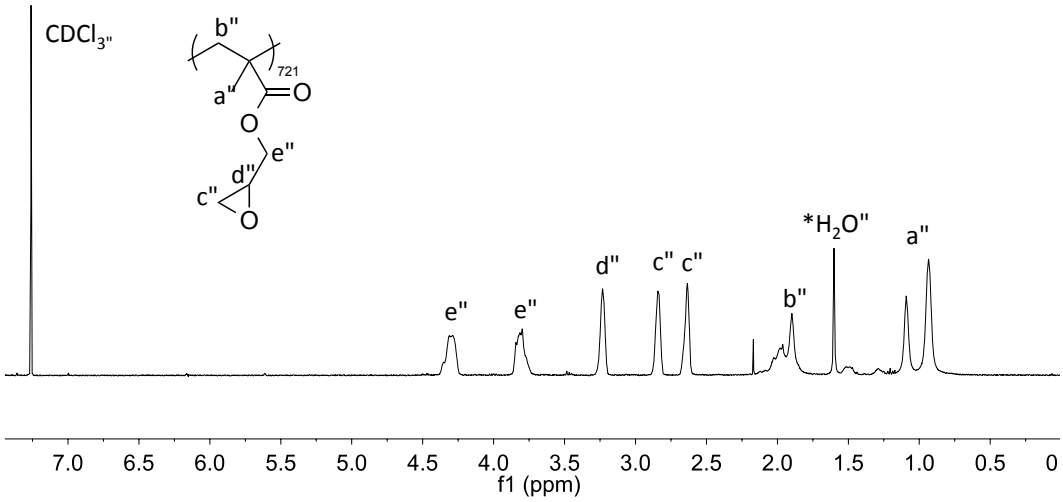

Figure 5.1. ^{1}H NMR and peak assignments of $PGMA_{721}$ backbone.

Aziodolysis of $PGMA_{721}$ ($PGMA_{721}$-N_3)

PGMA (1 g, 7.03 mmol epoxy groups) was added to a round bottom flask and dissolved in N,N-dimethylformamide (DMF, 30 mL). Sodium azide (1.37 g, 21.07 mmol) and ammonium chloride (1.13 g, 21.13 mmol) were added once the polymer was visibly dissolved. Azidolysis was conducted at 50 °C under argon for 24 h. The resulting solution was cooled to room temperature and diluted with tetrahydrofuran (THF). Salts were filtered off and the solution was concentrated before precipitation

into Nanopure water. Solids were lyophilized. Yield: 62.3%. ^{1}H NMR peaks assignments are shown in Figure 5.2; signals indicate complete conversion.

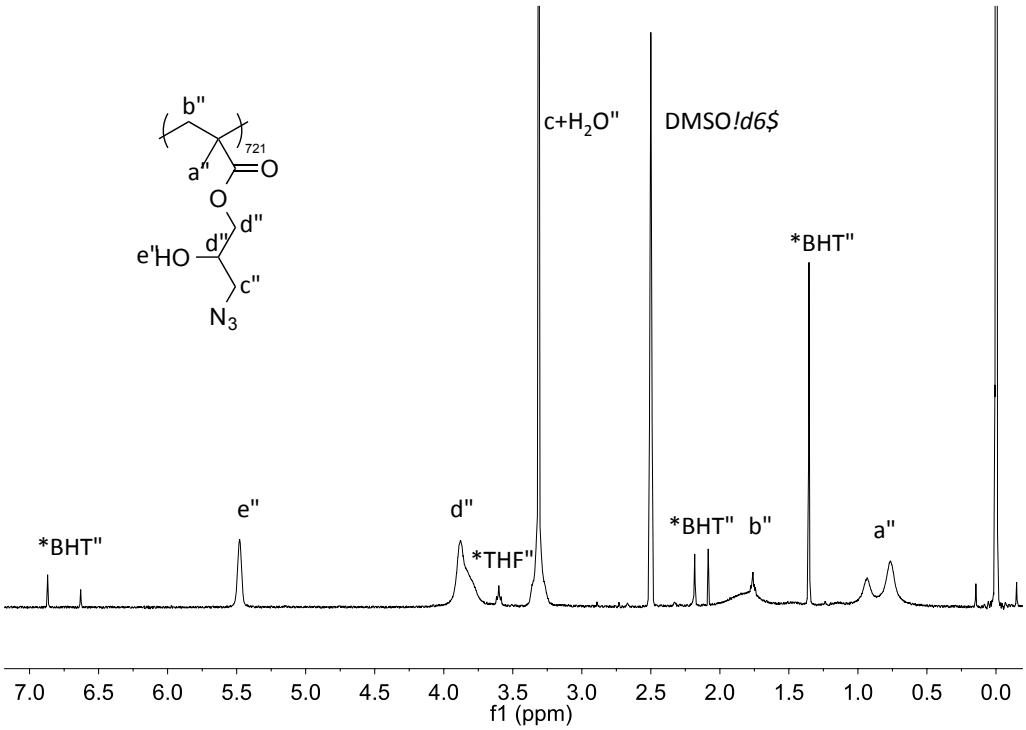

Figure 5.2. ^{1}H NMR and peak assignments of $PGMA_{721}$-N_3.

Synthesis of $PGMA_{721}$-g-PLA_{15}

$PGMA_{721}$-g-N_3 (300 mg, 1.62 mmol –OH group) and D,L-lactide (3.243 g, 22.5 mmol) were loaded into a round bottom flask, and placed under high vacuum at 36 ºC for ~ 5 hours. After backfilling with argon, anhydrous DMF (~ 35 mL) was added to dissolve the reagents. DBU (125.2 µL, 0.84 mmol) was then injected and the reaction was allowed to proceed for 1.5 h under argon at room temperature. Polymerization was quenched by addition of benzoic acid (256 mg, 1.51 mmol). DMF was removed under vacuum and the polymer was re-dissolved in THF, followed by precipitation

into a mixture of Nanopure water and methanol (1:1, vol). Solids were lyophilized to remove water. Yield: 80.6 %. ^{1}H NMR of the resulting grafted polymer is shown in Figure 5.3. The degree of polymerization of PLA side chains was calculated based on signals e and e'.

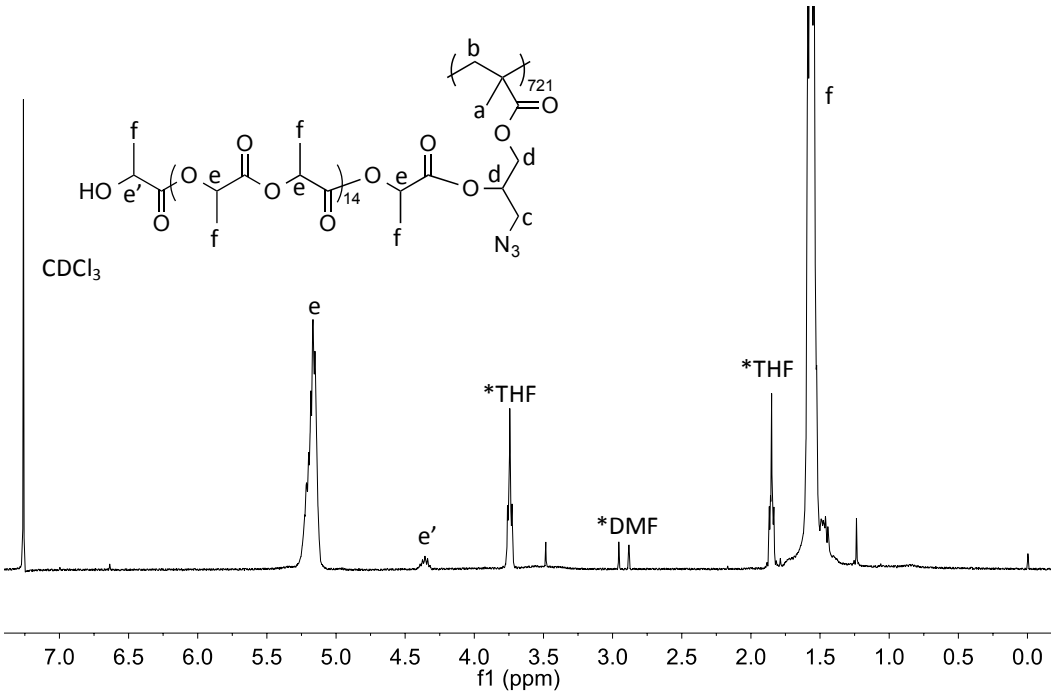

Figure 5.3. ^{1}H NMR and peak assignments of $PGMA_{721}$-g-PLA_{15}.

Synthesis of alkynyl-PEG_{45}

$mPEG_{45}$ (10.554 g, 5.28 mmol) was transferred to a round bottom flask and placed under high vacuum for around 5 h. The flask was backfilled with nitrogen prior to the addition of 5-hexynoic acid (700 μL, 6.33 mmol) and 4-(Dimethylamino) pyridine (DMAP) (0.264 g, 2.16 mmol), and purged with nitrogen for 30 minutes. Anhydrous dichloromethane (DCM, 40 mL) was added and the reagents were allowed to dissolve. Then, a solution of N,N'-dicyclohexylcarbodiimide (DCC) (2.179 g, 10.56

mmol) in anhydrous DCM (8 mL) was added to the reaction mixture dropwise, and the reaction was carried out overnight at room temperature The solution was filtered and concentrated by rotary evaporation; the product was recovered by precipitating this solution into cold diethyl ether and dried under vacuum. Yield: 80.3%. ^{1}H NMR of the product is shown in Figure 5.4 and indicates quantitative conversion.

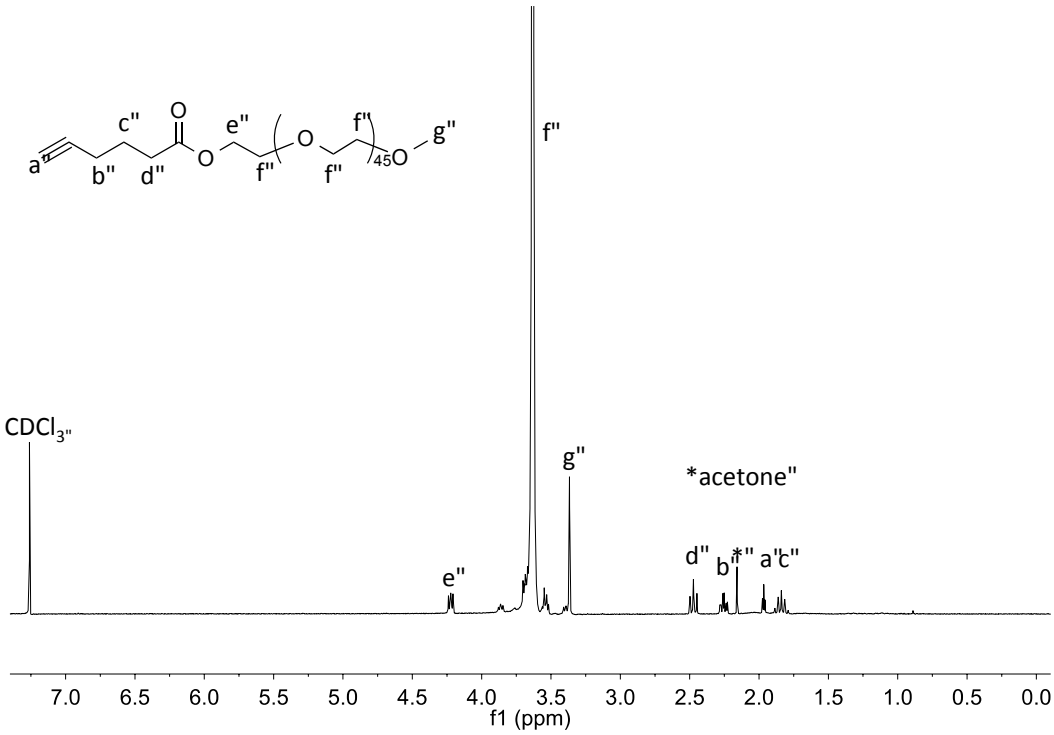

Figure 5.4. ^{1}H NMR and peak assignments of Alkynyl-PEG.

Synthesis of PGMA$_{721}$-g-PEG$_{45}$/PLA$_{15}$

Alkynl-PEG was grafted onto PGMA$_{721}$-g-PLA$_{17}$ via *'click'* reaction, catalyzed by $CuSO_4$•$5H_2O$/ascorbic acid. Molar ratio of -N_3, alkynyl groups, $CuSO_4$•$5H_2O$ and ascorbic acid was kept at 1:1.05:0.2:1. PGMA$_{721}$-g-PLA$_{15}$ (600 mg, 0.26 mmol) was and alkynyl-PEG (582.3 mg, 0.28 mmol) were placed in a round bottomed flask and

dissolved in DMF (60 mL). Ascorbic acid (46.5 mg, 0.26 mmol) was added and the solution was bubbled with argon for 30 min. Finally, $CuSO_4 \cdot 5H_2O$ (13.2 mg, 0.05 mmol) was added under argon and the reaction was allowed to take place at room temperature for 12 h under argon. The product was purified by dialysis against Nanopure water for 7 days and lyophilized. Yield: 96.8%. ^{1}H NMR spectrum of the polymer is shown in Figure 5.5. PEG grafting was estimated to be 96.8%. Diffusion-ordered NMR spectroscopy (DOSY) was conducted to confirm the purity of final product. Figure 5.7 includes the DOSY spectrum of the final product, and, as comparison, a mixture of final product with 5wt% Alkynyl-PEG to demonstrate that no unreacted PEG was present in the product.

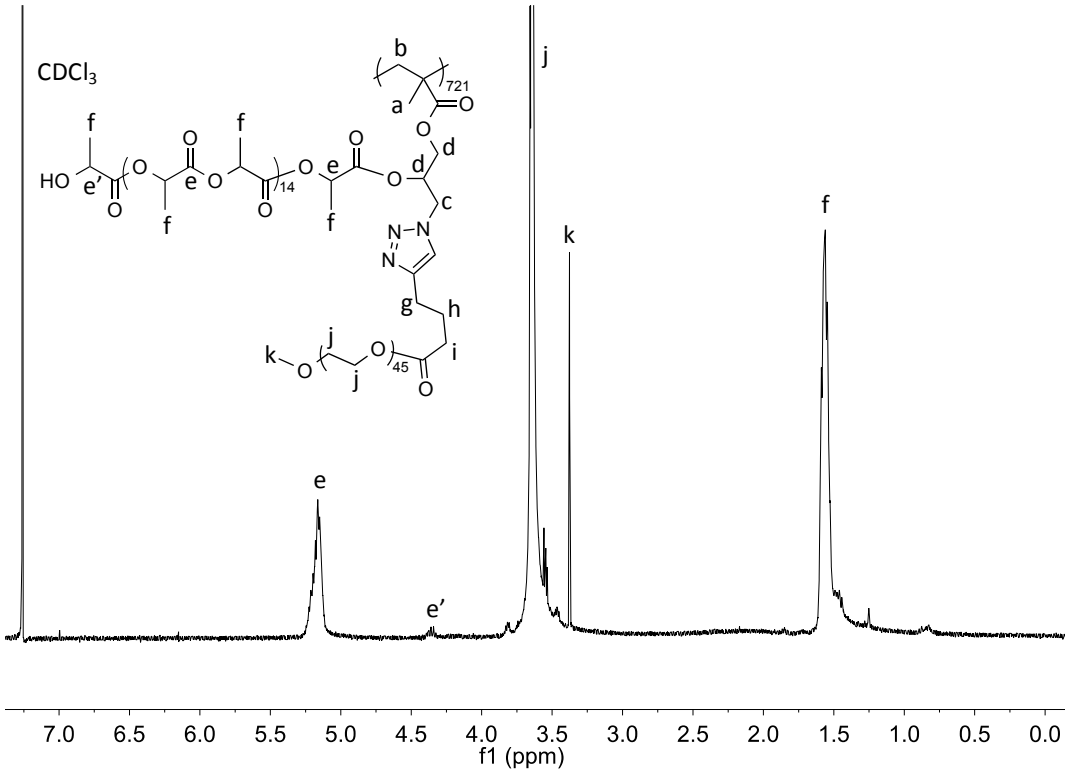

Figure 5.5. ^{1}H NMR and peak assignments of $PGMA_{721}$-*g*-PEG_{45}/PLA_{15}.

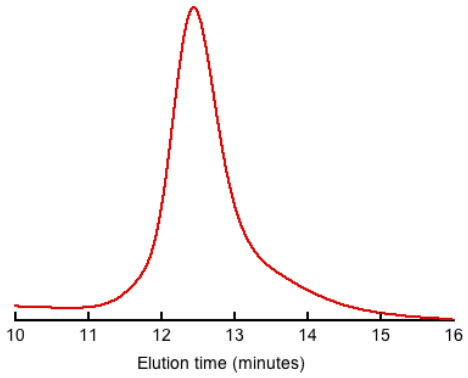

Figure 5.6. Gel permeation chromatogram of PGMA721 backbone.

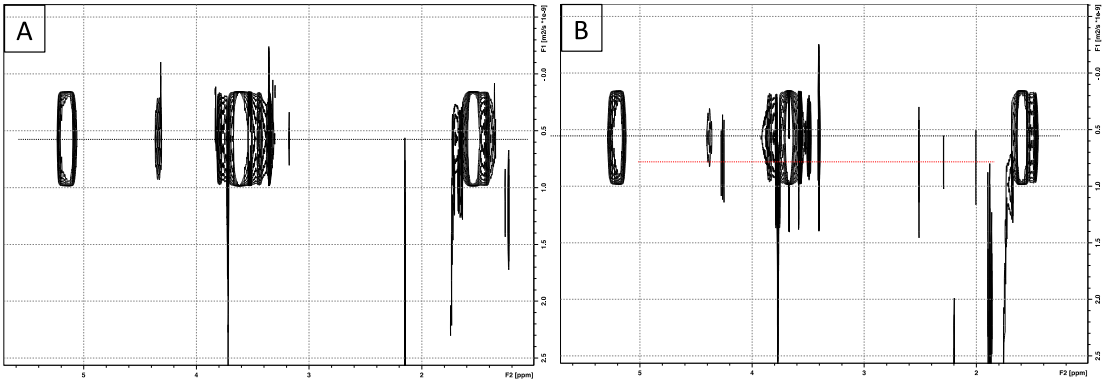

Figure 5.7. Diffusion ordered NMR spectroscopy of the polymer after reaction with PEG_{45}-alkyne was used to confirm the purity of the final product by the absence of signals corresponding to free PEG. DOSY NMR spectra of $PGMA_{721}$-*g*-PEG_{45}/PLA_{15} (A), and 95 wt % $PGMA_{721}$-*g*-PEG_{45}/PLA_{15} with 5 wt % alkynyl-PEG (B). A single trace is displayed in the former, compared to the two traces observed for the latter case, marked with black and red lines.

5.2.3. Differential Refraction index (dn/dc) Measurement

The change in refractive index with concentration (dn/dc) was measured by an Optilab-rEX refractive index detector (Wyatt Technology) using a laser light wavelength of 658 nm. The temperature was set at 25 °C for throughout the measurement. Samples were passed through 0.45 µm PVDF syringe filters (Thermo

Scientific) and injected via the syringe pump (New Era Pump System, NE-1000) at a fixed velocity of 0.2 mL/min. Six concentrations were surveyed for the polymer in dimethylformamide (anhydrous), ranging from 0.1 to 2 mg/mL. Seven samples were surveyed for nanoparticles suspensions in Nanopure water, ranging from 0.02 to 0.2 mg/. (dn/dc) values were analyzed by the Astra 6.1 software.

5.2.4. Static Light Scattering Measurement

SLS Measurements were performed with a DAWN HELEOS II (Wyatt Technology) with a 120mW GaAs linearly poloarized laser operated at 658 nm. Filtered samples (described above for refractive index measurements) were injected at a fixed velocity of 0.2 mL/min. Polystyrene (20 kDa, Fluka; 5 mg/mL solution in DMF) and dextran (9-11 kDa, Aldrich, 5 mg/mL solution in Nanopure water) was used as standards to normalize measurements for polymer and micelles respectively. (dn/dc) values were used to determine absolute molecular weights, and the weight average molecular weight (M_w) was extracted from Zimm plots using Debye and Zimm models (for the polymer and micelles, respectively) using Astra 6.1. The resulting zimm plots of polymer PGMA721 and nanoparticles from PGMA721 are provided in Figure 5.7 and Figure 5.8, respectively.

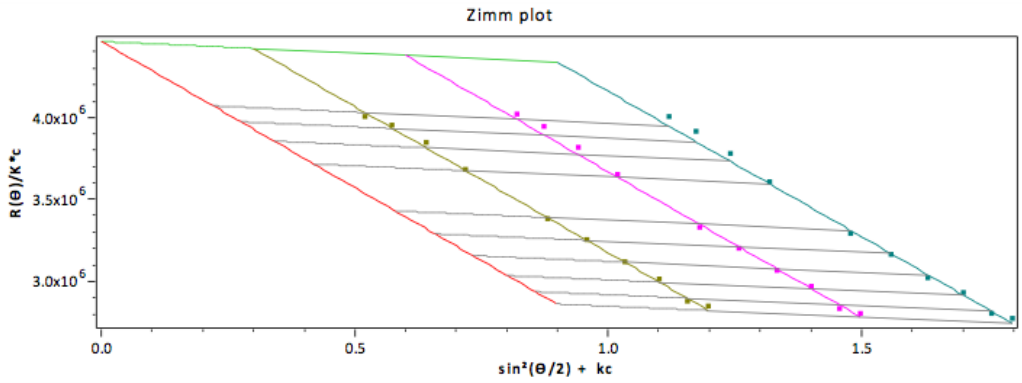

Figure 5.7. Zimm plot of multi-angle light scattering intensities from polymer solutions.

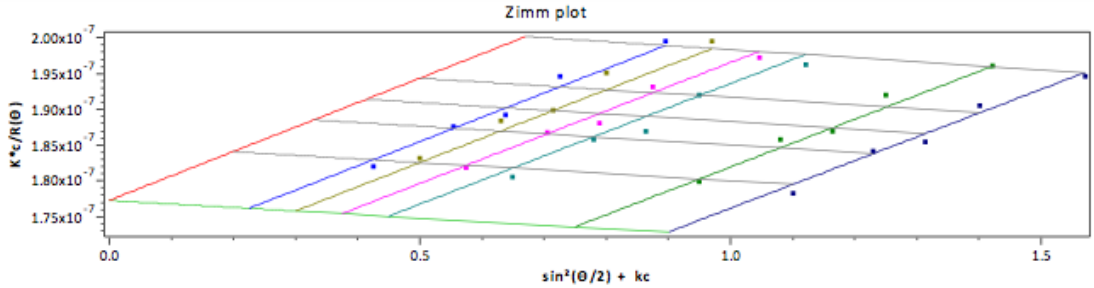

Figure 5.8. Zimm plot of multi-angle light scattering intensities from nanoparticle solutions.

5.2.5 Determine Critical Micelle Concentration

The critical micelle concentration (C_{CMC}) of polymer was measured by using pyrene as a probe. For this, 50 µL Pyrene solution in acetone ($6x10^{-5}$ M) was loaded into a 5mL clean scintillation vial and left open under the hood to allow for complete evaporation of the solvent. Then, 50 µL of polymer solution (0.001 to 2 mg/mL in acetone) were added to each of 10 vials containing pyrene, followed by 1mL of water. Final polymer concentration ranged from 50 µg/ml to 0.1 mg/mL. Samples were vigorously stirred with a vortex mixer (~ 1 min), and left to shake gently overnight to evaporate acetone. Excitation and emission spectrum were recorded by fluorescence

spectroscopy. Pyrene excitation was scanned from 300 to 360 nm at an emission wavelength of 390 nm. Excitation and emission bandwidths were set at 2 nm. The intensity ratio from signals at 336 and 334 nm (I_{336}/I_{334}) was analyzed as a function of polymer concentration. C_{CMC} values were read from the intersection between curve tangents at low and high concentrations.

5.2.6. Diffusion-ordered NMR Spectroscopy (DOSY) Measurement

Polymer solutions of 5 mg/mL were prepared in $CDCl_3$. To avoid convection effects resulting from sample heating during gradient pulses, the temperature was maintained at 17 ± 0.2°C. DOSY spectra were acquired with the ledbpgp2s pulse program. Gradient strength was linearly incremented in 32 steps from 5% to 80% of its maximum value. Diffusion time and gradient pulse lengths were set to 75 ms and 2 ms, respectively. The diffusion dimension of the 2D DOSY spectra was processed with a Bruker topsin software (v. 2.1).

5.2.7. Polymer Self-assembly

The polymer was dissolved in THF at concentrations ranging from 1 to 20 mg/mL. Rapid self-assembly was carried out in a four-inlet vortex mixer described elsewhere.[28] Nanopure water was charged into three 50 mL syringes (Hamilton, NJ) and the organic solution into a 10 mL syringe, and mounted on two separate syringe drivers (PHD Ultra, Harvard Apparatus). Flow rates of water and organic streams were 108 mL/min (water) and 12 mL/min (THF) to achieve a 10% (v/v) THF concentration. Samples were collected and dialyzed (6-8 kDa MWCO, Fisherbrand)

against Nanopure water for 24 h at 20 °C. Water was replenished every 4 h throughout the dialysis process. Samples were stored in clean scintillation vials, and unless otherwise noted, kept under refrigeration at 4 °C.

5.2.8 Flash Nanoprecipitation

The protocol described above was used to prepare solute loaded nanoparticles, with the exception that both the polymer and the solutes (rose bengal lactone or probucol) were dissolved together in tetrahydrofuran. Dialyzed samples were collected and filtered through 0.45 μm PVDF syringe filters (Thermo Scientific) and stored in clean centrifuge tubes (Falcon® Tube). Loading capacity (LC) and efficiency (LE) in nanoparticles (NP) are estimated as:

$$Loading\ capacity\ (LC,\%) = \frac{Mass\ of\ solute\ in\ NP}{Mass\ of\ NP} \times 100$$

$$Loading\ efficiency\ (LE,\%) = \frac{Mass\ of\ solute\ in\ NP}{Mass\ of\ solute\ in\ feed} \times 100$$

LC and LE were determined by a Varian Cary 50 UV/Vis spectrophotometer (Agilent Technologies, Santa Clara, CA). Loaded micelles were lyophilized and dissolved in DMF. Solute concentrations were calculated from calibration curves in DMF, with reference to their absorption at 565 nm (for rose bengal lactone) or 271 nm (for probucol).

5.2.9 Cryogenic TEM

Cryogenic TEM imaging was performed on the FEI Tecnai 12 TWIN Transmission Electron Microscope, operating at 80 kV. 5 μL of sample solution were placed on a

lacey carbon film supported on a TEM copper grid (Electron Microscopy Services, Hatfield, PA). All the TEM grids used for cryo-TEM imaging were treated with plasma air to render the lacey carbon film hydrophilic. A thin film of the sample solution was produced using the Vitrobot with a controlled humidity chamber (FEI). After loading of the sample solution, the lacey carbon grid was blotted using preset parameters and plunged instantly into a liquid ethane reservoir precooled by liquid nitrogen. Vitrified samples were then transferred to a cryo-holder and cryo-transfer stage, which was cooled by liquid nitrogen. To prevent sublimation of vitreous water, the cryo-holder temperature was maintained below -170 °C during the imaging process. All images were recorded by a SIS Megaview III wide-angle CCD camera.

5.2.9 Small-angle X-ray Scattering (SAXS) Measurements

SAXS measurements were performed at the synchrotron X-ray beam line BioCAT 18ID at Argonne National Laboratory. Samples were flown into a capillary cell by a programmed pump (Hamilton, MICROLAB® 500 Series, Reno, NV). The detector (Pilatus 1M) was positioned 2.5 m away from the samples resulting in the range of Q from 0.006 A^{-1} to 0.35 A^{-1}. The X-ray exposure and acquire time were 0.2 s and 5 s, respectively. Ten images were taken to obtain good statistics. Signal of the buffer sample (dialysis medium) was acquired as subtracting background. In addition, both the empty capillary and the one filled with Millipore water were also run to further obtain scattering parameters that are necessary for absolute scaling of the data.

5.2.10 Small-angle Neutron Scattering (SANS) Measurement

Polymers were dissolved in DMSO-d_6 at concentrations of (1, 2, 5 or 10 mg/mL).

Micelles samples (starting polymer concentration of 0.25 and 1 wt %) were dialyzed against deuterium oxide overnight, and the dialysis mediums were collected as solvent baseline. SANS experiments were performed on the NG-7 30 m SANS instrument at the National Institute of Standards and Technology, Center for Neutron Research. An incident wavelength of 6.0 Å was used with sample-detector distances of 1, 4 and 13 m to cover a q-range from $0.003\text{Å}^{-1} < \frac{4\pi sin\theta}{\lambda} < 0.56\text{Å}^{-1}$, where $2\theta$is the scattering angle. All measurements were performed at ambient temperature. The raw data were reduced and analyzed by the IGOR Pro (WaveMetrics), using the SANS reduction and analysis packages provided by NIST.[178] The raw data were corrected for the background and empty cell scattering, sample and empty cell transmission, detector sensitivity and cell thickness. Data were rescaled to an absolute intensity by beam flux method. Scattering from the solvent was subtracted in proportion to its volume fraction.

5.3 Results and Discussion

5.3.1 Molecular Brush Synthesis and Morphology Characterization

To examine the interaction between amphiphilic molecular brushes and hydrophobic solutes, we synthesized a brush copolymer consisting of poly(glycidyl methacrylate) [PGMA] as the backbone, with poly(D,L-lactide) [PLA] and poly(ethylene glycol) [PEG] side-chains (Figure 5.9). Backbone length and hydrophilic content were chosen to target unimolecular constructs; based on prior work we focused on 721 PGMA repeat units and 45 wt % PEG. PGMA was synthesized by reversible addition-fragmentation transfer (RAFT) polymerization and subject to azidolysis to generate

functional groups which served as either an initiation site for the ring-opening polymerization of D,L-lactide, or for conjugation of alkyne-PEG through *'click'* chemistry. Characteristics of the resulting polymer ($PGMA_{721}$-*g*-PEG_{45}/PLA_{14}) are provided in Table 5.1.

Table 5.1. Characteristics of brush amphiphile used in the study.

	Brush Amphiphile	M_n[a] (kg/mol)	M_w[b] (kg/mol)	$Đ$[b]	R_g[c] (nm)	w_{PEG}[a] (% *w*t)
PGMA721	$PGMA_{721}$-*g*-(PEG_{45}/PLA_{14})	3,110	4,470	1.43	40.2	45.7

[a]Determined from ^{1}H NMR spectra. [b]Estimated by M_w(SLS)/M_n(^{1}H NMR). [c]Determined by static light scattering in dimethylformamide.

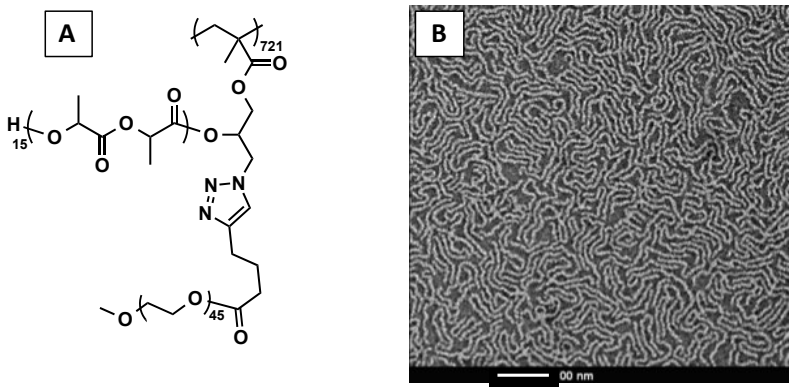

Figure 5.9. (**A**) Structure of the amphiphilic brush copolymer $PGMA_{721}$-*g*-PEG_{45}/PLA_{15}, and its morphology when drop-cast from a good solvent onto TEM grids (**B**). Scale bar corresponds to 100 nm.

In densely grafted molecular brushes, steric repulsion among side-chains forces the molecule into an extended cylindrical morphology.[65,175,176] Individual worm-like chains of $PGMA_{721}$-*g*-PEG_{45}/PLA_{15} were clearly visualized by transmission electron microscopy (Figure 5.9B) by depositing a 0.01 wt % solution of the polymer directly onto TEM grids from dimethylformamide, a good solvent for the polymer. Statistical

analysis of these images reveals an average chain length of ~ 210 nm and a width of 11 nm (Figure 5.10). Although TEM data suggest that the chains exist as cylinders, their exact dimensions in the dry state may differ from those in solution, as the extent of solvent evaporation and chain collapse or interaction with the underlying surface cannot be precisely accounted for in this technique.

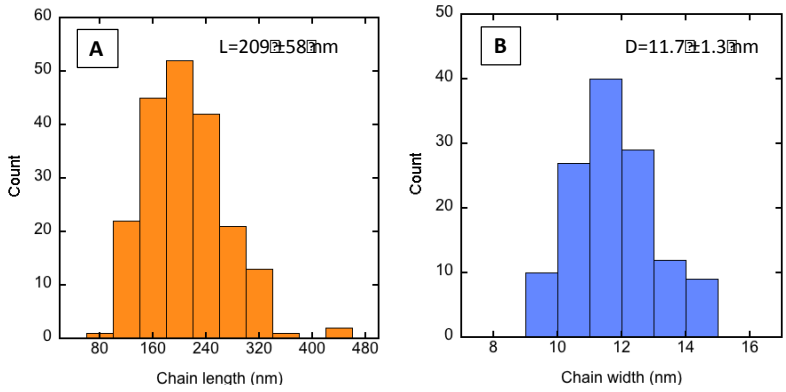

Figure 5.10. Statistical analysis of chain length (**A**) and chain width (**B**) of $PGMA_{721}$-*g*-PEG_{45}/PLA_{14} imaged by TEM from a drop-cast sample of the polymer in DMSO.

A more representative measure of the size and morphology of brushes in solution was provided by light and small angle neutron scattering experiments. SANS measurements were performed over a broad q-range to obtain information regarding the overall size of the polymer (low q-range) and a measure of its stiffness and cross-sectional dimensions (intermediate q-range) (Figure 5.11).[179] The low-q Guinier region was not observed for the copolymer in DMSO at the various concentrations examined (0.1-1.0 % wt), nevertheless it is possible to obtain information regarding its cross-section. SANS data were initially fit to a Guinier-Porod model (Figure 5.12) which yields a dimension parameter (*s*) that describes the shape of the object and its radius of gyration ($R_{g,cs}$).[180,181] For a 1.0 % wt solution of the copolymer, s = 1.1 and

$R_{g,cs}$ = 3.4 nm. The value of the dimension parameter corresponds to that of an elongated or rod-like object (s = 1), as the high slope of the curve at intermediate-q also suggests. In this intermediate-q region, the form factor varied according to $1/Q^{1.3}$ (inset in Figure 5.11) which deviated slightly from the expected $1/Q^{1}$ dependence,[176] and is indicative of a stiff cylinder with a finite radius.[182] The small upturn observed at the lowest-q range was attributed to a small fraction of larger aggregates.[181] The radius of gyration provided by the Guinier-Porod fit was considerably smaller than that resulting from static light scattering measurements (R_g = 40.2 nm) since it referred to the molecular cross-section of the brush. For a cylindrical object, its diameter (d) and cross-sectional radius of gyration are related according to $d = \sqrt{8} R_{g,cs}$,[180] such that the calculated diameter of the brush was d = 9.7 nm, consistent with that measured by TEM. As previously mentioned, cylinder length could not be estimated by SANS as the low-q Guinier region was not observed, and fitting the data to flexible or rigid cylinder models resulted in large variations of this parameter. We therefore assumed brush length to have dimensions similar to those observed by TEM (~ 200 nm).

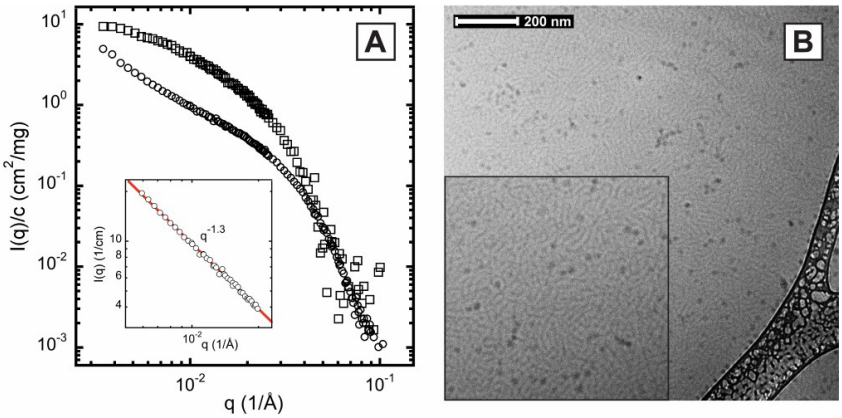

Figure 5.11. (**A**) SANS data of the copolymer in DMSO-d_6 (circles) or D_2O (squares). The inset shows the power-law fit of the former. (**B**) Morphology of the polymer in water showing the presence of cylindrical and spherical particles. Scale bar corresponds to 200 nm.

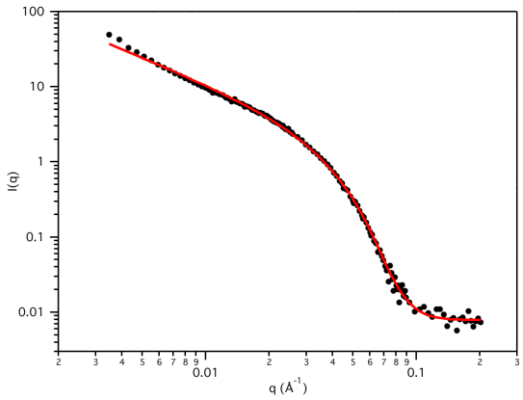

Figure 5.12. Scattering from $PGMA_{721}$-*g*-PEG_{45}/PLA_{14} in DMSO-d_6 and Guinier-Porod model fit.

5.2.3 Self-assembly of Molecular Brush

Brushes were transferred to a predominantly aqueous phase (10% vol THF) by a large and rapid change in solvent quality inside a four-stream vortex mixer.[28] The starting polymer concentration in THF was 10 mg/mL (1 wt %), unless otherwise specified. As estimated by competitive reactions, this method enables micromixing (i.e., mixing at the molecular level) within 40 ms.[28] Complete removal of the organic solvent was

then achieved by dialysis against water for 24 h. Noting that sample preparation for TEM (staining and drying) may alter particle morphology,[183] cryogenic TEM was instead used. As shown in Figure 5.11B, the majority of chains maintained an elongated shape with a small population of co-existing spheres, which were attributed to the polydisperse nature of the PGMA backbone as shorter macromolecular brushes are known to assemble into spherical aggregates.[181] Nanoparticle aggregation number was estimated by static light scattering, comparing the average molecular weight of the polymer in water (M_w = 5.6 × 10^6 g/mol) to its value in solution (DMF, M_w = 4.7 × 10^6 g/mol). The calculated value of 1.2 indicated that despite not having a structure inherently conducive to unimolecular aggregation in water (i.e., hydrophobic blocks tethering the hydrophilic component onto the backbone), the hydrophilic component of the brush offered sufficient steric stabilization to prevent intermolecular aggregation in water. PEG surface exposure in water was determined by ^{1}H NMR to be 92.7%,[20] a value relatively higher to that observed for diblock copolymers of PEG and PLA with similar block sizes.[184]

The scattering curve of the brush in water was notably different to that in DMSO. The difference in scattering patterns could be attributed to a change in the dimensions of brushes when they are in contact with a poor solvent for both the PGMA backbone and the PLA block, or also due to the presence of spherical particles, as observed by cryo-TEM. In the low-q region, the form factor plateaued (~ $1/Q^0$) as is characteristic of a Guinier regime, while in the intermediate-q region, both curves decaed as $1/Q^{1.3}$. When applied to the polymer in water, the Guinier-Porod model yielded s = 0.9 and R_g = 5.6 nm. The value of the dimension parameter still suggested that the polymer

continued to exist as an elongated object, however its decrease compared to the value in a good solvent could also be attributed to the contribution of 3-dimensional globular objects, for which $s = 0$. The increase in radius of gyration of the sample in water compared to that in DMSO, if referring to cylindrical molecules, would imply chain extension of the PEG block as the brush dimension is expected to decrease axially upon collapse of the backbone and PLA. An alternate possibility is that the increase in R_g results from the combined contributions of the cross-section of cylindrical molecules, as well as the comparatively larger radius of gyration of spherical nanoparticles. Since the population of spherical particles was considerably smaller than that of cylinders, as confirmed by cryo-TEM, scattering data were fit to flexible and rigid cylinder models. Of these, the flexible model was found to provide the best fit, yielding contour length (L = 89.0 nm), cylinder radius (R = 6.2 nm) (Table 5.2 and Figure 5.13).

Table 5.2. Summary of SANS and SAXS analysis for $PGMA_{721}$-g-PEG_{45}/PLA_{15} samples in DMSO and water.

solvent	starting polymer concentration (THF, wt %)	SANS				SAXS	
		L^a(nm)	R^b (nm)	λ_k^c (nm)	s^d	L (nm)	R (nm)
DMSO	1		4.9[e]		1.2		
H_2O	0.27					87.2	7.0
D_2O	1	89	6.2	22.2	0.9		
H_2O	2					93.0	7.0

[a-c]Cylinder radius (R) and length (L) estimated by a flexible cylinder model, unless otherwise noted. [d]Dimension parameter from a Guinier-Porod fit. [e]R_g was determined from a Guinier-Porod fit and used to estimate cylinder radius as noted in the text.

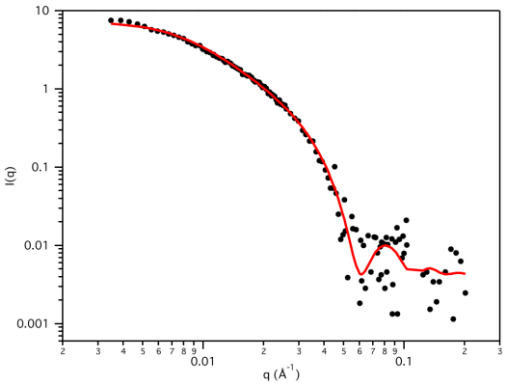

Figure 5.13. Scattering from $PGMA_{721}$-*g*-PEG_{45}/PLA_{14} in D_2O and flexible cylinder model fit.

SAXS measurements were used to examine the internal structure of the particles and provide information regarding their morphology. Measurements were carried out for micelles with starting polymer concentrations (in THF) of 0.27 wt % and 2 wt %. The asymmetric shaped pair distribution function $p(r)$ that results (Figure 5.14), suggests the presence of elongated structure. For an ideal rigid cylinder, $p(r)$ has a characteristic bell shape at low r, followed by an inflection point and a linear decrease to 0 at larger r.[185] For the sample at 0.27 wt %, an additional shoulder was observed at larger r and the linear region does not decay to 0, indicating a more flexible (worm-like) nature. Similar results were observed for the 2 wt % sample. Data were fit according to a core-shell cylinder model (Figure 5.15). The fit parameters obtained from this model reveal an estimated cylinder length between 87 and 93 nm, with a cross-sectional diameter of ~ 14 nm. Aggregation numbers were estimated to be 1.4 for both 0.27 wt % and 2 wt % samples, which were slightly larger than those estimated by SLS, but still support unimolecular assembly.

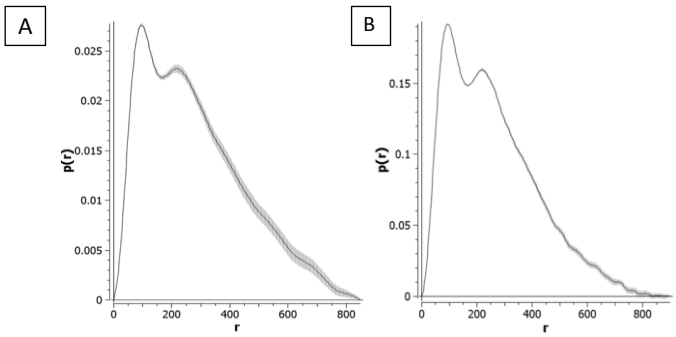

Figure 5.13. Pair distribution function $p(r)$ of PGMA$_{721}$-*g*-PEG$_{45}$/PLA$_{14}$ in D_2O. Samples were prepared with starting polymer concentrations (in THF) of (A) 0.27 wt % and (B) 2 wt %.

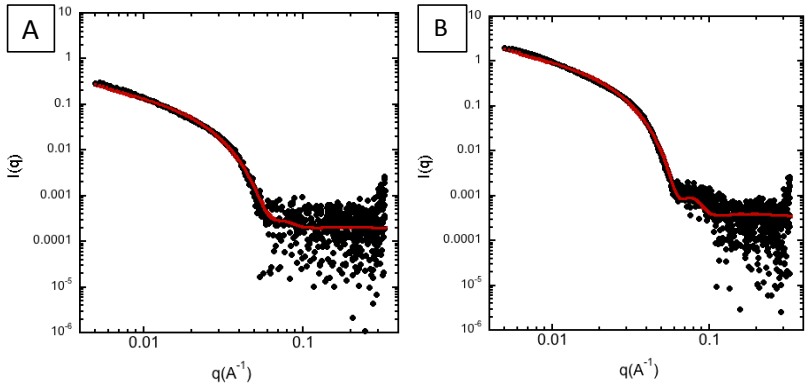

Figure 5.14. Scattering of PGMA$_{721}$-*g*-PEG$_{45}$/PLA$_{14}$ in H_2O and core-shell cylinder model fit. Samples were prepared with starting polymer concentrations (in THF) of (A) 0.27 wt % and (B) 2 wt %.

A summary of SANS and SAXS results is presented in Table 5.2. Taken together, the data revealed that despite the change in solvent quality, amphiphilic brushes preserved, for the most part, an elongated morphology. Hydrophobic collapse of the PGMA backbone and PLA side-chains in water, is counterbalanced by steric effects attributed to the high grafting density of PEG, resulting in a decrease in brush length accompanied by an increase in brush radii. On the other hand, the spherical particles that were found to co-exist with cylindrical ones may result from brushes with shorter

backbones, or chains with insufficient PEG grafting.

5.3.3 Solute-triggered Nanoparticle Formation

Rose bengal lactone (RBL) and probucol (PBC) were selected as model drugs to examine the ability of the amphiphilic brush to act as a stabilizer of hydrophobic solutes. RBL (clog P = 9.31) is a known potent inhibitor of kinesin and an effective sensitizer of singlet oxygen,[108,109] whereas PBC (clog P = 9.62) is an anti-hyperlipidemic drug and a BCS class II model drug;[186,187] logP values were estimated by using molinspiration.com. Solute loading was carried out by a rapid change in solvent quality, with both the brush copolymer and the solute dissolved in the organic phase prior to mixing. Loading was examined over a solute range from 5 - 75 % $w/w_{polymer}$. In contrast to the morphology of the brush in DMSO or in water, the presence of 15 % wt RBL (or PBC) triggered a collapse of the copolymer into, predominantly, spherical nanoparticles as judged by both cryo-TEM and TEM (Figure 5.15).

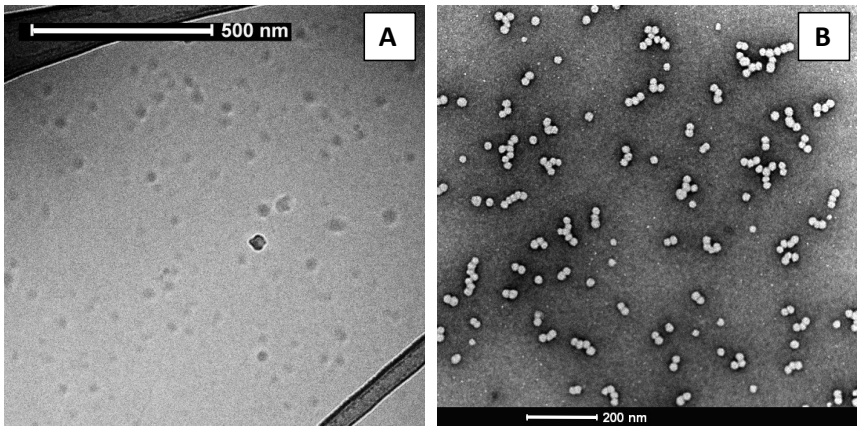

Figure 5.15. TEM (A) and cryo-TEM (B) images of rose bengal lactone (RBL) nanoparticles stabilized with $PGMA_{721}$-*g*-PEG_{45}/PLA_{15}. RBL feed used in both cases was 15 % $w/w_{polymer}$. Particle aggregation, as observed in image (B**)**, is attributed to effects during sample preparation.

Neutron scattering curves of RBL and PBC nanoparticles did not differ much from those of the polymer in water (Figure 5.16), and when fit with the Guinier-Porod model, yielded an even lower value of the structure parameter ($s \sim 0.7$) than in water, but still significantly different to that expected for spheres. We attribute this to worm-like chains which were sparsely found upon careful examination of the samples by cryo-TEM (Figure 5.17). The presence of worm-like structures suggests that self-assembly of the polymer in the absence of solute took place, potentially due to micromixing limitations. In contrast to the polymer in DMSO which exhibited two relaxation times consistent with an elongated structure of high aspect ratio (Figure 5.18), dynamic light scattering of loaded samples revealed a single τ suggesting the existence of a low volume fraction of elongated structures with a high level of anisotropy.[188]

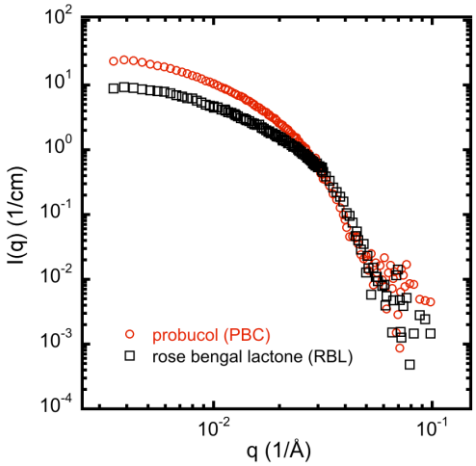

Figure 5.16. SANS of loaded nanoparticles with 15 w/w_p % solute. Particles were prepared with an initial polymer concentration of 10 mg/mL in THF.

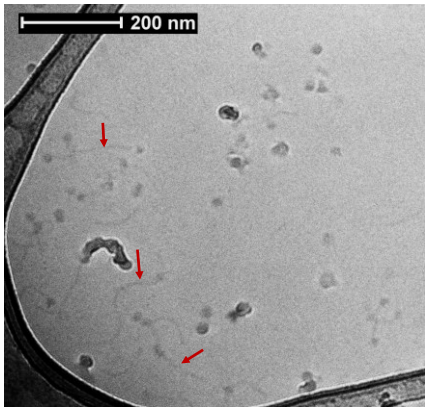

Figure 5.17. Cryo-TEM of RBL-loaded nanoparticles (15 w/w_p %) showing the coexistence of spherical and cylindrical morphologies (pointed by arrows).

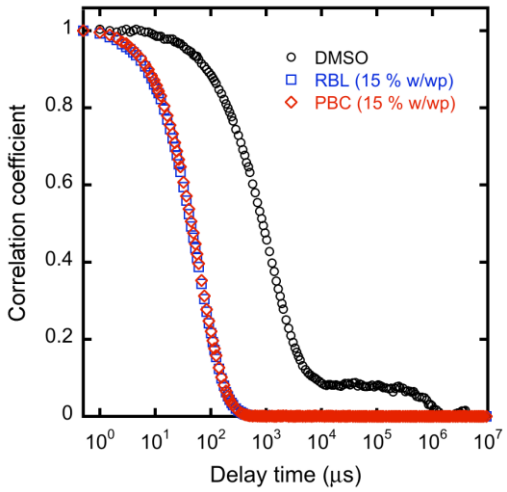

Figure 5.18. Correlation functions of the polymer in DMSO and of solute-loaded nanoparticles, as indicated.

5.3.4 Single-chain Nanoparticles Properties

DLS distributions of RBL and PBC nanoparticles are shown in Figure 5.19. In both cases, the average particle size remains constant (~ 40-45 nm) with relatively narrow polydispersities for low solute feeds (i.e., 5-20% w/w_p). Static light scattering results of 15% PBC nanoparticles yielded an aggregation number of ~ 1.5 which is within the range observed for the polymer in water, supporting unimolecular encapsulation. The similarity of PBC and RBL particles within this range suggests that unimolecular encapsulation occurs in both cases. Furthermore, encapsulation was found to be insensitive to initial polymer concentration within this range, as a ten-fold decrease in polymer concentration (prior to mixing) resulted in particles with the same size distributions (Figure 5.20). This is important in that concentration is known to dramatically influence intra- vs. intermolecular chain association. Loading capacity and efficiency of RBL and PBC were also measured within this range and were found to be high, with little influence of the type of solute on either parameter (Table 5.3).

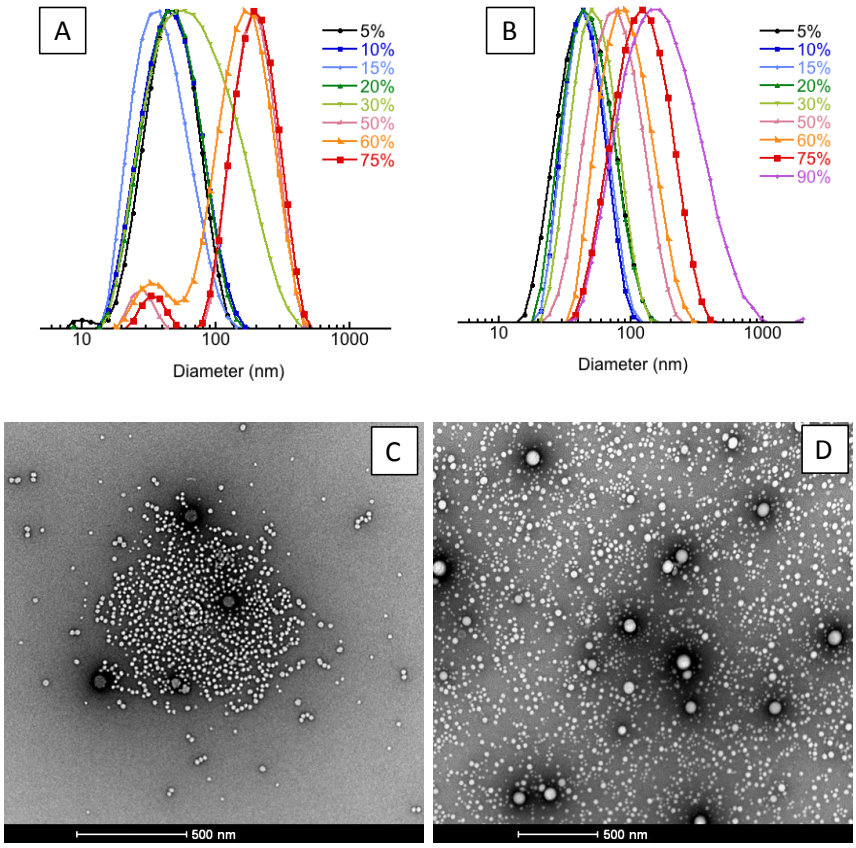

Figure 5.19. Size distributions and TEM images of RBL- and PBC- nanoparticles (A/C and B/D, respectively). Particle size was surveyed over a broad range of solute concentrations (5 - 75 % $w/w_{polymer}$), as indicated. Micrographs correspond to samples prepared with 50 % w/w_p (RBL) and 75 % w/w_p (PBC).

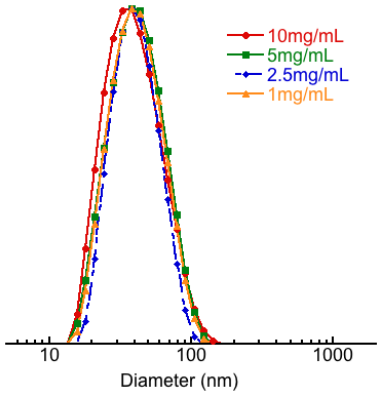

Figure 5.20. DLS size distributions of RBL-nanoparticles (15 w/w_p %) prepared with different initial concentrations of $PGMA_{721}$-*g*-PEG_{45}/PLA_{15} in THF, as indicated.

Table 5.3. Loading capacity and efficiency of RBL and PBC nanoparticles. Initial polymer concentration was 10 mg/mL in THF.

solute feed (w/w_p, %)	rose bengal lactone		probucol	
	LC (%)	*LE (%)*	*LC (%)*	*LE (%)*
5	3.8	74.4	3.8	75.8
10	9.5	79.6	6.8	81.8
15	12	89.9	12.9	89
20	17.1	80.5	12.8	72.3

The above observations support single-chain encapsulation of RBL and PBC by the brush polymer through hydrophobic host-guest interactions. Unlike previously reported examples of single-chain nanoparticles, the collapse of the brush amphiphile into spherical unimolecular nanoparticles is induced by the presence of an external hydrophobic component. Supersaturation, or the ratio of solute concentration to its solubility limit, is expected to be low under these conditions, so it is likely that heterogeneous nucleation is the preferred mechanism. In this sense, the high local concentration of PLA chains along the brush can provide a rich environment for nucleation to occur, leading to micellar compaction. Hence, the invariability of particle size to solute type or polymer concentration within this the range, appears to reflect a limit for solute solubilization in unimolecular micelles.

As solute feed increases (30-75%), differences among solutes become evident. For instance, RBL particles develop a bimodal distribution, the smaller peak of which falls within the range of unimolecular loaded micelles. Larger aggregates are also formed, indicating that the polymer is unable to affect unimolecular encapsulation, thus relying on intermolecular association to minimize the energy of the system. Interestingly, as evidenced by TEM, these larger aggregates appear to be formed by clusters of smaller particles as they exhibit a particularly rough surface. In contrast,

PBC particles show a gradual increase in size with solute concentration. This trend, which has been observed previously for solute encapsulation with linear diblock copolymers, suggests that nucleation and growth precede polymer adsorption and stabilization. Micrographs of loaded PBC particles in the high solute range show broader size distributions than for RBL and the larger aggregates do not appear to have the same surface roughness as aggregates from RBL. Ultimately, differences among RBL or PBC nanoparticles in the high solute range appear to reflect differences in solute-polymer interaction, determined by their physicochemical properties.

5.3. Conclusion

In this chapter, we discussed amphiphilic brush copolymers as single-molecule stabilizers of hydrophobic solutes. A densely PEG/PLA side-chain grafted brush copolymer with worm-like chain conformation was examined. The extended unimolecular structure of the brush was preserved after undergoing a rapid change in solvent quality, attributed to the steric effect offered by its high PEG grafting density. This macromolecular brush demonstrated its capability as an effective stabilizer of hydrophobic solutes. Notably, spherical single-chain nanoparticles were formed in the cases of low solute feeds, as a result of host-guest hydrophobic interactions. This intramolecular association, triggered by external hydrophobic compounds, is relatively insensitive to polymer concentrations, as compared to previously reported single-chain nanoparticle systems. On the other hand, higher solute encapsulation resulted in multimolecular nanoparticles, wherein the particle size and properties were largely dependent on physicochemical properties of encapsulated solutes.

Chapter VI: Enhanced Stability of Unimolecular Nanocarriers from Amphiphilic Brush Copolymers

6.1 Introduction

Micelles systems formed by the self-assembly of amphiphilic block copolymers have been widely studied as carriers for drug delivery. In an aqueous milieu, hydrophobic blocks of copolymers collapse and form the micelle core while hydrophilic blocks form the corona of the micelle, serving as the stabilizing layer.[22,33,34] This feature is especially useful for delivering hydrophobic drugs, since the limitation of poor solubility could be resolved by physical entrapment of the agents inside the hydrophobic micelle core, allowing their transport at concentrations that are much higher than their intrinsic water solubility.[35,189] The prolonged circulation time as well as the size of the particles (10-100nm) in polymeric micelle systems allow their gradual accumulation in regions with leaky vasculature, such as tumors or inflammation sites, providing a 'passive' targeting strategy, known as the enhanced permeability and retention effect (EPR).[6,34,35] As a result, micelle systems are poised to greatly improve the bioavailability of hydrophobic drugs.[6,34]

Drug retention inside these carriers depends on micellar stability and interactions between the drug and the stabilizer.[34] A important number of contributions have focused on improving micellar stability.[13,18,34] Physical stability is a vital parameter in determining how well a micellar drug delivery system can maintain integrity without dissociation under physiological conditions.[34,190] In vivo, protein-particle interaction

may interfere with the micelles.[34] Also, surface opsonization of blood proteins will induce the uptake of foreign objects by phagocytic macrophages, resulting in RES clearance.[33,34] In this sense, surface properties of the micelles, such as degree of hydrophilicity and steric stability have strong influence on the biodistribution of drug encapsulating micelles.[33,191] In polymeric micelle systems, poly(ethylene glycol) (PEG) is widely employed as the hydrophilic component, forming the corona of micelles. [6,33-35] The efficacy of PEG steric stabilization is dependent on its surface density and thickness,[33] and may slow down opsonization and enhance micellar stability.[6,12,14,191,192]

Recent advances in polymerization techniques have enabled us to synthesize macromolecules with increasingly complex architectures, such as molecular brush copolymers, wherein graft length exceeds graft spacing. Molecular brushes are a group of graft polymers that resemble the brush-like structure in glycoproteins.[43] The intramolecular excluded volume interactions among densely grafted side chains results in a shape-persistent conformation of the brush.[50,176] Micelles could be generated from amphiphilic molecular brushes undergoing solution self-assembly, and similar with their linear analogs, assembled structures are adaptable via altering the molecular characters of amphiphiles.[57,105,193] Micelles from brush amphiphiles exhibit advantageous properties in drug delivery applications, such as high solution stability,[74,194] and high loading capability.[194] More interesting, excluded interactions among crowded branches induce a lower level of intermolecular entanglement in assembled structures,[57] resulting in low aggregation numbers of polymer chains within brush amphiphiles micelles.[194,195] In particular cases, unimolecular micelles

have been obtained from the self-assembly of molecular brushes.[136,196-198] Compared with traditional micelles, unimolecular micelles possess higher stability against dissociation under condition of high dilution such as injection into bloodstream, and they have been developed as more stable delivery vehicles for therapeutic molecules.[9,10] In the previous Chapter, unimolecular micelles were obtained from $PGMA_{721}$-*g*-(PEG_{45}/PLA_{15}), an amphiphilic brush copolymer composed of a poly(glycidyl methacrylate) (PGMA) backbone bearing poly(ethylene glycol) (PEG) and poly (D, L-lactide) side chains. The brush amphiphile showed excellent solute stabilization capability, and the resulting loaded structures could preserve their unimolecular character until solute feeds of ~ 20 % wt.

In this Chapter, we further examined the physicochemical properties of unimolecular micelles from brush amphiphiles, and explored their potential as drug carriers. Aside from the previously discussed brush amphiphile $PGMA_{721}$-*g*-(PEG_{45}/PLA_{15}), we synthesized another copolymer with longer PEG segments ($PGMA_{721}$-*g*-(PEG_{113}/PLA_{11})). In addition, the amphiphilic linear block copolymer PEG_{113}-*b*-PLA_{34} was also used as a comparison in this study. First, we will discuss the properties and morphologies of micelles prepared from both amphiphiles. Then, we will examine loaded nanoparticle stability by interaction with human serum albumin. Solute-loaded particles were prepared by a rapid mixing method using rose bengal lactone (RBL). Cylindrical or spherical structures were found in loaded unimolecular micelles, dictated by the hydrophilic side chain length. Nanoparticle-protein stability was then evaluated, as was the drug release profile.

6.2 Materials and Method

6.2.1 Materials and Characterization

All reagents were commercially available and used as received unless otherwise noted. Glycidyl methacrylate (GMA, Aldrich 97%) was passed through a short basic alumina column to remove initiator. 2,2′-Azobis(2-methylpropionitrile) (AIBN) and D,L- lactide were recrystallized from methanol and anhydrous ethyl acetate respectively. 1,8-Diazabicyclo[5.4.0]undec-7-ene (DBU) was kept over molecular sieves (3 Å) overnight. Deionized water was purified in a Barnstead Nanopure system to a final resistance of 18.2 mΩ; it will be referred to as Nanopure water.

Gel Permeation Chromatography (GPC) was performed on a Waters 1515 Isocratic HPLC equipped with three Styragel® columns (HR4, HR3, 300 mm x 7.8 mm) connected in series, a differential refractive index detector (Waters 2414) and a UV-visible detector (Waters 2489). HPLC grade THF was used as the eluent, at a flow rate of 1 mL/min. Molecular weights are reported referenced to polystyrene standards (Shodex SL-105). ^{1}H NMR spectra of polymers were recorded on a Bruker AV 400 MHz spectrometer in either $CDCl_3$ or DMSO-d_6, ^{1}H NMR spectra of micelles were recorded in either D_2O or a mixture of D_2O and Acetone-d_6. Spectra were referenced to $CHCl_3$ (7.26 ppm) or DMSO-d_6 (2.50 ppm). Diffusion ordered spectroscopy (DOSY) were performed on a Bruker AV 400 MHz spectrometer, equipped with a 5 mm PABBO-BB ^{1}H probe. Dynamic Light Scattering was conducted on a Malvern Instruments Nano-ZS ZetaSizer equipped with a 4 mW He-Ne laser operating at 633 nm. All measurements were performed at 25 °C at a scattering angle of 173°.

Fluorescence spectroscopy was carried out on a Fluorolog-3 system (HORIBA Jobin Yvon Inc., NJ). Bright-field TEM imaging was performed on a FEI Technai 12 Twin Transmission Electron Microscope operated at an acceleration voltage of 100 kV. All TEM images were recorded by a SIS Megaview III wide-angle CCD camera. TEM grids (carbon-coated copper or formvar-carbon grid, Electron Microscopy, Hatfield, PA) were ionized under plasma before preparation. Grids were placed on top of a single drop of sample suspension (20 μL) for 5 minutes, washed with 5 drops of doubly distilled water and placed onto a drop of 2 wt% aqueous uranyl acetate solution for 30s. Excess solution was blotted off with filter paper and samples were allowed to dry at room temperature prior to imaging.

6.2.2 Polymer Synthesis

B1. *$PGMA_{721}$-g-(PEG_{45}/PLA_{15})*

The synthesis of molecular brush copolymer **B1** was discussed in section 5.2.2 of the previous chapter.

B2. *$PGMA_{721}$-g-(PEG_{113}/PLA_{11})*

(i) $PGMA_{721}$ & $PGMA_{721}$-g-N_3

$PGMA_{721}$ backbone synthesis and azidolysis were discussed in section 5.2.2.

(ii) $PGMA_{721}$-g-PLA_{11}

$PGMA_{721}$-g-N_3 (150 mg, 0.81 mmol –OH group) and D,L-lactide (1.1685 g, 8.11 mmol) were loaded into a round bottom flask, and placed under high vacuum at 36 ^{o}C

for ~ 5 hours. After backfilling with argon, anhydrous DMF (~ 35 mL) was added to dissolve the reagents. DBU (45.6 μL, 0.31 mmol) was then injected and the reaction was allowed to proceed for 1.5 h under argon at room temperature. Polymerization was quenched by addition of benzoic acid (93.4 mg, 0.76 mmol). DMF was removed under vacuum and the polymer was re-dissolved in THF, followed by precipitation into a mixture of Nanopure water and methanol (1:1, vol). Solids were lyophilized to remove water. Yield: 86.5 %. ^{1}H NMR of the resulting grafted polymer is shown in Figure 6.1. The degree of polymerization of PLA side chains was calculated based on signals e and e'.

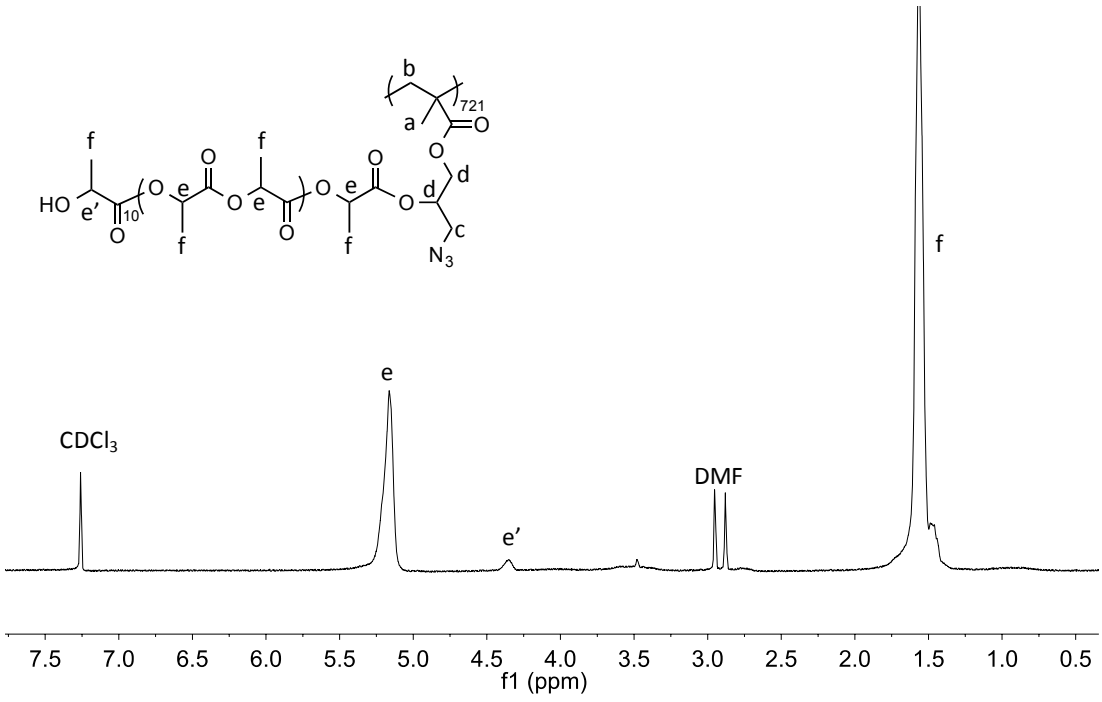

Figure 6.1. ^{1}H NMR and peak assignments of PGMA$_{721}$-*g*-PLA$_{11}$.

(ii) Alkynyl-terminated PEG

mPEG$_{113}$ (12.7807 g, 2.56 mmol) was transferred to a round bottom flask and placed

under high vacuum for around 5 h. The flask was backfilled with nitrogen prior to the addition of 5-hexynoic acid (338.5 μL, 3.07 mmol) and 4-(Dimethylamino) pyridine (DMAP) (0.128 g, 1.05 mmol), and purged with nitrogen for 30 minutes. Anhydrous dichloromethane (DCM, 20 mL) was added and the reagents were allowed to dissolve. Then, a solution of N,N'-dicyclohexylcarbodiimide (DCC) (1.055 g, 5.11 mmol) in anhydrous DCM (5 mL) was added to the reaction mixture dropwise, and the reaction was carried out overnight at room temperature The solution was filtered and concentrated by rotary evaporation; the product was recovered by precipitating this solution into cold diethyl ether and dried under vacuum. ^{1}H NMR of the product is shown in Figure 6.2 and indicates quantitative conversion.

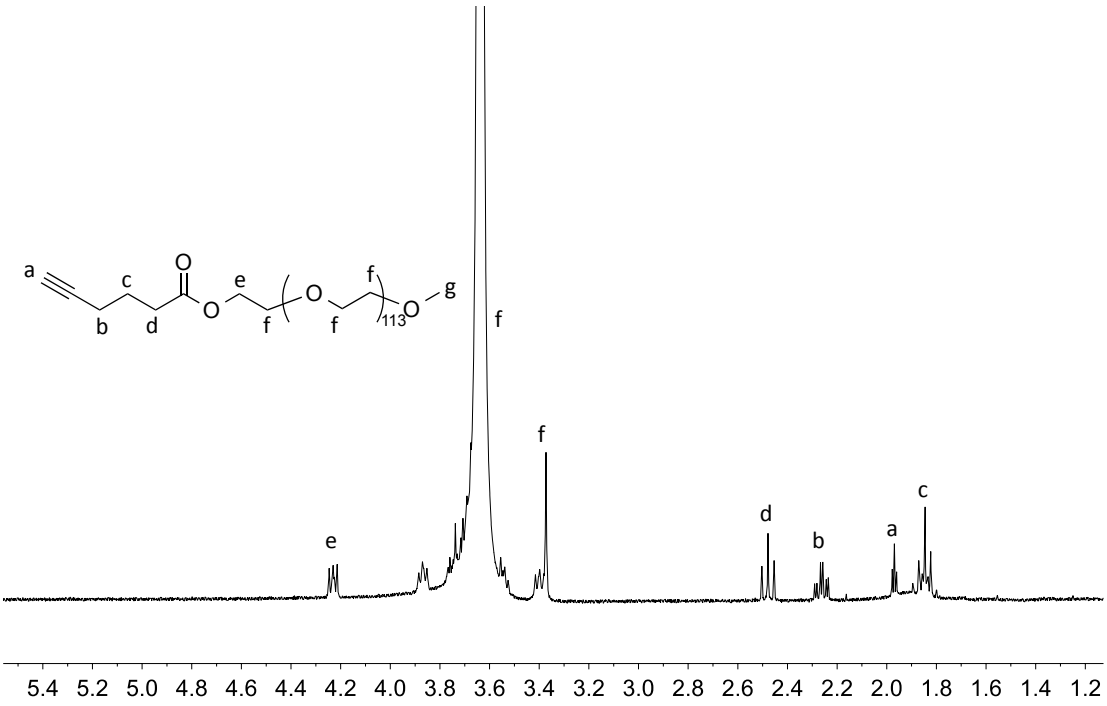

Figure 6.2. ^{1}H NMR and peak assignments of Alkynyl-terminated PEG.

(iii) PGMA$_{721}$-g-(PEG$_{113}$/PLA$_{11}$)

Alkynl-PEG was grafted onto PGMA$_{721}$-g-PLA$_{17}$ via *'click'* reaction, catalyzed by $CuSO_4 \cdot 5H_2O$/ascorbic acid. Molar ratio of $-N_3$, alkynyl groups, $CuSO_4 \cdot 5H_2O$ and ascorbic acid was kept at 1:1.05:0.2:1. PGMA$_{721}$-g-PLA$_{11}$ (200 mg, 0.11 mmol) was and alkynyl-PEG$_{113}$ (617.1 mg, 0.12 mmol) were placed in a round bottomed flask and dissolved in DMF (16 mL). Ascorbic acid (19.9 mg, 0.11 mmol) was added and the solution was bubbled with argon for 30 min. Finally, $CuSO_4 \cdot 5H_2O$ (5.5 mg, 0.02 mmol) was added under argon and the reaction was allowed to take place at room temperature for 12 h under argon. The product was purified by precipitation in diethyl ether and dried in vacuum oven. Yield: 96.1%. ^{1}H NMR spectrum of the polymer is shown in Figure 6.3.

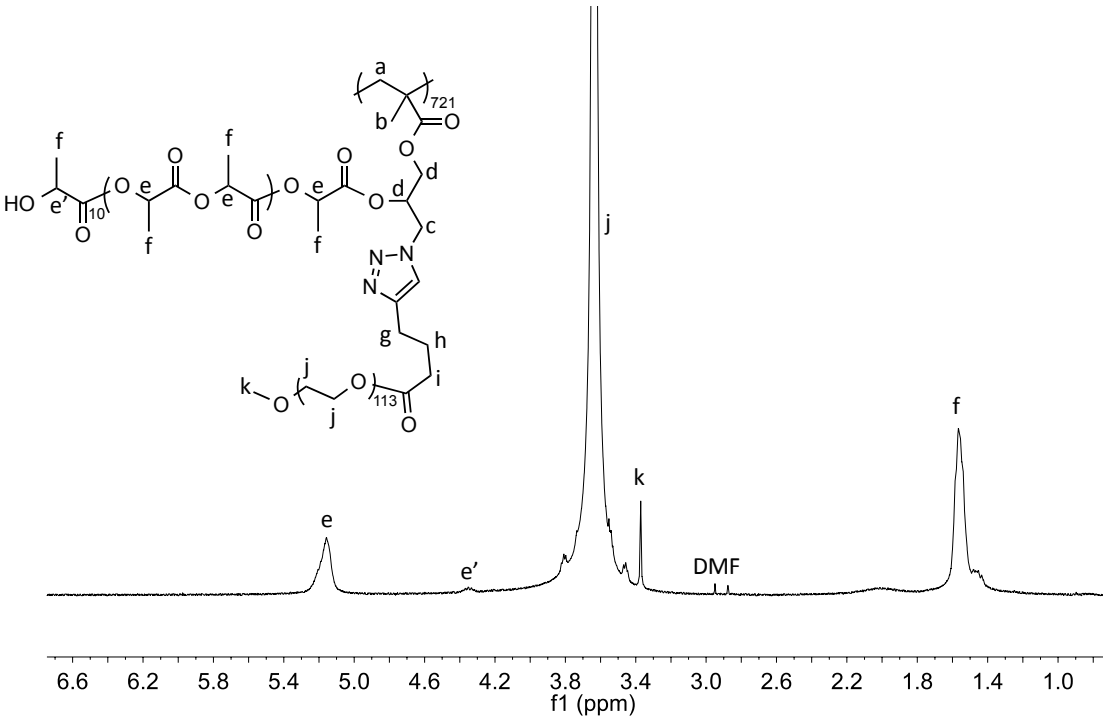

Figure 6.3. ^{1}H NMR and peak assignments of PGMA$_{721}$-*g*-(PEG$_{113}$/PLA$_{11}$).

L1. *PEG$_{113}$-b-PLA$_{34}$*

mPEG$_{113}$ (750 mg, 0.15 mmol) was loaded into a round bottom flask, and placed under high vacuum at 90 °C for ~1 h. After cooling and backfilling with argon, D,L-lactide (750 mg, 5.2 mmol) was added to the flask and placed under high vacuum at 36 °C for ~3 h. After backfilling with argon, 8 mL anhydrous dichloromethane was added to dissolve all reagents. DBU (8 µL, 0.05 ml) was then injected and the reaction was allowed to proceed for 1 h under argon at room temperature. Polymerization was quenched by addition of benzoic acid (15 mg, 0.12 mmol), followed by precipitation into 2-propanol. Resulting ^{1}H NMR spectra and chromatograms are given in Figures 6.4 and Figure 6.5, respectively

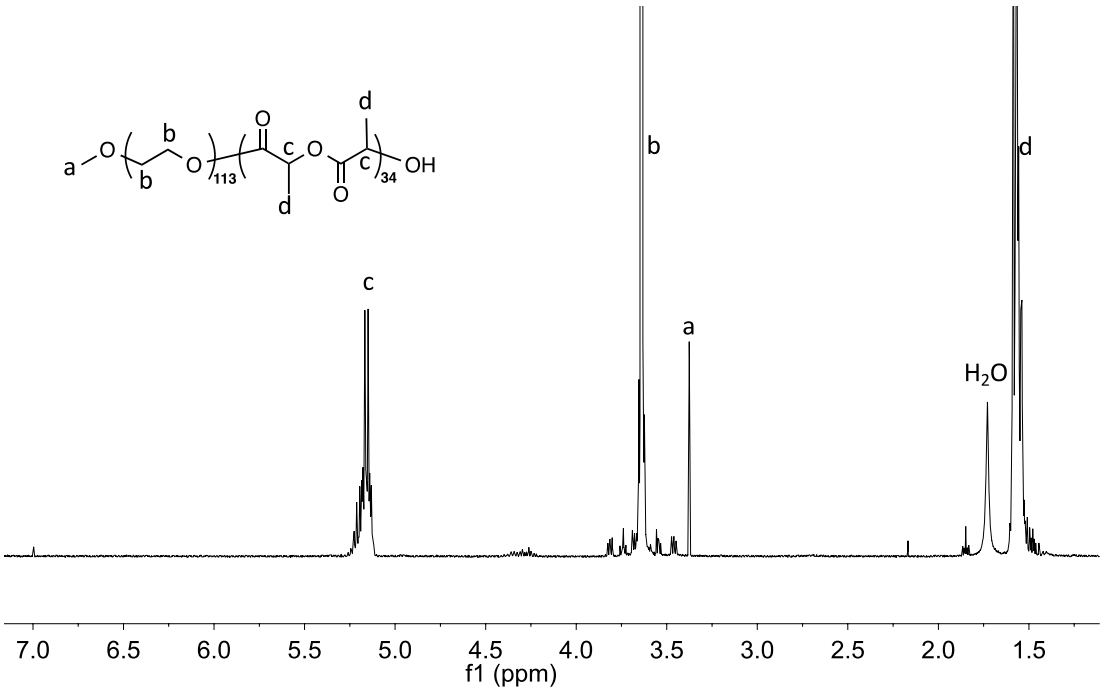

Figure 6.4. ^{1}H NMR and peak assignments of PEG$_{113}$-*b*-PLA$_{34}$.

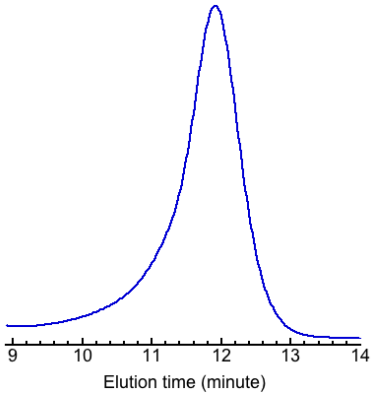

Figure 6.5. Gel permeation chromatogram of PEG_{113}-*b*-PLA_{34}.

6.2.3 Differential Refraction index (dn/dc) Measurement

The change in refractive index with concentration (dn/dc) was measured by an Optilab-rEX refractive index detector (Wyatt Technology) using a laser light wavelength of 658 nm. The temperature was set at 25 °C for throughout the measurement. Samples were passed through 0.45 μm PVDF syringe filters (Thermo Scientific) and injected via the syringe pump (New Era Pump System, NE-1000) at a fixed velocity of 0.2 mL/min. Six concentrations were surveyed for the polymer in dimethylformamide (anhydrous), ranging from 0.1 to 2 mg/mL. Seven samples were surveyed for nanoparticles suspensions in Nanopure water, ranging from 0.02 to 0.2 mg/. (dn/dc) values were analyzed by the Astra 6.1 software.

6.2.4. Static Light Scattering Measurement

SLS Measurements were performed with a DAWN HELEOS II (Wyatt Technology) with a 120mW GaAs linearly poloarized laser operated at 658 nm. Filtered samples (described above for refractive index measurements) were injected at a fixed velocity

of 0.2 mL/min. Polystyrene (20 kDa, Fluka; 5 mg/mL solution in DMF) and dextran (9-11 kDa, Aldrich, 5 mg/mL solution in Nanopure water) was used as standards to normalize measurements for polymer and micelles respectively. (dn/dc) values were used to determine absolute molecular weights, and the weight average molecular weight (M_w) was extracted from Zimm plots using Debye and Zimm models (for the polymer and micelles, respectively) using Astra 6.1.

6.2.5 Determine Critical Micelle Concentration C_{CMC}

The critical micelle concentration (C_{CMC}) of polymer was measured by using pyrene as a probe. For this, 50 μL Pyrene solution in acetone ($6x10^{-5}$ M) was loaded into a 5mL clean scintillation vial and left open under the hood to allow for complete evaporation of the solvent. Then, 50 μL of polymer solution (0.001 to 2 mg/mL in acetone) were added to each of 10 vials containing pyrene, followed by 1mL of water. Final polymer concentration ranged from 50 μg/ml to 0.1 mg/mL. Samples were vigorously stirred with a vortex mixer (~ 1 min), and left to shake gently overnight to evaporate acetone. Excitation and emission spectrum were recorded by fluorescence spectroscopy. Pyrene excitation was scanned from 300 to 360 nm at an emission wavelength of 390 nm. Excitation and emission bandwidths were set at 2 nm. The intensity ratio from signals at 336 and 334 nm (I_{336}/I_{334}) was analyzed as a function of polymer concentration. C_{CMC} values were read from the intersection between curve tangents at low and high concentrations.

6.2.6. Diffusion-ordered NMR Spectroscopy (DOSY) Measurement

Polymer solutions of 5 mg/mL were prepared in $CDCl_3$. To avoid convection effects resulting from sample heating during gradient pulses, the temperature was maintained at 17 ± 0.2°C. DOSY spectra were acquired with the ledbpgp2s pulse program. Gradient strength was linearly incremented in 32 steps from 5% to 80% of its maximum value. Diffusion time and gradient pulse lengths were set to 75 ms and 2 ms, respectively. The diffusion dimension of the 2D DOSY spectra was processed with a Bruker topsin software (v. 2.1).

6.2.7. Polymer Self-assembly

The polymer was dissolved in THF at concentrations ranging from 1 to 20 mg/mL. Rapid self-assembly was carried out in a four-inlet vortex mixer described elsewhere.[28] Nanopure water was charged into three 50 mL syringes (Hamilton, NJ) and the organic solution into a 10 mL syringe, and mounted on two separate syringe drivers (PHD Ultra, Harvard Apparatus). Flow rates of water and organic streams were 108 mL/min (water) and 12 mL/min (THF) to achieve a 10% (v/v) THF concentration. Samples were collected and dialyzed (6-8 kDa MWCO, Fisherbrand) against Nanopure water for 24 h at 20 °C. Water was replenished every 4 h throughout the dialysis process. Samples were stored in clean scintillation vials, and unless otherwise noted, kept under refrigeration at 4 °C.

6.2.8 Flash Nanoprecipitation

The protocol described above was used to prepare solute loaded nanoparticles, with

the exception that both the polymer and the solute (rose bengal lactone, RBL) were dissolved together in tetrahydrofuran. Dialyzed samples were collected and filtered through 0.45 μm PVDF syringe filters (Thermo Scientific) and stored in clean centrifuge tubes (Falcon® Tube). Loading capacity (LC) and efficiency (LE) in nanoparticles (NP) are estimated as:

$$Loading\ capacity\ (LC,\%) = \frac{Mass\ of\ solute\ in\ NP}{Mass\ of\ NP} \times 100$$

$$Loading\ efficiency\ (LE,\%) = \frac{Mass\ of\ solute\ in\ NP}{Mass\ of\ solute\ in\ feed} \times 100$$

LC and LE were determined by a Varian Cary 50 UV/Vis spectrophotometer (Agilent Technologies, Santa Clara, CA). Loaded micelles were lyophilized and dissolved in DMF. RBL concentrations were calculated from calibration curves in DMF, with reference to its absorption at 565 nm.

6.2.9 PEG Exposure in Micelles by NMR Studies

Micelles were concentrated ~100 times by centrifugation at 5000 g for 25 min (Allegra 64R, Beckman Coulter) through an Amicon Ultra centrifugal filter (10 kDa MWCO). Concentrated micelle suspensions were then transferred to an Eppendorf tube, and to it were added 600 mL D_2O and 3 μL methanol (external reference). Samples were vortexed for 1 min before analyzed by ^1H NMR (Bruker AV 400 MHz). From these solutions, 300 mL were then transferred back to clean Eppendorf tubes, mixed with acetone-d_6 (1 mL), and sonicated for 10 min. The samples were allowed to fully dissolve over 4 h at room temperature and sonicated again for 10 min prior to analysis.

6.2.10 Components Mobility Measurement

Polymers (10 mg) were dissolved in acetone-d_6 (600 μL to 120 μL) in Eppendorf tubes. Then, D_2O (0 μL to 480 μL) was added to each of the tubes containing polymer solution, resulting in 600 μL final solution of 16.7 mg/mL polymer in cosolvent mixtures. The percentage of D_2O in cosolvent mixtures ranged from 0% to 80%. ^1H NMR (Bruker AV 400 MHz) spectra were acquired, and the full width at half maximum (in Hertz) of PLA (methine, CH) and PEG (methylene, CH_2) signals were analyzed.

6.2.11 Nanoparticle Stability Studies

Nanoparticles (0.7mg/mL) were incubated with human serum albumin (HSA, 2 mg/mL) in phosphate buffer solution (Dulbecco's phosphate buffered saline, pH 7.4) at 37 ^oC. Particle size was monitored by dynamic light scattering at different intervals (0, 2, 4, 8 and 24 h).

6.2.12 RBL Release Study

3 mL of RBL loaded nanoparticles were transferred in to a dialysis cassette (Slide-A-Lyzer®, Thermo Scientific, 3.5 kDa MWCO). The dialysis cassette was then immersed in a beaker containing 150 mL of PBS solution. The system was kept at 37 ^oC under mild stirring. At selected intervals (1, 2, 4, 8, 12, and 24 h), 5 mL of PBS solution in the beaker was taken out, and it was replaced with the same amount of fresh PBS to maintain the sink volume constant. The released medium was lyophilized and the resulting powder was re-suspended in 2 mL dimethylformamide.

The concentration of RBL was determined by a Varian Cary 50 UV/Vis spectrophotometer (Agilent Technologies, Santa Clara, CA), calculated according to the empirical equation of pure RBL in dimethylformamide, referring to the absorbance at 565 nm.

6.3 Results and discussion

6.3.1 Amphiphile Properties

Structures of molecular brush copolymers **B1** and **B2**, and linear copolymer **L1** are provided in Figure 6.6, and their molecular characteristics have been summarized in Table 6.1. Prior to assembly, amphiphile properties including critical micelle concentration (CMC), and their diffusion coefficient in an organic solvent were examined, as shown in Table 6.2.

Critical micelle concentration (CMC) is the amphiphile concentration above which micelles start to form[6,18,33]. C_{CMC} is related with the hydrophobicity of the copolymer, wherein a longer hydrophobic block could promote the cohesion of the core, lowering its CMC value, and it is a fundamental parameter that characterizes thermodynamic stability of micelle.[18] Low C_{CMC} value was found in linear amphiphile **L1**, indicating its high stability against dissociation upon dilution.[18,33] However, unimolecular do not exhibit a clear CMC, since it is composing of a single polymer chain.[199] Instead, critical water content (CWC), defined as the water content at which hydrophobic blocks of copolymers begin to associate,[14,200,201] may better represent the onset of unimolecular micelle formation. Thereby, the onset of hydrophobic association in

different types of amphiphiles, as well as their micellar stability, is discussed and compared in terms of the reduction of their hydrophobic chain mobility in response of water addition, provided in section 6.3.3.

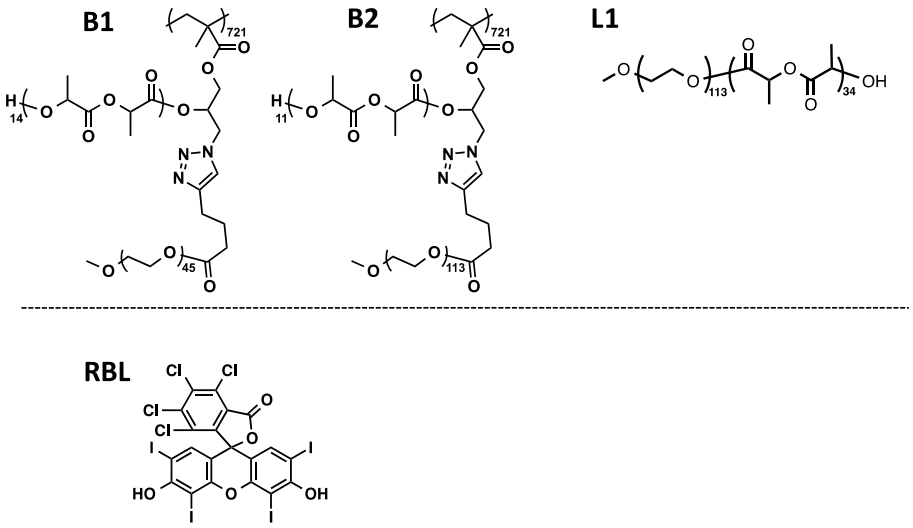

Figure 6.6. Molecular structures of brush amphiphile **B1**, **B2**, and linear amphiphile **L1**, and hydrophobic solute Rose Bengal lactone (RBL).

Table 6.1. Characteristics of amphiphiles used in the study.

	Polymer	M_n [a] (kg/mol)	M_w [b,c] (kg/mol)	$Đ$ [c,d]	R_g [d] (nm)	w_{PEG} [a] (% *w*t)
B1	$PGMA_{721}$-*g*-(PEG_{45}/PLA_{15})	3,110	4,470	1.43[c]	40.2	45.7
B2	$PGMA_{721}$-*g*-(PEG_{113}/PLA_{11})	4,952	-	-	-	72.8
L1	PEG_{113}-*b*-PLA_{34}	9.9	13.2	1.08[d]	-	50.5

[a]Determined from ^{1}H NMR spectra. [b]Measured by gel permeation chromatography. [c]Estimated by M_w(SLS)/M_n(^{1}H NMR). [d]Determined by static light scattering in dimethylformamide.

Table 6.2. Micellar properties of amphiphiles.

	CMC[a] (10^{-3} mg/mL)	Diffusion Coefficient[b] (10^{-10} m^2/s)	PEG exposure%[c]
B1	-	5.70	87.8%
B2	-	5.67	95.3%
L1	2.86	5.77	86.1%

[a]Determined by fluorescence spectroscopy. [b]Measured diffusion-ordered NMR spectroscopy. [c]Calculated from ^{1}H NMR measurement of PEG proton signal of micelles in D_2O versus in $CDCl_3$.

6.3.2 Amphiphile Self-assembly

Empty micelles from amphiphiles were prepared by a rapid mixing method, wherein their self-assembly was triggered by a rapid change in solvent quality from 100% THF to 90% water/10% THF (v/v) inside a multi-inlet vortex mixer (MIVM). Assembled structure morphologies were recorded by transmission electron microscopy, as shown in Figure 6.7. A cylindrical structure had been discovered for **B1** due to the steric hindrance among hydrophilic side chains, as discussed in the previous chapter. A further increase in PEG side-chain length results in the different morphologies shown for **B2**. Numerous features, including cylindrical, spherical, and pearl-necklace-like structures were observed by TEM, as demonstrated in Figure 6.7 (B). We suspect that TEM might not be the best representation of the intact morphology of brush micelles, since both staining and drying in TEM sample preparation may result in structural alterations of colloids,[183] as discussed in Chapter V. Accordingly, the morphology of **B2** will be characterized more exhaustively by a combination of cryo-TEM and small angle scattering techniques in the future. On the other hand, spherical nanoparticles were formed from the self-assembly of **L1**, which is consistent with results from prior literature on the linear PEG/PLA system undergoing rapid self-assembly.[20] Nevertheless, the polydispersity of **L1**

nanoparticles was not narrow (0.21), as demonstrated by dynamic light size (Figure 6.7C). The imperfect **L1** nanoparticles are likely related with the short PLA block, which leads to a less compact nanoparticle core,[14] susceptible to inter-particle aggregation. Micelles from **B1** were discovered to be unimolecular, determined by static light scattering, as discussed in Chapter V. Similarly, the aggregation number of polymer chains in micelles from **L1** was calculated by comparing the apparent molecular weight of micelles (2.7×10^6 Da) with number average molecular weight of **L1** (9.9×10^3 Da) calculated from NMR analysis, resulting in an aggregation number of 273.

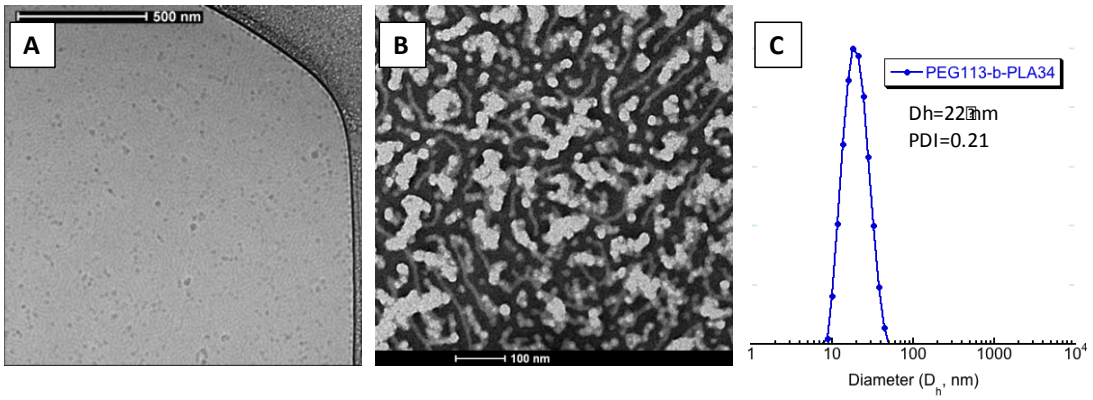

Figure 6.7. Transmission electron micrographs of unloaded aggregate structures from amphiphile **B1** (A) and **B2** (B). (A**)** was conducted under cryogenic condition, whereas (B**)** is recorded by regular TEM. (C) Dynamic light scattering distribution of unloaded nanoparticles from amphiphile **L1**

Self-assembly aggregates are stabilized by hydrophilic PEG contents that are exposed into the aqueous surroundings. Both surface density and thickness of PEG shell dictates the efficacy of the PEG stabilization corona, preventing the unwanted exposure of hydrophobic core components in the aqueous medium.[33] PLA and PEG

exhibit similar solubility parameters, resulting in high compatibility between them. Consequently, it is possibly for a fraction of PEG chains to be buried inside PLA core, leading to insufficient PEG coverage.[41] To examine the PEG surface coverage of the three micellar samples, we conducted an NMR study to determine the ratio of PEG contents that are effectively exposed on the surfaces of micelles. This was based on comparing proton integration signals of PEG on the micelle surface (in D_2O) with respect to the total amount of PEG (in acetone-d_6), using methanol as an external standard. High PEG exposure ratios (> 86%) were found in all samples, as given in Table 6.2, meanwhile PLA signals were absent in micelles, indicating PEG effectively served as steric stabilizer for all.

6.3.3 Mobility of Hydrophobic Compartments in Cosolvent Mixtures

The kinetics of amphiphile self-assembly mainly relies on the hydrodynamic interactions among the aggregates and the chain mobility in the core.[202] Also, the hydrophobic chain mobility provide insights into the critical water content (CWC) of the copolymers - during the micellization process, as the depletion of good solvent from the micelle core, the onset of the associations among hydrophobic compartments is characterized by the reduction in their mobility.[14] For a better understanding of hydrophobic compartment mobility under different solvent quality, we estimated local mobility by NMR as the half width of the proton peak (in Hz). A broad peak represents more restricted local chain mobility.[203] Herein we compare amphiphiles **B1** and **L1**. First, amphiphiles were dissolved in acetone-d_6, a good solvent for both blocks, followed by addition of predetermined amounts of D_2O, a selectively poor solvent for PLA. Peak widths (in Hz) of PEG and PLA were analyzed by ^{1}H NMR

and plotted against the percentage of D_2O; the results are provided in Figure 6.8. In a good solvent (0 % D_2O), both PEG and PLA in **B1** exhibit lower mobility than in **L1**, reflected by their broader half width. The lower mobility of chains in **B1** is concomitant with its brush architecture, wherein PLA and PEG chain ends were connected through the brush backbone in **B1**, limiting their mobility. An increase in the percentage of D_2O resulted in a decrease of PLA chain mobility in both amphiphiles, corresponding to the decrease in solvent quality. The addition of D_2O has a negligible effect on the PEG peak width, since D_2O does not alter the solubility of PEG. For both amphiphiles, the decrease of PLA mobility exhibits two regions: initially, for lower percentages of D_2O, a mild decrease in PLA chain mobility was accompanied by the increase in D_2O percentage, whereas at higher content of D_2O, a rapid decrease in PLA mobility was observed. The two regions were separated by a breakpoint, wherein a sudden jump in PLA mobility occurred. The breakpoint positions are at ~ 40 % and ~ 50 % D_2O for **B1** and **L1**, respectively. The breakpoint suggests the onset of self-assembly, indicated by the rapid decrease in local mobility of PLA. In this sense, an earlier onset of micelle formation was observed in **B1**, triggered by a smaller amount of D_2O. It could be attributed to the aforementioned limited chain mobility, or the unimolecular character in brush amphiphile **B1**. The highest contents of D_2O examined were 65% and 75% for **B1** and **L1**, respectively, since further addition of D_2O will lead to the complete burial of PLA inside the micelle core, resulting in an absence of the PLA proton signal. The core material (PLA) was able to be completely shielded inside the corona with less poor solvent addition for **B1** micelles, suggesting a better stabilization effect offered by its PEG corona.

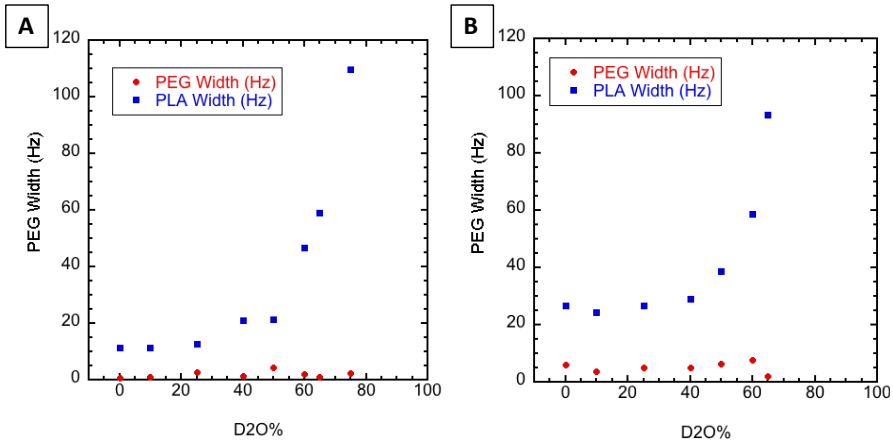

Figure 6.8. Effect of D_2O percentage on half width of ^1H NMR signals of (A) **B1** and (B) **L1** in acetone-d_6/D_2O (v/v) cosolvent mixtures at 25 °C.

6.3.4. Solute Stabilization

Rose Bengal lactone (RBL) was selected as the model solute in this study. We previously found that **B1** could effectively solubilize RBL, and preserve its unimolecular character with moderate solute incorporation. The cylindrical unimolecular micelles of **B1** collapsed into spheres upon solute loading, driven by the hydrophobic interaction between solute molecules and PLA branches. Here, in order to enrich the library of unimolecular brushes, we further examined solute stabilization properties of **B2**. RBL loaded nanoparticles from all three amphiphiles were prepared with the same condition, by the rapid change in solvent quality. The rapid mixing of non-solvent with solvent containing drug and stabilizing amphiphile generates high supersaturation and induces the rapid nucleation of solute particles, then, the adsorption of stabilizing amphiphile on solute particles quenches further solute aggregation and results in nanoparticles with controlled size.[204] The properties of the resulting nanoparticles depend on the competitive kinetics of polymer aggregation and solute nucleation and growth: rapid amphiphile assembly results in formation of

dead micelles without incorporation of organic solute, while rapid precipitation of solutes results in undesired larger particles.[205] The morphologies of loaded nanoparticles were examined by TEM, provided in Figure 6.9. Different from the collapsed spherical structure in **B1** sample, RBL loaded **B2** micelles preserved its cylindrical structure. We suspect higher level of excluded volume interactions are promoted by longer PEG branches in **B2**, resulting in extended backbone conformation.

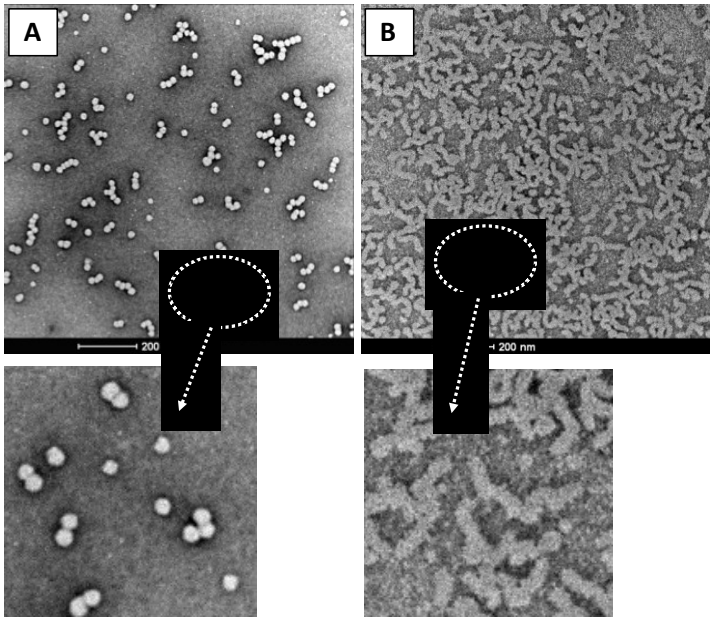

Figure 6.9. Transmission electron micrographs of RBL (15% w/w_p) loaded nanoparticles, prepared from **B1** (A), **B2** (B).

Drug loading capability (*LC*) and efficiency (*LE*) were evaluated for brush amphiphile **B1** and **B2**, as provided in Table 6.3. Flash nanoprecipitation is known to formulate nanoparticles with efficient entrapment of hydrophobic compounds,[41] as a result, high loading contents were obtained from both.

Table 6.3. *LC* and *LE* of RBL in nanoparticle prepared with amphiphile **B1** and **B2**.

Polymers	15% *w*/ w_p RBL	
	LC %	*LE*%
B1	12.0	89.9
B2	11.8	83.7

6.3.5.Nanoparticle Stability of Unimolecular Micelles

A previous study of nanoparticle stability in biologically relevant media reveals the superior colloidal stability of unimolecular brush amphiphile micelles in PBS, as well as their limited protein interaction, compared to its linear amphiphile counterparts.[20] Herein, we further investigate the in vitro stability of unimolecular loaded nanoparticles from brush amphiphile **B1,** in terms of their interactions with human serum albumin. Specifically, RBL loaded nanoparticles were incubated in PBS at 37 ^{o}C in the presence of human serum albumin (HSA), and their size distributions were monitored and taken as indicators of their stability. Nanoparticles prepared with RBL feeds ranging from 5 to 20% *w*/w_p were examined and compared.

Prior to protein adsorption, the colloidal stability of loaded nanoparticles in 1x PBS at 37^{o}C was examined. Nanoparticles in the buffered medium were prepared by dilution of nanoparticle aqueous solution directly with PBS (10x). Particle size was characterized immediately after addition of the buffer, and this refers to its size at time 0 (0 h). A small increase in average particle size (~ 4 - 6 nm) was observed upon switching the medium to PBS. As shown in Figure 6.10, the majority of nanoparticles were stable thereafter. A small deviation in particle size after 24 h was also found for 5 % RBL in which case it is possible that the small amount of solute might not provide sufficient compaction and therefore stabilization.

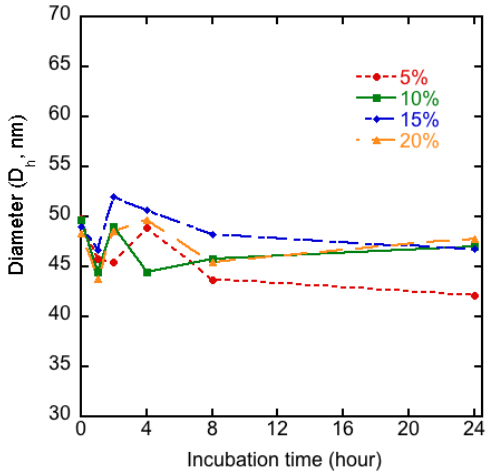

Figure 6.10. Average particle size of loaded nanoparticles of **B1** incubated in 1X PBS at 37 ^{o}C. Nanoparticles are prepared with different feeds of RBL, as indicated.

Knowing the stability of **B1** nanoparticles in PBS, we further examined their interaction with human serum albumin (HSA). All samples were prepared with a nanoparticle concentration of ~ 0.7 mg/mL, and an HSA concentration of ~ 2 mg/mL. The resulting mixtures were incubated at 37 ^{o}C for 24 h. Size distributions of nanoparticle-HSA mixture after 24 h incubation were compared with size distributions of original samples without adding HSA, and provided in Figure 6.11. In all batches, the mixture exhibits a bimodal distribution, with the small peak at ~ 7 nm corresponding to HSA, and the main peak at ~ 50 nm corresponding to loaded nanoparticles. Interestingly, it reveals no obvious change in size distributions after incubation with HSA, suggesting no apparent protein-nanoparticle interaction. Moreover, we analyzed intensity ratios between protein peaks and nanoparticle peaks (I_{HSA}/ I_{NP}). The ratios were acquired from samples immediately with HSA addition (0 h) and after incubation for 24 h, and are summarized in Table 6.4. For samples with 5 % - 15 % RBL, there is no apparent change in I_{HSA}/ I_{NP} ratio after 24 h, indicating no protein aggregation occurred. However, a slightly decrease of I_{HSA}/ I_{NP} was observed

in the sample with 20 % RBL, induced by the decrease in I_{HSA}. This drop of protein peak intensity is likely associated with protein aggregation, and as evidence, a small aggregation peak was identified in the size distribution of the mixture (Figure 6.11D).

Table 6.4. I_{HSA}/ I_{NP} of RBL loaded nanoparticles of **B1** at 0 h and 24 h of incubation with HSA.

RBL%	I_{HSA}/I_{NP} (0 h)	I_{HSA}/I_{NP} (24 h)
5	0.29	0.38
10	0.32	0.35
15	0.35	0.35
20	0.47	0.38

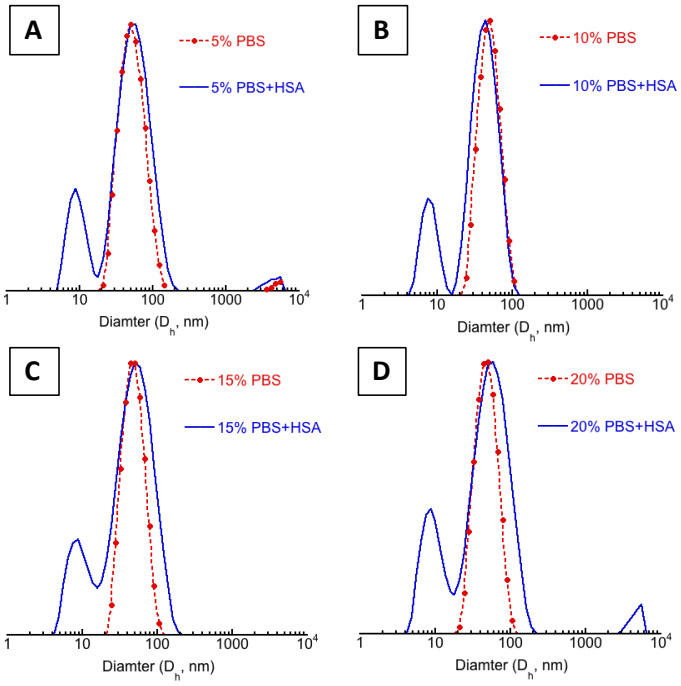

Figure 6.11. Size distributions of loaded nanoparticles of **B1** in the presence of human serum albumin (HSA) after 24 h incubation in PBS at 37 ºC (blue solid line). Distributions of nanoparticles in PBS are provided as references (red dotted line). **A-D** correspond to nanoparticles prepared with 5%, 10% 15% and 20% w/w_P of RBL, respectively.

The aggregation of nanoparticles is mediated by the PEG shell.[33] Generally, high

molecular weight PEG (> 2000 Da) results in stealth nanoparticles,[206] and effectiveness of PEG corona steric stabilization depending on both the surface density and the thickness of PEG shell.[6,33,35] Here, we suspect the excellent in vitro stability of loaded **B1** nanoparticles is associated with its densely grafted PEG branches, wherein PEG surface density is enhanced by the architecture of the amphiphile. Also, excluded volume interactions among crowed PEG chains might force them to adopt a more extended conformation, resulting in a thicker PEG surface layer on micelle surface.

6.3.6 Release Profiles

The release study of loaded nanoparticles of **B1** (15 % w/w_p RBL) was carried out in a simulated physiological condition in PBS (pH = 7.4) at 37 ^{o}C. The cumulative release profile of RBL in **B1** nanoparticles is given in Figure 6.12. Sustained release of RBL is achieved by **B1** nanoparticles, with no initial burst release.

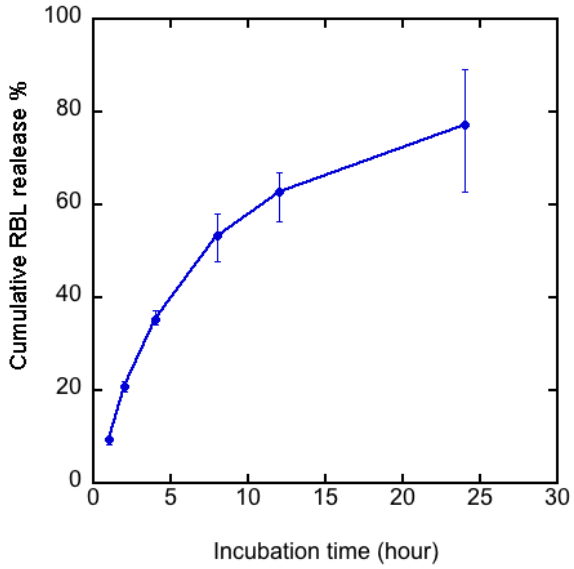

Figure 6.12. Cumulative drug release profiles of loaded nanoparticles of **B1** (15 % w/w_p RBL).

6.4 Conclusion

We examined the physicochemical properties of unloaded and loaded micelles of molecular brushes bearing poly(ethylene glycol) and poly(D,L-lactide) side chains. Rapid assembly of brush amphiphiles resulted in cylindrical unimolecular structures, different from the conventional spherical multi-molecular micelles obtained in rapid mixing process. The PEG exposure ratio on micelles surface was found to be higher in brush amphiphile micelles, compared to a linear amphiphile counterpart. In addition, the study of hydrophobic compartment mobility in amphiphiles further revealed an enhanced PEG steric stabilization effect in brush amphiphiles aggregates. Solute loading by Flash nanoprecipitation resulted in different loaded nanoparticle morphologies from brush amphiphiles, dictated by their hydrophilic side chain lengths. Stability of unimolecular loaded nanoparticles was examined by their interactions with human serum albumin. The results show excellent stability of

unimolecular loaded nanoparticles in biologically relevant media. Finally, drug release behaviors of loaded nanoparticles were studied, and no burst release was found in unimolecular micelles.

Bibliography

(1) Fahr, A.; Liu, X. *Expert Opin Drug Del* 2007, *4*, 403.

(2) Kawabata, Y.; Wada, K.; Nakatani, M.; Yamada, S.; Onoue, S. *Int J Pharmaceut* 2011, *420*, 1.

(3) Dennis Douroumis, A. F. *Drug Delivery Strategies for Poorly Water-Soluble Drugs*; John Wiley & Sons Ltd: Chichester, 2013.

(4) van Hoogevest, P.; Liu, X. L.; Fahr, A. *Expert Opin Drug Del* 2011, *8*, 1481.

(5) Robert O. Williams III, A. B. W., Dave A. Miller.

(6) Torchilin, V. P. *Journal of Controlled Release* 2001, *73*, 137.

(7) Bang, J.; Jain, S.; Li, Z.; Lodge, T. P.; Pedersen, J. S.; Kesselman, E.; Talmon, Y. *Macromolecules* 2006, *39*, 5583.

(8) Jain, S.; Bates, F. S. *Science* 2003, *300*, 460.

(9) Yang, X. Q.; Grailer, J. J.; Pilla, S.; Steeber, D. A.; Gong, S. Q. *Bioconjugate Chem* 2010, *21*, 496.

(10) Cao, W. Q.; Zhou, J.; Mann, A.; Wang, Y.; Zhu, L. *Biomacromolecules* 2011, *12*, 2697.

(11) Rosler, A.; Vandermeulen, G. W. M.; Klok, H. A. *Adv Drug Deliver Rev* 2012, *64*, 270.

(12) Tyrrell, Z. L.; Shen, Y. Q.; Radosz, M. *Prog Polym Sci* 2010, *35*, 1128.

(13) Elsabahy, M.; Wooley, K. L. *Chem Soc Rev* 2012, *41*, 2545.

(14) Letchford, K.; Burt, H. *Eur J Pharm Biopharm* 2007, *65*, 259.

(15) Otsuka, H.; Nagasaki, Y.; Kataoka, K. *Curr Opin Colloid In* 2001, *6*, 3.

(16) Jokerst, J. V.; Lobovkina, T.; Zare, R. N.; Gambhir, S. S. *Nanomedicine-Uk*

2011, *6*, 715.

(17) Engler, A. C.; Chan, J. M. W.; Fukushima, K.; Coady, D. J.; Yang, Y. Y.; Hedrick, J. L. *Acs Macro Lett* 2013, *2*, 332.

(18) Owen, S. C.; Chan, D. P. Y.; Shoichet, M. S. *Nano Today* 2012, *7*, 53.

(19) Zhu, Z. X. *Biomaterials* 2013, *34*, 10238.

(20) Aguilar-Castillo, B. A.; Santos, J. L.; Luo, H. Y.; Aguirre-Chagala, Y. E.; Palacios-Hernandez, T.; Herrera-Alonso, M. *Soft Matter* 2015, *11*, 7296.

(21) Malmsten, M.; Lindman, B. *Macromolecules* 1992, *25*, 5440.

(22) Rowan, S. J. *Nat Mater* 2009, *8*, 89.

(23) Smart, T.; Lomas, H.; Massignani, M.; Flores-Merino, M. V.; Perez, L. R.; Battaglia, G. *Nano Today* 2008, *3*, 38.

(24) Dormidontova, E. E. *Macromolecules* 1999, *32*, 7630.

(25) Hayward, R. C.; Pochan, D. J. *Macromolecules* 2010, *43*, 3577.

(26) Won, Y. Y.; Davis, H. T.; Bates, F. S. *Macromolecules* 2003, *36*, 953.

(27) Lund, R.; Willner, L.; Richter, D.; Dormidontova, E. E. *Macromolecules* 2006, *39*, 4566.

(28) Liu, Y.; Cheng, C. Y.; Liu, Y.; Prud'homme, R. K.; Fox, R. O. *Chem Eng Sci* 2008, *63*, 2829.

(29) Johnson, B. K.; Prud'homme, R. K. *Phys Rev Lett* 2003, *91*.

(30) Karnik, R.; Gu, F.; Basto, P.; Cannizzaro, C.; Dean, L.; Kyei-Manu, W.; Langer, R.; Farokhzad, O. C. *Nano Lett* 2008, *8*, 2906.

(31) Cui, H. G.; Chen, Z. Y.; Zhong, S.; Wooley, K. L.; Pochan, D. J. *Science* 2007, *317*, 647.

(32) Wang, C. W.; Sinton, D.; Moffitt, M. G. *J Am Chem Soc* 2011, *133*, 18853.

(33) Allen, C.; Maysinger, D.; Eisenberg, A. *Colloid Surface B* 1999, *16*, 3.

(34) Gaucher, G.; Dufresne, M. H.; Sant, V. P.; Kang, N.; Maysinger, D.; Leroux, J. C. *Journal of Controlled Release* 2005, *109*, 169.

(35) Torchilin, V. P. *Pharm Res* 2007, *24*, 1.

(36) Kumar, V.; Prud'Homme, R. K. *J Pharm Sci-Us* 2008, *97*, 4904.

(37) D'Addio, S. M.; Prud'homme, R. K. *Adv Drug Deliver Rev* 2011, *63*, 417.

(38) Brick, M. C.; Palmer, H. J.; Whitesides, T. H. *Langmuir : the ACS journal of surfaces and colloids* 2003, *19*, 6367.

(39) Kumar, V.; Wang, L.; Riebe, M.; Tung, H. H.; Prud'homme, R. K. *Mol Pharm* 2009, *6*, 1118.

(40) Johnson, B. K.; Prud'homme, R. K. *Aust J Chem* 2003, *56*, 1021.

(41) Pustulka, K. M.; Wohl, A. R.; Lee, H. S.; Michel, A. R.; Han, J.; Hoye, T. R.; McCormick, A. V.; Panyam, J.; Macosko, C. W. *Molecular Pharmaceutics* 2013, *10*, 4367.

(42) Russ, B.; Liu, Y.; Prud'homme, R. K. *Chem Eng Commun* 2010, *197*, 1068.

(43) Sheiko, S. S.; Sumerlin, B. S.; Matyjaszewski, K. *Prog Polym Sci* 2008, *33*, 759.

(44) Torchilin, V. P. *Nanoparticulates as Drug Carrieres*; Imperial College Press: London, 2006.

(45) Ambade, A. V.; Savariar, E. N.; Thayumanavan, S. *Molecular Pharmaceutics* 2005, *2*, 264.

(46) Santos, J. L.; Herrera-Alonso, M. *Macromolecules* 2014, *47*, 137.

(47) Aryal, S.; Prabaharan, M.; Pilla, S.; Gong, S. Q. *Int J Biol Macromol* 2009, *44*, 346.

(48) Zhang, W. L.; Li, Y. L.; Liu, L. X.; Sun, Q. Q.; Shuai, X. T.; Zhu, W.; Chen, Y.

M. *Biomacromolecules* 2010, *11*, 1331.

(49) Essa, S.; Rabanel, J. M.; Hildgen, P. *Eur J Pharm Biopharm* 2010, *75*, 96.

(50) Sheiko, S. S.; Borisov, O. V.; Prokhorova, S. A.; Moller, M. *Eur Phys J E* 2004, *13*, 125.

(51) Guo, J. T.; Hong, H.; Chen, G. J.; Shi, S. X.; Nayak, T. R.; Theuer, C. P.; Barnhart, T. E.; Cai, W. B.; Gong, S. Q. *Acs Appl Mater Inter* 2014, *6*, 21769.

(52) Lian, X. M.; Wu, D. X.; Song, X. H.; Zhao, H. Y. *Macromolecules* 2010, *43*, 7434.

(53) Beers, K. L.; Gaynor, S. G.; Matyjaszewski, K.; Sheiko, S. S.; Moller, M. *Macromolecules* 1998, *31*, 9413.

(54) Nese, A.; Lebedeva, N. V.; Sherwood, G.; Averick, S.; Li, Y.; Gao, H.; Peteanu, L.; Sheiko, S. S.; Matyjaszewski, K. *Macromolecules* 2011, *44*, 5905.

(55) Johnson, J. A.; Lu, Y. Y.; Burts, A. O.; Lim, Y.-H.; Finn, M. G.; Koberstein, J. T.; Turro, N. J.; Tirrell, D. A.; Grubbs, R. H. *Journal of the American Chemical Society* 2011, *133*, 559.

(56) Li, X.; ShamsiJazeyi, H.; Pesek, S. L.; Agrawal, A.; Hammouda, B.; Verduzco, R. *Soft Matter* 2014, *10*, 2008.

(57) Fenyves, R.; Schmutz, M.; Horner, I. J.; Bright, F. V.; Rzayev, J. *J Am Chem Soc* 2014, *136*, 7762.

(58) Wang, C. E.; Stayton, P. S.; Pun, S. H.; Convertine, A. J. *J Control Release* 2015, *219*, 345.

(59) Zheng, Y. C.; Li, S. P.; Weng, Z. L.; Gao, C. *Chem Soc Rev* 2015, *44*, 4091.

(60) Kosovan, P.; Kuldova, J.; Limpouchova, Z.; Prochazka, K.; Zhulina, E. B.; Borisov, O. V. *Macromolecules* 2009, *42*, 6748.

(61) Feng, C.; Li, Y. J.; Yang, D.; Hu, J. H.; Zhang, X. H.; Huang, X. Y. *Chem Soc Rev* 2011, *40*, 1282.

(62) Peng, S. J.; Bhushan, B. *Rsc Adv* 2012, *2*, 8557.

(63) Lee, H. I.; Pietrasik, J.; Sheiko, S. S.; Matyjaszewski, K. *Prog Polym Sci* 2010, *35*, 24.

(64) Verduzco, R.; Li, X. Y.; Pesek, S. L.; Stein, G. E. *Chem Soc Rev* 2015, *44*, 7916.

(65) Rzayev, J. *Acs Macro Lett* 2012, *1*, 1146.

(66) Zou, J.; Yu, Y.; Li, Y.; Ji, W.; Chen, C.-K.; Law, W.-C.; Prasad, P. N.; Cheng, C. *Biomaterials Science* 2015, *3*, 1078.

(67) Fu, Q.; Ren, J. M.; Qiao, G. G. *Polymer Chemistry* 2012, *3*, 343.

(68) Kutnyanszky, E.; Hempenius, M. A.; Vancso, G. J. *Polymer Chemistry* 2014, *5*, 771.

(69) Guo, J.; Peng, L.; Yuan, J. *European Polymer Journal* 2015, *69*, 449.

(70) Lee, H.-i.; Pietrasik, J.; Sheiko, S. S.; Matyjaszewski, K. *Progress in Polymer Science* 2010, *35*, 24.

(71) Tezuka, Y.; Oike, H. *J Am Chem Soc* 2001, *123*, 11570.

(72) Qiu, L. Y.; Bae, Y. H. *Pharm Res* 2006, *23*, 1.

(73) Mullner, M.; Dodds, S. J.; Nguyen, T. H.; Senyschyn, D.; Porter, C. J. H.; Boyd, B. J.; Caruso, F. *ACS nano* 2015, *9*, 1294.

(74) Xu, P. S.; Tang, H. D.; Li, S. Y.; Ren, J.; Van Kirk, E.; Murdoch, W. J.; Radosz, M.; Shen, Y. Q. *Biomacromolecules* 2004, *5*, 1736.

(75) Ren, Y. Y.; Wei, Z. Y.; Leng, X. F.; Wu, T.; Bian, Y. F.; Li, Y. *The journal of Physical Chemistry B* 2016, *120*, 4078.

(76) Hadjichristidis, N.; Pispas, S.; Floudas, G. A. *Copolymers: Synthesis Strategies,*

Physical Properties, and Applications; John Wiley & Sons, Inc: Hoboken, 2003.

(77) Li, S. X.; Ye, C. N.; Zhao, G. D.; Zhang, M. J.; Zhao, Y. L. *J Polym Sci Pol Chem* 2012, *50*, 3135.

(78) Johnson, J. A.; Lu, Y. Y.; Burts, A. O.; Xia, Y.; Durrell, A. C.; Tirrell, D. A.; Grubbs, R. H. *Macromolecules* 2010, *43*, 10326.

(79) Rouault, Y.; Borisov, O. V. *Macromolecules* 1996, *29*, 2605.

(80) Borisov, O. V.; Zhulina, E. B. *Macromolecules* 2005, *38*, 2506.

(81) Polotsky, A.; Charlaganov, M.; Xu, Y. Y.; Leermakers, F. A. M.; Daoud, M.; Muller, A. H. E.; Dotera, T.; Borisov, O. *Macromolecules* 2008, *41*, 4020.

(82) Reynhout, I. C.; Cornelissen, J. J. L. M.; Nolte, R. J. M. *J Am Chem Soc* 2007, *129*, 2327.

(83) Zheng, Y.; Won, Y. Y.; Bates, F. S.; Davis, H. T.; Scriven, L. E.; Talmon, Y. *J Phys Chem B* 1999, *103*, 10331.

(84) He, Y. Y.; Li, Z. B.; Simone, P.; Lodge, T. P. *J Am Chem Soc* 2006, *128*, 2745.

(85) Li, Z.; Ma, J.; Lee, N. S.; Wooley, K. L. *J Am Chem Soc* 2011, *133*, 1228.

(86) Pochan, D. J.; Chen, Z. Y.; Cui, H. G.; Hales, K.; Qi, K.; Wooley, K. L. *Science* 2004, *306*, 94.

(87) Wang, C. Q.; Li, G. T.; Guo, R. R. *Chemical Communications* 2005, 3591.

(88) Cui, H. G.; Chen, Z. Y.; Wooley, K. L.; Pochan, D. J. *Macromolecules* 2006, *39*, 6599.

(89) Chen, Z. Y.; Cui, H. G.; Hales, K.; Li, Z. B.; Qi, K.; Pochan, D. J.; Wooley, K. L. *J Am Chem Soc* 2005, *127*, 8592.

(90) Yu, H. Z.; Jiang, W. *Macromolecules* 2009, *42*, 3399.

(91) Garnier, S.; Laschewsky, A. *Macromolecules* 2005, *38*, 7580.

(92) Zhu, J. H.; Zhang, S. Y.; Zhang, K.; Wang, X. J.; Mays, J. W.; Wooley, K. L.; Pochan, D. J. *Nat Commun* 2013, *4*.

(93) Gao, H.; Matyjaszewski, K. *J Am Chem Soc* 2007, *129*, 11828.

(94) Xia, Y.; Kornfield, J. A.; Grubbs, R. H. *Macromolecules* 2009, *42*, 3761.

(95) Yuan, Y. Y.; Du, Q.; Wang, Y. C.; Wang, J. *Macromolecules* 2010, *43*, 1739.

(96) Chang, H. Y.; Lin, Y. L.; Sheng, Y. J. *Macromolecules* 2012, *45*, 4778.

(97) Huang, K.; Rzayev, J. *J Am Chem Soc* 2011, *133*, 16726.

(98) Zhao, P.; Yan, Y. C.; Feng, X. Q.; Liu, L. X.; Wang, C.; Chen, Y. M. *Polymer* 2012, *53*, 1992.

(99) Spaeth, J. R.; Kevrekidis, I. G.; Panagiotopoulos, A. Z. *J Chem Phys* 2011, *135*.

(100) Chen, L.; Jiang, T.; Lin, J. P.; Cai, C. H. *Langmuir : the ACS journal of surfaces and colloids* 2013, *29*, 8417.

(101) Wang, C. W.; Sinton, D.; Moffitt, M. G. *ACS nano* 2013, *7*, 1424.

(102) Torchilin, V. P. *Nanoparticles as Drug Carriers* 2006.

(103) Feng, C.; Lu, G. L.; Li, Y. J.; Huang, X. Y. *Langmuir : the ACS journal of surfaces and colloids* 2013, *29*, 10922.

(104) Shen, H.; Hong, S. Y.; Prud'homme, R. K.; Liu, Y. *J Nanopart Res* 2011, *13*, 4109.

(105) Luo, H.; Santos, J. L.; Herrera-Alonso, M. *Chemical Communications* 2014, *50*, 536.

(106) Feuz, L.; Strunz, P.; Geue, T.; Textor, M.; Borisov, O. *Eur Phys J E* 2007, *23*, 237.

(107) Johnson, B. K.; Prud'homme, R. K. *Aiche J* 2003, *49*, 2264.

(108) Hopkins, S. C.; Vale, R. D.; Kuntz, I. D. *Biochemistry-Us* 2000, *39*, 2805.

(109) Lu, L. D.; Rininsland, F. H.; Wittenburg, S. K.; Achyuthan, K. E.; McBranch, D. W.; Whitten, D. G. *Langmuir : the ACS journal of surfaces and colloids* 2005, *21*, 10154.

(110) Hanying Luo, D. R., Chao Wang, and Margarita Herrera-Alonso *Molecular Pharmaceutics*, *13*, 1855.

(111) Matteucci, M. E.; Brettmann, B. K.; Rogers, T. L.; Elder, E. J.; Williams, R. O.; Johnston, K. P. *Molecular Pharmaceutics* 2007, *4*, 782.

(112) Chen, J. F.; Zhang, J. Y.; Shen, Z. G.; Zhong, J.; Yun, J. *Ind Eng Chem Res* 2006, *45*, 8723.

(113) Lindfors, L.; Skantze, P.; Skantze, U.; Westergren, J.; Olsson, U. *Langmuir : the ACS journal of surfaces and colloids* 2007, *23*, 9866.

(114) Shah, P. *Mrs Bull* 2006, *31*, 894.

(115) Horn, D.; Rieger, J. *Angew Chem Int Edit* 2001, *40*, 4331.

(116) Texter, J. *J Disper Sci Technol* 2001, *22*, 499.

(117) Shekunov, B. Y.; Baldyga, J.; York, P. *Chem Eng Sci* 2001, *56*, 2421.

(118) Van Keuren, E. R. *J Disper Sci Technol* 2004, *25*, 547.

(119) Xiong, J. Y.; Liu, X. Y.; Chen, S. B.; Chung, T. S. *J Phys Chem B* 2005, *109*, 13877.

(120) Cheng, J.; Teply, B. A.; Sherifi, I.; Sung, J.; Luther, G.; Gu, F. X.; Levy-Nissenbaum, E.; Radovic-Moreno, A. F.; Langer, R.; Farokhzad, O. C. *Biomaterials* 2007, *28*, 869.

(121) Farokhzad, O. C.; Cheng, J. J.; Teply, B. A.; Sherifi, I.; Jon, S.; Kantoff, P. W.; Richie, J. P.; Langer, R. *P Natl Acad Sci USA* 2006, *103*, 6315.

(122) Harris, L. A.; Goff, J. D.; Carmichael, A. Y.; Riffle, J. S.; Harburn, J. J.; St

Pierre, T. G.; Saunders, M. *Chem Mater* 2003, *15*, 1367.

(123) Kakizawa, Y.; Kataoka, K. *Langmuir : the ACS journal of surfaces and colloids* 2002, *18*, 4539.

(124) Berret, J. F.; Yokota, K.; Morvan, M.; Schweins, R. *J Phys Chem B* 2006, *110*, 19140.

(125) Schwarzer, H. C.; Peukert, W. *Aiche J* 2004, *50*, 3234.

(126) Zhao, H.; Wang, J. X.; Wang, Q. A.; Chen, J. F.; Yun, J. *Ind Eng Chem Res* 2007, *46*, 8229.

(127) Kumari, A.; Yadav, S. K.; Yadav, S. C. *Colloid Surface B* 2010, *75*, 1.

(128) Soppimath, K. S.; Aminabhavi, T. M.; Kulkarni, A. R.; Rudzinski, W. E. *J Control Release* 2001, *70*, 1.

(129) Nicolas, J.; Mura, S.; Brambilla, D.; Mackiewicz, N.; Couvreur, P. *Chem Soc Rev* 2013, *42*, 1147.

(130) Zhu, Z. X. *Molecular Pharmaceutics* 2014, *11*, 776.

(131) Kumar, V.; Wang, L.; Riebe, M.; Tung, H. H.; Prud'homme, R. K. *Molecular Pharmaceutics* 2009, *6*, 1118.

(132) Gu, L. N.; Shen, Z.; Zhang, S.; Lu, G. L.; Zhang, X. H.; Huang, X. Y. *Macromolecules* 2007, *40*, 4486.

(133) Li, C. H.; Ge, Z. S.; Fang, J.; Liu, S. Y. *Macromolecules* 2009, *42*, 2916.

(134) Zhao, C. Z.; Wu, D. X.; Lian, X. M.; Zhang, Y.; Song, X. H.; Zhao, H. Y. *J Phys Chem B* 2010, *114*, 6300.

(135) Zhu, Z. X.; Margulis-Goshen, K.; Magdassi, S.; Talmon, Y.; Macosko, C. W. *J Pharm Sci-Us* 2010, *99*, 4295.

(136) Luo, H. Y.; Santos, J. L.; Herrera-Alonso, M. *Chemical Communications* 2014,

50, 536.

(137) Li, Y.; Qi, X. R.; Maitani, Y.; Nagai, T. *Nanotechnology* 2009, *20*.

(138) Anantachoke, N.; Makha, M.; Raston, C. L.; Reutrakul, V.; Smith, N. C.; Saunders, M. *J Am Chem Soc* 2006, *128*, 13847.

(139) Helgason, T.; Awad, T. S.; Kristbergsson, K.; Decker, E. A.; McClements, D. J.; Weiss, J. *J Agr Food Chem* 2009, *57*, 8033.

(140) Liu, Y.; Kathan, K.; Saad, W.; Prud'homme, R. K. *Phys Rev Lett* 2007, *98*.

(141) Li, Y.; Yue, T. T.; Yang, K.; Zhang, X. R. *Biomaterials* 2012, *33*, 4965.

(142) Nangia, S.; Sureshkumar, R. *Langmuir : the ACS journal of surfaces and colloids* 2012, *28*, 17666.

(143) Truong, N. P.; Whittaker, M. R.; Mak, C. W.; Davis, T. P. *Expert Opin Drug Del* 2015, *12*, 129.

(144) Herd, H.; Daum, N.; Jones, A. T.; Huwer, H.; Ghandehari, H.; Lehr, C. M. *ACS nano* 2013, *7*, 1961.

(145) Albanese, A.; Tang, P. S.; Chan, W. C. W. *Annu Rev Biomed Eng* 2012, *14*, 1.

(146) Schulz, A.; Jaksch, S.; Schubel, R.; Wegener, E.; Di, Z. Y.; Han, Y. C.; Meister, A.; Kressler, J.; Kabanov, A. V.; Luxenhofer, R.; Papadakis, C. M.; Jordan, R. *ACS nano* 2014, *8*, 2686.

(147) Khimani, M.; Ganguly, R.; Aswal, V. K.; Nath, S.; Bahadur, P. *J Phys Chem B* 2012, *116*, 14943.

(148) Zhou, Z. Y.; D'Emanuele, A.; Attwood, D. *Int J Pharmaceut* 2013, *452*, 173.

(149) Sharma, P. K.; Reilly, M. J.; Jones, D. N.; Robinson, P. M.; Bhatia, S. R. *Colloid Surface B* 2008, *61*, 53.

(150) Mikhail, A. S.; Allen, C. *Biomacromolecules* 2010, *11*, 1273.

(151) Tan, H.; Wang, Z. G.; Li, J. H.; Pan, Z. C.; Ding, M. M.; Fu, Q. *Acs Macro Lett* 2013, *2*, 146.

(152) Woodhead, J. L.; Hall, C. K. *Langmuir : the ACS journal of surfaces and colloids* 2010, *26*, 15135.

(153) Gindy, M. E.; Panagiotopoulos, A. Z.; Prud'homme, R. K. *Langmuir : the ACS journal of surfaces and colloids* 2008, *24*, 83.

(154) Tam, J. M.; Murthy, A. K.; Ingram, D. R.; Nguyen, R.; Sokolov, K. V.; Johnston, K. P. *Langmuir : the ACS journal of surfaces and colloids* 2010, *26*, 8988.

(155) Polotsky, A. A.; Gillich, T.; Borisov, O. V.; Leermakers, F. A. M.; Textor, M.; Birshtein, T. M. *Macromolecules* 2010, *43*, 9555.

(156) Napper, D. H. *Academic Press: New York, 1983* 1983, *p*, xvi.

(157) Visaveliya, N.; Kohler, J. M. *Acs Appl Mater Inter* 2014, *6*, 11254.

(158) Deppe, D. D.; Dhinojwala, A.; Torkelson, J. M. *Macromolecules* 1996, *29*, 3898.

(159) Veniaminov, A. V.; Sillescu, H. *Macromolecules* 1999, *32*, 1828.

(160) Ehlich, D.; Sillescu, H. *Macromolecules* 1990, *23*, 1600.

(161) Jamshidi, K.; Hyon, S. H.; Ikada, Y. *Polymer* 1988, *29*, 2229.

(162) Choo, Y.; Mahajan, L. H.; Gopinadhan, M.; Ndaya, D.; Deshmukh, P.; Kasi, R. M.; Osuji, C. O. *Macromolecules* 2015, *48*, 8315.

(163) Bechtold, K.; Hillmyer, M. A.; Tolman, W. B. *Macromolecules* 2001, *34*, 8641.

(164) Kikkawa, Y.; Fujita, M.; Abe, H.; Doi, Y. *Biomacromolecules* 2004, *5*, 1187.

(165) Vyavahare, O.; Ng, D.; Hsu, S. L. *J Phys Chem B* 2014, *118*, 4185.

(166) Ricarte, R. G.; Lodge, T. P.; Hillmyer, M. A. *Molecular Pharmaceutics* 2015, *12*, 983.

(167) Raffa, P.; Wever, D. A. Z.; Picchioni, F.; Broekhuis, A. A. *Chem Rev* 2015, *115*, 8504.

(168) Laukkanen, A.; Valtola, L.; Winnik, F. M.; Tenhu, H. *Polymer* 2005, *46*, 7055.

(169) Morishima, Y.; Nomura, S.; Ikeda, T.; Seki, M.; Kamachi, M. *Macromolecules* 1995, *28*, 2874.

(170) Yamamoto, H.; Mizusaki, M.; Yoda, K.; Morishima, Y. *Macromolecules* 1998, *31*, 3588.

(171) Mizusaki, M.; Morishima, Y.; Winnik, F. M. *Macromolecules* 1999, *32*, 4317.

(172) Song, C. F.; Li, L. Y.; Dai, L. Z.; Thayumanavan, S. *Polym Chem-Uk* 2015, *6*, 4828.

(173) Lyon, C. K.; Prasher, A.; Hanlon, A. M.; Tuten, B. T.; Tooley, C. A.; Frank, P. G.; Berda, E. B. *Polym Chem-Uk* 2015, *6*, 181.

(174) Zhou, Y. M.; Jiang, K. Q.; Song, Q. L.; Liu, S. Y. *Langmuir : the ACS journal of surfaces and colloids* 2007, *23*, 13076.

(175) Weller, D.; McDaniel, J. R.; Fischer, K.; Chilkoti, A.; Schmidt, M. *Macromolecules* 2013, *46*, 4966.

(176) Rathgeber, S.; Pakula, T.; Wilk, A.; Matyjaszewski, K.; Beers, K. L. *J Chem Phys* 2005, *122*.

(177) Zhao, P.; Liu, L. X.; Feng, X. Q.; Wang, C.; Shuai, X. T.; Chen, Y. M. *Macromolecular Rapid Communications* 2012, *33*, 1351.

(178) Kline, S. R. *Journal of applied crystallography* 2006, *39*, 895.

(179) Ruff, Y.; Buhler, E.; Candau, S. J.; Kesselman, E.; Talmon, Y.; Lehn, J. M. *J Am Chem Soc* 2010, *132*, 2573.

(180) Hammouda, B. *Journal of Applied Crystallography* 2010, *43*, 716.

(181) Pesek, S. L.; Li, X. Y.; Hammouda, B.; Hong, K. L.; Verduzco, R. *Macromolecules* 2013, *46*, 6998.

(182) Gromadzki, D.; Jigounov, A.; Stepanek, P.; Makuska, R. *Eur Polym J* 2010, *46*, 804.

(183) Kuntsche, J.; Horst, J. C.; Bunjes, H. *Int J Pharmaceut* 2011, *417*, 120.

(184) Riley, T.; Stolnik, S.; Heald, C. R.; Xiong, C. D.; Garnett, M. C.; Illum, L.; Davis, S. S.; Purkiss, S. C.; Barlow, R. J.; Gellert, P. R. *Langmuir : the ACS journal of surfaces and colloids* 2001, *17*, 3168.

(185) Glatter, O. *J Appl Crystallogr* 1979, *12*, 166.

(186) Ting, J. M.; Navale, T. S.; Bates, F. S.; Reineke, T. M. *Macromolecules* 2014, *47*, 6554.

(187) Dalsin, M. C.; Tale, S.; Reineke, T. M. *Biomacromolecules* 2014, *15*, 500.

(188) Stancik, C. M.; Lavoie, A. R.; Schutz, J.; Achurra, P. A.; Lindner, P.; Gast, A. P.; Waymouth, R. M. *Langmuir : the ACS journal of surfaces and colloids* 2004, *20*, 596.

(189) Rosler, A.; Vandermeulen, G. W. M.; Klok, H. A. *Advanced Drug Delivery Reviews* 2001, *53*, 95.

(190) Jones, M. C.; Leroux, J. C. *European Journal of Pharmaceutics and Biopharmaceutics* 1999, *48*, 101.

(191) D'Addio, S. M.; Saad, W.; Ansell, S. M.; Squiers, J. J.; Adamson, D. H.; Herrera-Alonso, M.; Wohl, A. R.; Hoye, T. R.; Macosko, C. W.; Mayer, L. D.; Vauthier, C.; Prud'homme, R. K. *J Control Release* 2012, *162*, 208.

(192) Swami, A.; Shi, J. J.; Gadde, S.; Votruba, A. R.; Kolishetti, N.; Farokhzad, O. C. *Nanostruct Sci Techn* 2012, 9.

(193) Huang, Y.; Li, L.; Fang, Y. e. *Materials Letters* 2009, *63*, 1416.

(194) Khelfallah, N.; Gunari, N.; Fischer, K.; Gkogkas, G.; Hadjichristidis, N.; Schmidt, M. *Macromolecular Rapid Communications* 2005, *26*, 1693.

(195) Du, J. Z.; Tang, L. Y.; Song, W. J.; Shi, Y.; Wang, J. *Biomacromolecules* 2009, *10*, 2169.

(196) Cheng, C.; Qi, K.; Germack, D. S.; Khoshdel, E.; Wooley, K. L. *Adv Mater* 2007, *19*, 2830.

(197) Guo, J.; Hong, H.; Chen, G.; Shi, S.; Nayak, T. R.; Theuer, C. P.; Barnhart, T. E.; Cai, W.; Gong, S. *ACS Appl. Mater. Interfaces* 2014, *6*, 21769.

(198) Yu, Y.; Chen, C.-K.; Law, W.-C.; Sun, H.; Prasad, P. N.; Cheng, C. *Polymer Chemistry* 2015, *6*, 953.

(199) Trivedi, R.; Kompella, U. B. *Nanomedicine-Uk* 2010, *5*, 485.

(200) Bertin, P. A.; Watson, K. J.; Nguyen, S. T. *Macromolecules* 2004, *37*, 8364.

(201) Li, L. Y.; Raghupathi, K.; Song, C. F.; Prasad, P.; Thayumanavan, S. *Chemical Communications* 2014, *50*, 13417.

(202) Zhang, L. F.; Eisenberg, A. *Macromolecules* 1999, *32*, 2239.

(203) Takaya Terashima, T. S., Kaoru Fukae, Mitsuo Sawamoto *Macromolecules* 2014, *47*, 589.

(204) Varun Kumar, L. W., Mike Riebe, Hsien-Hsin Tung, Robert K. Prud'homme *Molecular Pharmaceutics* 2009, *6*, 1118.

(205) Hao Shen, S. H., Robert K. Prud'homme, Ying Liu *J Nanopart Res* 2011, *13*, 4109.

(206) Hucknall, A.; Kim, D. H.; Rangarajan, S.; Hill, R. T.; Reichert, W. M.; Chilkoti, A. *Adv Mater* 2009, *21*, 1968.

CURRICULUM VITA

Hanying Luo was born on June 11, 1986 in Chengdu, Sichuan Province, China. She received her Bachelor of Science in Biomedical Engineering at Southeast University in 2009, and Master of Science in Materials Science and Engineering at University of Florida in 2011. She joined the Materials Science and Engineering Department at Johns Hopkins University in 2011, started to work in Professor Margarita Herrera-Alonso's group. Her research focuses on self-assembly behavior of amphiphilic macromolecular brush copolymers and their application as hydrophobic solute stabilizers. Important publication to date include:

Refereed Journal Articles:

H. Luo, D. Raciti, C. Wang, M. Herrera-Alonso, "Macromolecular Brushes as Stabilizers of Hydrophobic Solute Nanoparticles," *Molecular Pharmaceutics*, **2016**, 13 (6).

B. A. Aguilar-Castillo, J. L. Santos, **H. Luo**, M. Herrera-Alonso et al., "Nanoparticle stability in biologically relevant media: influence of polymer architecture," *Soft Matter*, **2015**, 11, 7296.

H. Luo, J. L. Santos and M. Herrera-Alonso, "Toroidal structures from brush amphiphiles," *Chem. Commun.*, **2014**, 50, 53.